UNIVERSITY OF CALIFORNIA

Santa Barbara

Molecular Beam Epitaxy of β-Ga$_2$O$_3$: Growth and Doping

A dissertation submitted in partial satisfaction of the

requirements for the degree Doctor of Philosophy

in Materials

by

Takeki Itoh

Committee in charge:

Professor James S. Speck, Chair

Professor Chris Palmstrom

Professor Steven DenBaars

Professor Umesh Mishra

September 2023

The dissertation of Takeki Itoh is approved.

_____

Chris Palmstrom

_____

Umesh Mishra

_____

Steven P. DenBaars

_____

James S. Speck, Committee Chair

September 2023

Molecular Beam Epitaxy of β-Ga$_2$O$_3$: Growth and Doping

Krishnamoorthy group: Arkka Bhattacharyya, Saurav Roy, Carl Peterson, Yizheng Liu and Kittamet Chanchaiworawit.

Finally, I would like to express my deepest appreciation to my family and friends for their support during the PhD program. My parents, Yukihisa Itoh and Hitomi Itoh in Japan, have always been supportive for my journey as a PhD student in the US. This endeavor would not have been possible without my wife, Yuka Itoh, and my two sons, Gaku Itoh and Kento Itoh.

CURRICULUM VITAE
TAKEKI ITOH
July 2023

<u>EDUCATION</u>

Doctor of Philosophy in Materials, University of California, Santa Barbara   July 2023
(expected)
Advisor: Prof. James S. Speck

Master of Engineering in Applied Chemistry, The University of Tokyo,   March 2015
Advisor: Prof. Hiroshi Fujioka

Bachelor of Engineering in Applied Chemistry, The University of Tokyo,   March 2013
Advisor: Prof. Masaharu Oshima

<u>EXPERIENCE</u>

Graduate Student Researcher, Speck Group, UCSB   2018-Present
- Epitaxial growth of gallium oxide films by molecular beam epitaxy.
- Structural characterization and analysis of the crystal quality of thin films.
- Device fabrication process of gallium oxide-based power electronics.

Graduate Teaching assistant, Speck Group, UCSB   2022
- Undergraduate introduction to Materials Science and Engineering

Display Research Engineer, Sony, Microdisplay Development Department   2015-2018
- Development of high light-resistance liquid crystal materials for LCDs.
- Design of mass-production equipment for high-efficiency hydrolysis process.
- Device simulation of LCD panels for high brightness design rules.

Graduate Research Assistant, Fujioka Group, The University of Tokyo, 2013-2015
- Demonstration of the first InGaN-based thin film transistors on glass substrates.
- Crystal growth of nitride semiconductor materials by pulsed sputtering.

<u>AWARDS</u>
SPIE 2022 Optics and Photonics Education Scholarship   2022
Bright Horizon Global Foundation Materials Department Service Awards   2022
Japan Student Service Organization (JASSO) Overseas Scholarship   2018

<u>SKILLS</u>
Epitaxial Growth: MBE, MOCVD, Sputtering, PECVD, ALD, Electron-beam evaporation
Characterization: Spectrometer, Raman, Polarimetry, Ellipsometer, XRD, XPS, RHEED, AFM, SEM, FIB, Hall, IV/CV
Processing: Lithography (stepper and maskless aligner), Spin-coat, Dry-etch (reactive ion etching, plasma etching), Wet-etching, Lift-off, Thermal annealing, Plasma ashing, Dicing saw, Soldering, LCD packaging,
Programing: MATLAB, Python, LabVIEW, CAD, VBA, LCD simulator, L-Edit, Klayout.

PUBLICATIONS

22. **Takeki Itoh**, Akhil Mauze, Yuewei Zhang and James S. Speck, *Continuous Si doping β-Ga$_2$O$_3$ films by plasma-assisted molecular beam epitaxy*, APL Mater. **11**, 041108 (2023).

21. **Takeki Itoh**, Akhil Mauze, Yuewei Zhang and James S. Speck, *Epitaxial growth of β-Ga$_2$O$_3$ on (110) substrate by plasma-assisted molecular beam epitaxy*, Appl. Phys. Lett. **117**, 152105 (2020).

20. **Takeki Itoh**, Atsushi Kobayashi, Jitsuo Ohta and Hiroshi Fujioka, *High-current-density indium nitride ultrathin-film transistors on glass substrates*, Appl. Phys. Lett. **109**, 142104 (2016).

19. **Takeki Itoh**, Atsushi Kobayashi, Kohei Ueno, Jitsuo Ohta and Hiroshi Fujioka, *Fabrication of InGaN thin-film transistors using pulsed sputtering deposition*, Sci. Rep. **6**, 29500 (2016).

18. Fikadu Alema*, **Takeki Itoh***, William Brand, Marko Tadjer, Andrei Osinsky and James S. Speck, *N$_2$O grown high Al composition nitrogen doped β-(AlGa)$_2$O$_3$/β-Ga$_2$O$_3$ using MOCVD*, J. Vac. Sci. Technol. A. **41**, 042709 (2023). (*: Equal contribution)

17. Fikadu Alema, **Takeki Itoh**, William Brand, Andrei Osinsky and James S. Speck, *Controllable nitrogen doping of MOCVD Ga$_2$O$_3$ using NH$_3$*, Appl. Phys. Lett. **122**, 252105 (2023).

16. Akhil Mauze, **Takeki Itoh**, Yuewei Zhang and James S. Speck, *Coherently strained (001) β-(Al$_x$Ga$_{1-x}$)$_2$O$_3$ thin films on β-Ga$_2$O$_3$: Growth and compositional analysis*, J. Appl. Phys. 132, 115302 (2022).

15. Fikadu Alema, **Takeki Itoh**, James S. Speck and Andrei Osinsky, *Highly conductive epitaxial β-Ga$_2$O$_3$ and β-(Al$_x$Ga$_{1-x}$)$_2$O$_3$ films by MOCVD*, Jpn. J. Appl. Phys. **61**, 100903 (2022).

14. Atsushi Kobayashi, **Takeki Itoh**, Jitsuo Ohta, Masaharu Oshima and Hiroshi Fujioka, *Solid-phase epitaxy of InO$_x$N$_y$ alloys via thermal oxidation of InN films on yttria-stabilized zirconia*, Phys. Status. Solidi RRL **8**, 362-336 (2014).

13. Arkka Bhattacharyya, Carl Peterson, **Takeki Itoh**, Saurav Roy, Jacqueline Cooke, Steve Rebollo, Praneeth Ranga, Berardi-Sensale-Rodriguez and Sriram Krishnamoorthy, *Enhancing the electron mobility in Si-doped (010) β-Ga$_2$O$_3$ films with low-temperature buffer layers*, APL Mater. **11**, 021110 (2023). [Featured]

12. Akhil Mauze, Yuewei Zhang, **Takeki Itoh** and James S. Speck, *Mg doping and diffusion in (010) β-Ga$_2$O$_3$ films grown by plasma-assisted molecular beam epitaxy*, J. Appl. Phys. **130**, 235301 (2021).

11. Akhil Mauze, Yuewei Zhang, **Takeki Itoh**, Elaheh Ahmadi and James S. Speck, *Sn doping of (010) β-Ga₂O₃ films grown by plasma-assisted molecular beam epitaxy*, Appl. Phys. Lett. **117**, 222102 (2020).

10. Akhil Mauze, Yuewei Zhang, **Takeki Itoh**, Feng Wu and James S. Speck, *Metal oxide catalyzed epitaxy (MOCATAXY) of β-Ga₂O₃ films in various orientations grown by plasma-assisted molecular beam epitaxy*, APL Mater. **8**, 021104 (2020). [Featured]

9. Esmat Farzana, Arkka Bhattacharyya, Nolan S Hendricks, **Takeki Itoh**, Sriram Krishnamoorthy and James S. Speck, *Oxidized metal Schottky contact with high-κ dielectric field plate for low-loss high-power vertical β-Ga₂O₃ Schottky diodes*, APL Mater. **10**, 111104 (2022). [Editor's pick]

8. Kenny Huynh, Michael E Liao, Akhil Mauze, **Takeki Itoh**, Xingxu Yan, James S. Speck, Xiaoqing Pan and Mark S Goorsky, *Surface reaction dependence of molecular beam epitaxy grown aluminum on various orientations of β-Ga₂O₃*, APL Mater. **10**, 011110 (2022).

7. Esmat Farzana, Jianfeng Wang, Morteza Monavarian, **Takeki Itoh**, Kai Shek Qwah, Zachary J. Biegler, Kelsey F. Jorgensen and James S. Speck, *Over 1 kV Vertical GaN-on-GaN pn Diodes with Low On-Resistance using Ammonia Molecular Beam Epitaxy*, IEEE Electron Device Lett. **41**, 1806 (2020). [Editor's pick]

6. Fikadu Alema, Yuewei Zhang, Akhil Mauze, **Takeki Itoh**, James S. Speck, Brian Hertog and Andrei Osinsky, *H₂O vapor assisted growth of β-Ga₂O₃ by MOCVD*, AIP Advances **10**, 085002 (2020).

5. Esmat Farzana, Fikadu Alema, Wan Ying Ho, Akhil Mauze, **Takeki Itoh**, Andrei Osinsky and James S. Speck, *Vertical β-Ga₂O₃ field plate Schottky barrier diode from metal-organic chemical vapor deposition*, Appl. Phys. Lett. **118**, 162109 (2021).

4. Robert Montgomery, Yuewei Zhang, Chao Yuan, Samuel Kim, Jingjing Shi, **Takeki Itoh**, Akhil Mauze, Satish Kumar, James Speck and Samuel Graham, *Thermal management strategies for gallium oxide vertical trench-fin MOSFET*, J. Appl. Phys. **129**, 085301 (2021).

3. Yuewei Zhang, Akhil Mauze, Fikadu Alema, Andrei Osinsky, **Takeki Itoh** and James S. Speck, *β-Ga₂O₃ lateral transistors with high aspect ratio fin-shape channels*, Jpn. J. Appl. Phys. **60,** 014001 (2021).

2. Chao Yuan, Yuewei Zhang, Robert Montgomery, Samuel Kim, Jingjing Shi, Akhil Mauze, **Takeki Itoh**, James S. Speck and Samuel Graham*, Modeling and analysis for thermal management in gallium oxide field-effect transistors*, J. Appl. Phys. **127**, 154502 (2020).

1. Fikadu Alema, Yuewei Zhang, Andrei Osinsky, Nicholas Valente, Akhil Mauze, **Takeki Itoh** and James S. Speck, *Low temperature electron mobility exceeding 10⁴ cm²/V s in MOCVD grown β-Ga₂O₃*, APL Mater. **7**, 121110 (2019). [Featured]

CONFERENCE PRESENTATIONS

31. **Takeki Itoh**, Fikadu Alema, Will Brand, James S. Speck and Andrei Osinsky, *MOCVD growth of β-(AlGa)$_2$O$_3$ on β-Ga$_2$O$_3$ using N$_2$O,* SPIE photonic west 12422 - 78 February-2023. [Invited]

30. **Takeki Itoh**, Akhil Mauze, Yuewei Zhang and James S. Speck, *Continuous Si doping in (010) and (001) β-Ga$_2$O$_3$ films by plasma-assisted molecular beam epitaxy,* The 4th International Workshop on Gallium Oxide and Related Materials, Epi 1-4, Nagano, Japan, October-2022.

29. **Takeki Itoh**, Akhil Mauze, Yuewei Zhang and James S. Speck, *β-Ga$_2$O$_3$ epitaxial growth on (110) substrate by plasma-assisted molecular beam epitaxy,* The 4th International Workshop on Gallium Oxide and Related Materials, Epi 3-1, Nagano, Japan, October-2022.

28. **Takeki Itoh**, Akhil Mauze, Yuewei Zhang and James S. Speck, *(110) β-Ga2O3 Epitaxial Films Grown by Plasma-Assisted Molecular Beam Epitaxy*, 5th Gallium Oxide Workshop, EG-TuA01, Washington, D.C., August-2022.

27. **Takeki Itoh**, Akhil Mauze, Yuewei Zhang and James S. Speck, *Epitaxial Growth on β-Ga$_2$O$_3$ (110) Substrate by Plasma-Assisted Molecular Beam Epitaxy*, 64th Electronic Materials Conference, L01, The Ohio State University, July-2022.

26. **Takeki Itoh**, Akhil Mauze, Yuewei Zhang and James S. Speck, *Crystal growth on (110) β-Ga$_2$O$_3$ via plasma-assisted molecular beam* epitaxy, SPIE photonic west opto, 116870U, March-2021.

25. **Takeki Itoh**, Atsushi Kobayashi, Kohei Ueno, Jitsuo Ohta and Hiroshi Fujioka, *InGaN thin-film transistors on amorphous glass substrates,* The 6th International Symposium on Growth of III-Nitrides, We-B62, Hamamatsu, November-2015.

24. **Takeki Itoh**, Atsushi Kobayashi, Kohei Ueno, Jitsuo Ohta and Hiroshi Fujioka, *Characteristics of thin-film transistors based on nitride semiconductors grown on glass substrates*, 76th JSAP Fall Meeting,15a-1D-7, Nagoya Congress Center, September-2015.

23. **Takeki Itoh**, Atsushi Kobayashi, Jitsuo Ohta, Masaharu Oshima and Hiroshi Fujioka, *High mobility c-axis-oriented ultrathin InN films grown on amorphous substrates*, 10th International Conference on Nitride Semiconductors, Washington, D.C., August- 2013.

22. **Takeki Itoh**, Atsushi Kobayashi, Jitsuo Ohta, Masaharu Oshima and Hiroshi Fujioka, *Characterization of InN films grown on fused silica,* 5th Nitride Semiconductor Crystal Growth Meeting, FR22, Osaka University, June-2013.

21. **Takeki Itoh**, Atsushi Kobayashi, Jitsuo Ohta, Hiroshi Fujioka and Masaharu Oshima, *Characterization of InN films grown on amorphous substrates*, 60th JSAP Spring Meeting, 28p-G21-2, Kanagawa Institute of Technology, March-2013.

20. Steve Rebollo, **Takeki Itoh**, Sriram Krishnamoorthy and James S. Speck, *An Investigation of (001) β-Ga$_2$O$_3$ Etching via Heated H$_3$PO$_4$,* 6th Gallium Oxide Workshop, MD-TuP-10, Buffalo, August-2023.

19. Fikadu Alema, **Takeki Itoh**, William Brand, Andrei Osinsky and James S. Speck, *Controllable Deep Acceptor Doping in MOCVD β-Ga$_2$O$_3$ to Compensate Parasitic Interface Charges*, EG-MoM-14, , 6th Gallium Oxide Workshop, MD-TuP-10, Buffalo, August-2023.

18. Akhil Mauze, **Takeki Itoh**, Yuewei Zhang and James S. Speck, *Coherently strained (001) β-Ga$_2$O$_3$-(Al$_x$Ga$_{1-x}$)$_2$O$_3$ thin films on β-Ga$_2$O$_3$*, The 4th International Workshop on Gallium Oxide and Related Materials, Epi 3-4, Nagano, Japan, October-2022.

17. Akhil Mauze, **Takeki Itoh**, Yuewei Zhang and James S. Speck, *Doping and diffusion of Mg in (010) β-Ga$_2$O$_3$ films grown by plasma-assisted molecular beam epitaxy*, The 4th International Workshop on Gallium Oxide and Related Materials, Epi 3-4, Nagano, Japan, October-2022.

16. Fikadu Alema, **Takeki Itoh**, James S. Speck and Andrei Osinsky, *Highly Conductive β-Ga$_2$O$_3$ and (Al$_x$Ga$_{1-x}$)$_2$O$_3$ epitaxial films by MOCVD,* 5th Gallium Oxide Workshop, EG-TuP09, Washington, D.C., August-2022.

15. Akhil Mauze, **Takeki Itoh**, Esmat Farzana, Yuewei Zhang and James S. Speck, *Materials development for high voltage vertical gallium oxide devices*, SPIE photonic west 12422-19 February-2023. [Invited]

14. Esmat Farzana, Arkka Bhattacharyya, Nolan Hendricks, **Takeki Itoh**, Sriram Krishnamoorthy and James S. Speck, Metal Oxide (PtO$_x$) Schottky Contact with High-k Dielectric Field Plate for Improved Field management in Vertical β-Ga$_2$O$_3$ Devices, DI-TuA13, Washington, D.C., August-2022.

13. Akhil Mauze, **Takeki Itoh**, Esmat Farzana, Yuewei Zhang and James S. Speck, *β-Ga$_2$O$_3$: Growth, Doping, and Device Design*, IWUMD 04_1009, May 2022. [Invited]

12. Esmat Farzana, Fikadu Alema, **Takeki Itoh**, Nolan Hendricks, Akhil Mauze, Andrei Osinsky and James S. Speck, *β-Ga$_2$O$_3$ epitaxy and power devices from metal-organic chemical vapor deposition*, SPIE photonic west opto, PC120020H, March-2022.

11. Esmat Farzana, Jianfeng Wang, Kelsey Jorgensen, Kai Shek Qwah, Morteza Monavarian, **Takeki Itoh**, Zachary J Biegler, James S Speck, *Vertical GaN Devices for High-Power Electronics*, ECS Meeting, H3-1004, October-2021. [Invited]

12. Jingjing Shi, Anusha Krishnan, A.F.M. Anhar Uddin Bhuiyan, Yee Rui Koh, Kenny Huynh, Akhil Mauze, Sai Mu, Brian M. Foley, Habib Ahmad, **Takeki Itoh**, Yuewei Zhang, Chao Yuan, Samuel Kim, W. Alan Doolittle, Chirs Van De Walle, James S. Speck, Mark Goorsky, Patrick Hopkins, Hongping Zhao, Samuel Graham, *Thermal Transport Across Al-$(Al_xGa_{1-x})_2O_3$ and Al-Ga_2O_3 Interfaces*, InterPack, 74116, October-2021.

11. Akhil Mauze, **Takei Itoh**, Esmat Frazana and James S. Speck, *Materials progress for the development of β-Ga_2O_3 for power electronics*, Compound Semiconductor Week , May-2021. [Invited]

10. Akhil Mauze, **Takeki Itoh**, Yuewei Zhang and James S. Speck, *Sn doping of (010) β-Ga_2O_3 films grown by plasma-assisted molecular beam epitaxy*, SPIE photonic west opto, 116870I, March-2021.

9. Esmat Farzana, Fikadu Alema, Wan Ying Ho, **Takeki Itoh**, Andrei Osinsky and James S. Speck, *Vertical β-Ga_2O_3 Schottky diodes from metal-organic chemical vapor deposition with low on-resistance and high average breakdown field*, SPIE photonic west opto, 116870G, March-2021.

8. Atsushi Kobayashi, Masumi Sakamoto, Kyohei Nakamura, Khe Shin Lye, **Takeki Itoh**, Kohei Ueno and Hiroshi Fujioka, *Crystal growth of InN on amorphous substrates towards the fabrication of high-mobility thin-film transistors*, JSPS 162 committee 110th meeting/special symposium, 6, The University of Tokyo, September-2018.

5. Kyohei Nakmura, Atsushi Kobayashi, **Takeki Itoh**, Khe Shin Lye, Mari Morita, Kohei Ueno, Jitsuo Ohta, Yuki Tokumoto and Hiroshi Fujioka, *Fabrication of thin-film transistors based on InGaN film grown at room temperature*, 64th JSAP Spring Meeting, 14a-503-5, Pacifico Yokohama, March-2017.

4. Atsushi Kobayashi, **Takeki Itoh**, Kohei Ueno, Jitsuo Ohta and Hiroshi Fujioka, *Growth of nitride semiconductors on glass substrates and its application for thin-film transistors*, 8th Nitride Semiconductor Crystal Growth Meeting, Mo-19, Kyoto University, May-2016.

3. Atsushi Kobayashi, **Takeki Itoh**, Khe Shin Lye, Kohei Ueno, Jitsuo Ohta and Hiroshi Fujioka, *Characterization of InGaN thin-film transistors fabricated on amorphous substrates*, 63th JSAP Spring Meeting, 21a-H121-9, Tokyo Institute of Technology, March-2016.

2. Khe Shin Lye, **Takeki Itoh**, Atsushi Kobayashi, Kohei Ueno, Jitsuo Ohta and Hiroshi Fujioka, *Room temperature preparation of InN films on polymer substrates by PSD and its application for TFTs*, The 6th International Symposium on Growth of III-Nitrides, We-B57, Hamamatsu, November-2015.

1. Khe Shin Lye, **Takeki Itoh**, Atsushi Kobayashi, Kohei Ueno, Jitsuo Ohta and Hiroshi Fujioka, *Thin-film transistors based on InN grown on polymer sheets at room temperature*, 76th JSAP Fall Meeting,15a-1D-8, Nagoya Congress Center, September-2015.

ABSTRACT

Molecular Beam Epitaxy of β-Ga_2O_3: Growth and Doping

by

Takeki Itoh

Efficient power electronic devices are essential for minimizing power losses during power conversion due to the growing worldwide energy consumption and global warming. Ultrawide bandgap semiconductors show high breakdown voltage to achieve efficient power conversion. In particular, β-Ga_2O_3 has been considered as a promising ultrawide bandgap semiconductor material for next-generation power electronics due to its large bandgap (4.8 eV) and breakdown field (8 MV/cm). The availability of melt-based growth method enables manufacturing of extremely high-quality single-crystal bulk substrates.

The optimization of growth orientations is critical toward high-quality β-Ga_2O_3 epitaxial films. In this study, epitaxial growth of β-Ga_2O_3 films on (110) substrates have been performed via plasma-assisted molecular beam epitaxy (PAMBE). Atomic force microscopy (AFM) scan shows a very low RMS roughness of 0.08 nm for the surface of the as received (110) substrates. High-resolution X-ray diffraction measurements reveal a 2.5 nm/min growth rate of β-Ga_2O_3 films on (110) substrates for conventional PAMBE growth conditions (~700 °C) which is comparable to that of on (010) substrates. The surface morphology of β-Ga_2O_3 epitaxial films is smooth and has a similar dependence on Ga flux as (010) growth. However, the (110) plane does not have tendency to show a well-defined

step-terrace structure in spite of the appearance of (110) facets in growth of (010) β-Ga$_2$O$_3$. Indium catalyzed growth was also demonstrated to improve the growth rate up to 4.5 nm/min and increase the maximum growth temperature up to 900 °C of (110) β-Ga$_2$O$_3$.

The continuous Si doping in β-Ga$_2$O$_3$ epitaxial films grown by PAMBE through the utilization of a valved effusion cell for the Si elemental source. Secondary ion mass spectroscopy (SIMS) results exhibit that the Si doping profiles in β-Ga$_2$O$_3$ are flat and have sharp turn on/off depth profiles. The Si doping concentration was able to be controlled by either varying the cell temperatures or changing the aperture of the valve of the Si effusion cell. Additionally, the High crystal quality and smooth surface morphologies were confirmed on Si-doped β-Ga$_2$O$_3$ epitaxial films grown on (010) and (001) substrates. The electronic properties of Si-doped (001) β-Ga$_2$O$_3$ epitaxial film showed an electron mobility of 67 cm^2/Vs at the Hall concentration of 3.0×10^{18} cm^{-3}.

β-Ga$_2$O$_3$ epitaxial film grown by PAMBE shows outstanding crystal quality. However, the residual nitrogen in the oxygen gas source results in nitrogen incorporation into the β-Ga$_2$O$_3$ epitaxial films. Since nitrogen is a deep acceptor in the β-Ga$_2$O$_3$ materials system, the incorporation of nitrogen will affect the transport properties of β-Ga$_2$O$_3$ films. To identify the nitrogen incorporation level, nitrogen incorporation in β-Ga$_2$O$_3$ films was measured by SIMS with low detection limit of nitrogen. The PAMBE-grown β-Ga$_2$O$_3$ epaxial films showed a nitrogen concentration of 1.0×10^{17} cm^{-3} either by conventional MBE growth and MOCATAXY growth. To prevent the nitrogen incorporation, pure ozone source was used as the oxygen source for the growth β-Ga$_2$O$_3$. The ozone concentration was improved to up to 80% by adding a recirculating line between the MBE and the pure ozone generator.

TABLE OF CONTENTS

I. Introduction to β-Ga₂O₃ and its growth

1.1 Ultra-wide bandgap semiconductor

Power electronic devices are the key components which are applied throughout almost all the electric devices in our lives, from power adapters to electrics vehicles and high-speed rails[1]. Their primary roles are as power converter: switching AC to DC, vice versa, and turning up and turning down the voltages of the electricity. For different usage such as high power and high current rate, proper types of power devices are chosen at particular power/current regions.

Nowadays, people all over the world are making efforts to replace fossil fuels with sustainable energies such as solar energy and wind energy to achieve carbon neutral due to global warming. Moreover, the primary energy form of solar energy and other sustainable energies is electric power, which indicates that the improvement of the proportion of modern life's essentials driven by electric power will be mainstream. One of the most important replacements of fossil fuel-driven instruments such as conventional internal combustion engine vehicles. Moreover, nearly 30% of total greenhouse effect gas emission is from transportation. This emission can be significantly reduced if most of the conventional internal combustion engine cars and trucks are replaced by electric cars and trucks.

The efficiency of the power switches is critical for energy saving during the transmission of electricity. Conventional Si-based power electronics shows a switching efficiency of ~90%. On the other hand, by using semiconductor materials with wide bandgaps such gallium nitride or silicon carbide, the switching efficiency can be pushed up to over 99%[2]

1

with an operation voltage up to over 1000 V. The capability of power electronics that can be used at a high voltage is essential for fast charging of electric vehicles.

β-Ga$_2$O$_3$ has been considered as a promising ultrawide bandgap semiconductor material due to its large energy bandgap (4.8 eV)[3] and high breakdown field (~8 MV/cm)[4]. The ultrawide bandgap semiconductor materials, such AlN and diamond, have larger energy bandgaps than the wide bandgap semiconductors such as GaN (3.4 eV) and SiC (3.3 eV). To measure the potential of a semiconductor material for the application of power electronics, the Baliga's Figure of Merit (BFOM) is widely used[5]. In a power electronic device, the two most important features are the on resistance and the breakdown voltage. A large breakdown voltage is desirable for low energy loss, and a low on resistance is desirable for low heat loss during the operation of the power electronic device. A basic concept of a vertical power electronic device and its corresponding electric field profile can be illustrated as shown in Figure 1.1.
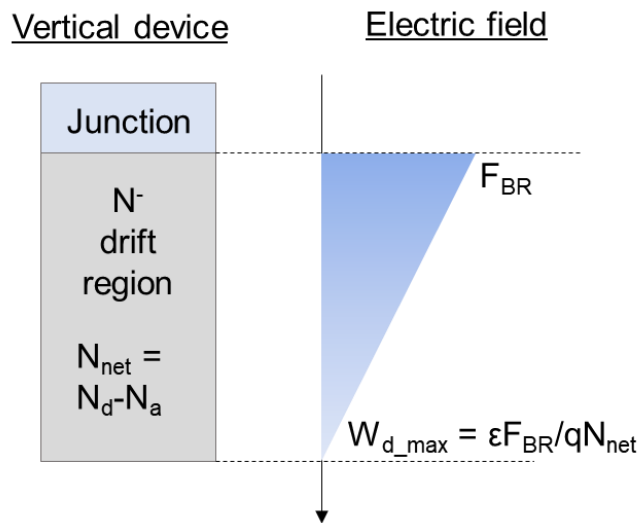
Figure 1.1. A schematic of a vertical semiconductor junction with lightly doped N drift region and the electric field profile when the device is reaching breakdown.

In the drift region of this device, the background doping concentration is expressed by $N_{net} = N_d - N_a$. When this device reaches the breakdown state, which means it can no longer hold the voltage that is applied, the maximum electric field generated at the interface between the junction and the drift region is F_{BR}. Assuming shallow hydrogenic dopants (n = N_d), the on resistance can be shown as the following equation,

$$R_{on} = \frac{W_D}{N_d q \mu} \text{ (eqn. 1.1)}$$

Where W_D is the width of the depletion region. When the device reaches the breakdown state, W_D reaches the maximum width: W_{d_max}. Based on the maximum electric field F_{BR}, $W_{d\_max} = \varepsilon F_{BR}/q N_{net}$. Therefore, the maximum breakdown voltage here can be shown as follows,

$$V_{BR} = \frac{1}{2} F_{BR} W_{d\_max} = \frac{\varepsilon F_{BR}^2}{2q N_{net}} \text{ (eqn. 1.2)}$$

As a result, the Baliga's figure of merit (BFOM) can be expressed as follows,

$$BFOM = \frac{4V_{BR}^2}{R_{on}} = \mu \varepsilon F_{BR}^3 \text{ (eqn. 1.3)}$$

To summarize the important properties, including BFOM. of major semiconductor materials, Table 1.1 is shown as follows,

Table 1.1. Parameters of major semiconductor materials

	Si	4H-SiC	GaN	Diamond	AlN	β-Ga$_2$O$_3$
Band gap (eV)	1.1	3.3	3.4	5.5	6.2	4.8
Electron mobility (cm^{2}V^{-1}s^{-1})	1500	900	1500	2200	420	200
Dielectric constant (ε_r)	11.7	9.7	8.9	5.7	9	10
Breakdown field (MV/cm)	0.3	2.5	3	5.5	15.4	8
Baliga's FOM ($\mu \varepsilon F_{BR}^3$)	1	320	1400	21000	32370	2400

From this summary, diamond shows the highest value of BFOM among all the semiconductor materials. However, as shown in equation (1.3), BFOM is solely determined by the carrier mobility and its breakdown field. This suggests that a semiconductor material with high carrier mobility and large breakdown field is suitable for applications of power electronics. While this is true for an ideal semiconductor material with minimum background impurity concentration and defects, in the real life, semiconductor materials always have issues with impurities and defects due to the lack of methods to produce materials without imperfections.

While BFOM is based on the assumption that the donors are hydrogenic and the carrier concentrations are not affected by background compensation, this FOM can be modified to reflect the real activation energies of donors and background carrier concentrations. The first effect from imperfection to be considered is the incomplete ionization due to deep donor/acceptor levels for certain semiconductor materials such as AlN and diamond. Here, the value of the on resistance: R_{on}, need to be expressed as,

$$R_{on} = \frac{N_d}{n} \frac{4V_{BR}^2}{\mu \varepsilon F_{BR}^3} \text{ (eqn. 1.4)}$$

This form of on resistance is derived from the BFOM in eq. 1.3, and N_d/n is a coefficient to define the ratio of ionization. Therefore, a modified BFOM that takes the incomplete ionization due to deep donor/acceptor levels into consideration should be expressed as follows,

$$Modified\ BFOM = \frac{4V_{BR}^2}{R_{on}} = \frac{n}{N_d} \mu \varepsilon F_{BR}^3 \text{ (eqn. 1.5)}$$

The second effect from the material's imperfection is the background compensation from the impurities and native defects. To reflect this background compensation effect to the

4

BFOM, the charge neutrality equation should be used to derive the carrier concentration prefactor,

$$n + N_a = \frac{N_d}{1 + g_d \exp\left(\frac{(E_F - E_d)}{k_B T}\right)} \quad \text{(eqn. 1.6)}$$

Where g_d is the degeneracy factor, E_d is the activation energy of the donor state, and k_B is Boltzmann constant. To derive the value of electron concentration n, solve the charge neutrality equation for n to get the following equation with the electron concentration derived from the conduction band density of state: $n = N_c \exp(-(E_c - E_F)/k_B T)$,

$$n = \frac{-\left(N_c \exp\left(-\frac{\Delta E_d}{k_B T}\right) + g_d N_a\right) + \sqrt{\left(N_c \exp\left(-\frac{\Delta E_d}{k_B T}\right) + g_d N_a\right)^2 + 4 g_d N_c \exp\left(-\frac{\Delta E_d}{k_B T}\right)(N_{net})}}{2 g_d}$$

(eqn. 1.7)

Where ΔE_d is the ionization energy of the donor level from the conduction band minimum, and N_c is the effective density of state of conduction band. Assuming the value of $N_c \exp\left(-\frac{\Delta E_d}{k_B T}\right)$ is small, $n/N_{net} = N_c \exp\left(-\frac{\Delta E_d}{k_B T}\right)/g_d N_a$.

Therefore, the modified BFOM that includes the effect from the incomplete ionization and background compensation can be expressed as follows,

$$Modified\ BFOM = \frac{n}{N_{net}} \mu \varepsilon F_{BR}^3 = \frac{N_c \exp\left(-\frac{\Delta E_d}{k_B T}\right)}{g_d N_a} \mu \varepsilon F_{BR}^3 \quad \text{(eqn. 1.8)}$$

The relationship between breakdown voltages and on-resistance R_{on} considering the incomplete ionization and background compensation levels of different semiconductor materials are plotted in figure 1.2. The plot of GaN over 10 kV is not available due to the low purity of materials due to carbon incorporation, which results in low breakdown voltage.

5
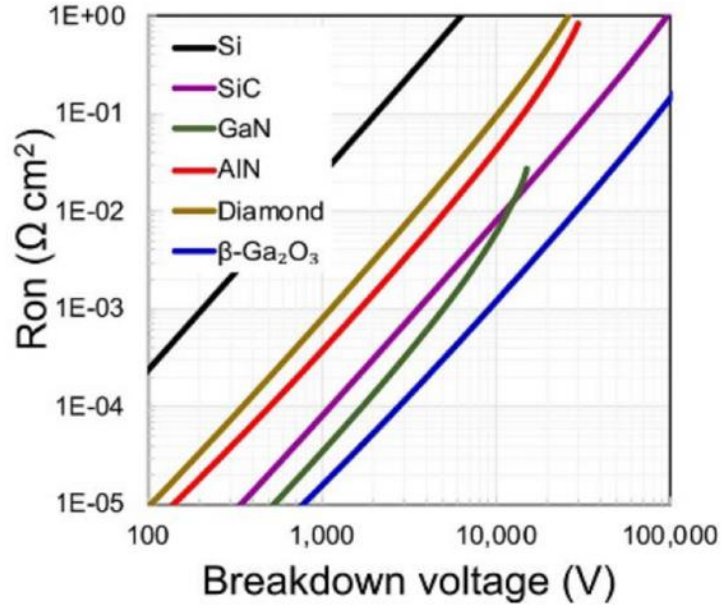
Figure 1.2. The relationship between breakdown voltage (V_{BR}) and on resistance (R_{on})of different types of semiconductor materials based on the effect from incomplete ionization and background compensations due to impurities in the materials[6].

As a result, from Figure 1.2, β-Ga$_2$O$_3$ significantly outperforms other wide-bandgap semiconductor materials for power applications when the doping abilities and materials purity limitation are taken into consideration[6]. While the donor or acceptor activation energy are the intrinsic properties of the semiconductor materials that cannot be changed or improved, the purity of the materials can be obtained from the advancement of epitaxial growth methods and availability of single-crystal bulk substrates. Therefore, the development of crystal growth technology of semiconductor materials with large energy bandgap and shallow hydrogenic dopants is critical for the adoption of efficient power electronics devices. β-Ga$_2$O$_3$ has the availability of shallow donors and high quality bulk substrates with low density threading dislocations, which are advantages over other wide bandgap semiconductor materials.

6

1.2 Bulk growth methods for β-Ga$_2$O$_3$

Compared to other wide bandgap semiconductor materials, one of the most significant advantages of beta gallium oxide is the availability of bulk substrates grown by melt methods. This capability is not only critical to the crystal growth of high-quality β-Ga$_2$O$_3$ epitaxial film, but also to the adoption of β-Ga$_2$O$_3$-based power electronics. Since quality control is the most important part of power electronics, which requires high reliability during the operation in a transportation method such as electric vehicle and high-speed train.

The melt growth methods for β-Ga$_2$O$_3$ bulk crystals include edge-defined film fed growth (EFG) methods, Czochralski method, floating zone method, and Vertical Bridgeman method. Among all these four bulk growth methods, EFG method is currently the most promising method due to its high quality and uniformity of the manufactured bulk substrates[7]. Currently, bulk substrates with the crystal orientations of (010), (001) and ($\bar{2}$01) are commercially available from Novel Crystal Technologies. While the [010] zone is a scalable orientation in β-Ga$_2$O$_3$ crystal system by EFG method, both (100) and (001) orientations are in the [010] zone, which means they are suitable for large-scale bulk substrates. Moreover, even 100 mm diameter of (001) β-Ga$_2$O$_3$ oriented wafers are commercially available. The density of threading locations is as low as 1×10^3 cm^{-2} [7], which is much lower than other wide-bandgap semiconductor materials such as GaN bulk substrates. This high-quality bulk substrate with low threading dislocation density leads to high breakdown voltages for power electronic devices. However, the production cost of the EFG method is a major issue. Due to the loss of iridium from the crucible during the growth process of the β-Ga$_2$O$_3$ bulk materials, the cost cannot be easily reduced without significant improvement of the melting growth method.

Czochralski method is another melt growth method that currently provides commercially available bulk substrates[8]. Since the melt surface area of Czochralski method is much larger than that of the EFG method, it is expected that Czochralski method can reduce the production cost of β-Ga$_2$O$_3$ bulk materials and high-quality substrates. However, since the surface area is large, the evaporation of β-Ga$_2$O$_3$ is also large during the process of bulk materials growth. This brings loss of β-Ga$_2$O$_3$ and introduces impurities and defects into the bulk materials, which leads to lower crystal quality than that of the EFG method.

The Floating zone method[9] and vertical Bridgman[10] method are currently both under development for large area and high-quality bulk growth of β-Ga$_2$O$_3$ single-crystal materials in order to reduce the ultimate production cost of β-Ga$_2$O$_3$ bulk substrates. Since the floating zone method has a relatively small area of hot zone compared to EFG and Czochralski methods, the size limitation still needs to be overcome. On the other hand, vertical Bridgman method is showing progress toward the fabrication of large area bulk substrates. Y. Ueda et al demonstrated a two-inch Fe-doped β-Ga$_2$O$_3$ bulk wafer grown by vertical Bridgman method[10], showing reasonable low FWHM values across the whole wafer. Since the vertical Bridgman method can reuse its crucible and the growth is operated in the air, this method can be another promising method to reduce the production cost of β-Ga$_2$O$_3$ bulk substrates.

1.3 Epitaxial growth methods for β-Ga₂O₃

Epitaxial growth of β-Ga$_2$O$_3$ films with remarkable crystal quality has been achieved on various orientations of single-crystal substrates by metal organic chemical vapor deposition (MOCVD)[11,12], hydride vapor phase epitaxy (HVPE)[13,14] and molecular beam epitaxy (MBE)[15–17]. Recent reports have shown that MOCVD grown β-Ga$_2$O$_3$ films exhibited low

temperature electron mobility of $\sim 10^4$ cm/Vs[12,18], while other research by MOCVD reported carrier concentration as low as $\sim 2 \times 10^{14}$ cm^{-3} [19]. β-Ga$_2$O$_3$ films grown by HVPE show relatively fast growth rate compared to the other two growth techniques, but the surface morphology of as-grown bulk materials remains rough. The rough surface can be resolved by chemical-mechanical polishing to obtain smooth surface morphology. However, there is still much improvement to be made in materials' quality and electronic properties. Additionally, growth methods such as mist-CVD[20], atomic layer deposition (ALD)[21,22], and pulse laser deposition (PLD)[23,24] are also available for epitaxial growth of β-Ga$_2$O$_3$ films on either native or foreign substrates. Mist-CVD is a growth method that utilizes ultrasonic mist reactant to grow materials and the cost is considered to be lower than other growth techniques. The research focus of mist-CVD method has been targeted on the alpha phase Ga$_2$O$_3$ on sapphire substrates due to the lower cost compared to the native substrates. However, growth attempts on β-Ga$_2$O$_3$ substrates have also been performed to obtain relatively high crystal quality β-Ga$_2$O$_3$ films. ALD has been known for its precise thickness control and high crystal quality growth of oxide films. However, the low growth rate due to its process of growth by single atomic layers has limited its research activities. On the other hand, PLD played a major role in the early stage of the research of growth techniques for BGO. The crystal quality of PLD-grown materials, however, is lower compared to other growth methods due to the ion damage generated during the growth. Achieving an extremely smooth surface morphology of β-Ga$_2$O$_3$ films is essential to minimize interface scattering in the channels of such lateral devices and is particularly important for modulation-doped field effect transistors (MODFETs) that utilized the β-(Al$_x$Ga$_{1-x}$)$_2$O$_3$/β-Ga$_2$O$_3$ heterostructure[25,26].

1.4 Basics of molecular beam epitaxy

Molecular beam epitaxy of is one of the primary epitaxial growth methods for beta-gallium oxide films. Due to its capabilities of growing high-purity epitaxial films and its flexibility of using different types of elemental sources, the first demonstration of β-Ga$_2$O$_3$-based MOSFET was realized by utilizing MBE-grown films as channel material. This breakthrough triggered enormous interest in this field since beta gallium oxide was not known as a material that works for semiconductor devices. Epitaxial growth of β-Ga$_2$O$_3$ by other growth methods such as MOCVD and HVPE have been developed after the emerging interest in this semiconducting material. Compared to these two growth methods, MBE maintains the following advantages: flexibility of source materials of III-group metals, oxidizers such as oxygen and ozone. Moreover, the choice of dopants is also flexible with a reasonable vapor pressure inside the chamber provided by either solid or liquid elemental materials. On the other hand, MBE requires ultra-high vacuum (UHV) pressure. The MBE system needs to be sealed by high-quality materials and gaskets between the connections of components. To maintain the vacuum inside the chambers, the MBE system needs to be constantly pumped by different types of pumps at different pressure ranges. For the stage that holds the sample for growth, a rotation motor is attached to it for rotating the sample to achieve uniform growth of epitaxial films. A pyrometer is attached to a port that faces the sample to measure the temperature of the growth sample by the infrared radiation. The pyrometer is calibrated by monitoring the melting of an Al deposited on the β-Ga$_2$O$_3$ substrate. Since the melting point of Al is 660.3 °C, the emissivity is calibrated when the Al metal starts to melt by slowly heating the substrate. Since β-Ga$_2$O$_3$ has different thermal conductivity on its different orientations, the calibration should be performed on all the

crystal orientations that are to be grown in the MBE system to accurately measure the temperature of the β-Ga$_2$O$_3$ substrates.
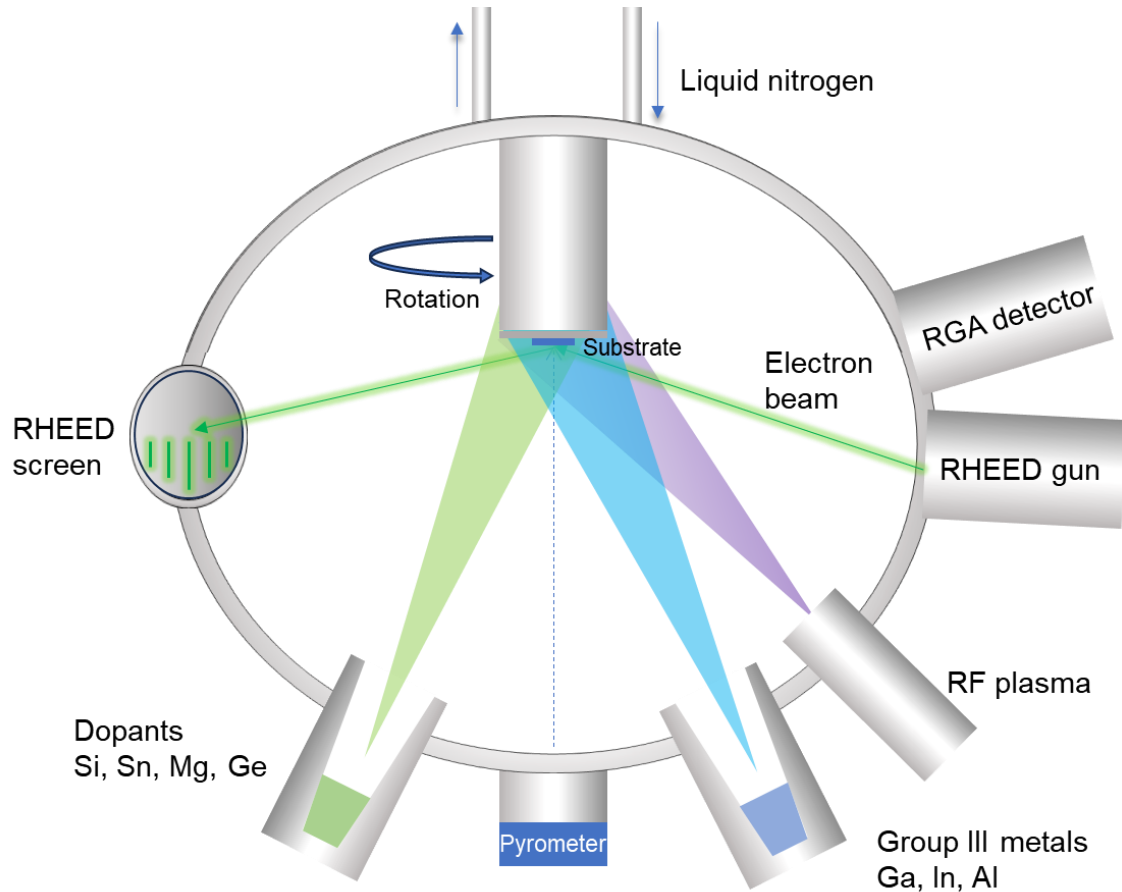
Figure 1.3. A schematic of the MBE system for β-Ga$_2$O$_3$ epitaxial growth

Figure 1.3 is a schematic of an MBE system built for the purpose of epitaxial growth of beta-gallium oxide. The MBE system is called a "vertical system" since the substrate for growth and the effusion cells are aligned vertically. On the other hand, a system with the substrate and the effusion cells are aligned horizontally is called a "horizontal system". The advantages of a vertical system are the ease of using any kind of source materials at any position. Since all the effusion cells are mounted vertically to the MBE system, there is no

need to worry about the source materials in either liquid or solid phase cannot hold itself due to the direction of the gravity. The horizontal system provides ease of maintenance due to the space that can be used to hold and transfer the effusion cells.

In particular, an oxide MBE system needs to consider the oxidation of source materials in the effusion cells. A typical background O pressure during the growth of beta-gallium oxide is approximately 1×10^{-5} Torr. The metal source, either in the solid phase or liquid phase in the oxidation environment can be oxidized during the growth of metal-oxide films. In the case of Ga effusion cell, the formation of Ga suboxide (Ga_2O) does not prevent the further generation of Ga flux the Ga source since Ga_2O is also in gas phase at this temperature/pressure range. This contributes to the stability of the epitaxial growth of beta-gallium oxide. For In source material, the operation temperature: 800℃, is also in the range when it is in the liquid phase. On the other hand, the aluminum source can be quickly oxidized to form Al_2O_3 at the interface between the outgoing Al flux and incoming oxygen environment. The formation of solid Al_2O_3 can block the path of outgoing Al flux from the effusion cell. To overcome this issue, the Al_2O_3 formed near the opening of the effusion cell can be heated up to 1200 ℃ to be baked off. After this, the Al flux can recover to the previous level.

Reflection high energy electron diffraction (RHEED) system is the most common way to monitor the surface during epitaxial growth, which is attached to the MBE system. An electron gun with acceleration voltage up to 15 kV and filament current up to 1.5 A. This RHEED electron gun is differentially pumped by an ion pump to prolong the lifetime of the filament. On the opposite side of the MBE chamber, a fluorescence screen that is made of P43 phosphor is used to show the diffraction from the growth sample. The diffraction

patterns on the RHHED screen show the surface morphologies and growth modes of the sample. When the growth is in 2D mode, which corresponds to smooth surface morphology, the diffraction of electrons shows streaky patterns on the screen. On the other hand, when the growth is in 3D mode, which corresponds to rough surface morphology, the diffraction patterns become spotty.

To ensure the reproductivity of MBE growths over time, a beam flux monitor is crucial to the MBE system. The fluxes from the effusion cells are measured by the Bayard-Alpert type ionization gauge equipped on the beam flux monitor. The position of the ionization gauge should be close to the location of the growth substrate to obtain the fluxes that are actually going into the sample. Here, the ionization gauge measures the fluxes from the effusion cells as the beam equivalent pressure (BEP). This is a local pressure that is measured as a directional gas beam on a surface. This concept is used to define fluxes such as Ga flux, In flux, and Al flux in this study. This pressure is determined by the pressure obtained from the ionization gauge when only one effusion cell' shutter is open, subtracted by the pressure when no effusion cell is open. Since the beam flux needs time to stabilize after opening the shutter of an effusion cell, the BEP should be obtained when the pressure showing on the ionization gauge is stabilized. Moreover, gettering might happen when a metal source effusion cell is open to cause the drop of the background vacuum pressure. The BEP value of a certain metal source should be obtained when both the background pressure and the pressure from the effusion cells are stabilized.

To monitor the type of gas species that are existing in the main growth chamber, a residual gas analyzer (RGA) is attached to the MBE system. The RGA detector provides a spectrum from partial pressures of atomic mass unit (amu) 1 to 65 to obtain the information

of different types of molecules. This information can help determine whether the system has a leak to the atmosphere by observing the ratio of oxygen and nitrogen partial pressure. Additionally, RGA can monitor certain types of molecules over time while the MBE system is under a process such as baking and leak check. For a UHV system like MBE, using helium gas to check the locations of leak is the primary method. Since helium only exists at a very low concentration in the air, it has a low background level so that it doesn't affect the vacuum too much when it gets through a leak point. Moreover, helium gas has a low atomic mass, so it is relatively mobile in the system, and it is not reactive. However, helium gas can only be used at a vacuum of UHV level.

The most important feature of an MBE system is the ultra-pure growth environment. To achieve this pure environment, ultra-high vacuum is needed in the system. In an MBE system, a turbo molecular pump is usually the primary choice for the pumping of the main growth chamber. The turbo molecule pump can pump the system down to the 1×10^{-11} Torr level. Turbo pump needs help from a rough pump such as a scroll pump or an oil pump to reach low vacuum first, then the turbo can be started by speeding up the blades to its operation speed. Since the blade speed of the turbo pumps is in the 30,000 rpm to 60,000 rpm range, the turbo pump needs time to speed up to reach its normal operation state.

Cryo pump is another popular choice for UHV pumping in an MBE system. By condensing the gas species in the atmosphere on the cold stages inside the pump, the cryo pump can provide fast and clean pumping in a certain vacuum level range. On the other hand, non-condensable gas species such as hydrogen, helium and neon can be pumped by either using a turbo pump or on the 15 K cryopanel with porous materials attached. In addition, since the gas species are condensed on the cryopanel, the cooling efficiency by the

14

helium compressor drops as the condensed gas accumulates on the surface of the cryopanel. Therefore, monitoring the temperature of the cryo pump is necessary during the usage of the over time. When the temperature of the cryo pump goes over a certain point, the pump needs to be regenerated by stopping the compressor to allow the cryopanel heat up to room temperature. During this process, the gas species condensed on the cryopanel vaporizes as the temperature goes above their boiling point. This process needs an external pumping such as a scroll pump or an oil pump to exhaust the vaporized gas species. After this regeneration process, the cryopump can be restarted by starting the helium compressor and reach a temperature of under 10 K. The cryopump needs to be started at a medium vacuum level, such as a 1×10^{-3} Torr to 1×10^{-5} Torr range. In this case, the MBE system can be pumped by a scroll pump, then a small turbo pump followed by a large main turbo pump.

Additionally, an ion pump can be used for pumping UHV pressure. Compared to a turbo pump and a cryopump, ion pump is less used in the modern MBE systems due to its lower starting operation vacuum level than the other two types of vacuum pumps. However, it can reach UHV pressures to as low as 1×10^{-11} Torr by sputtering a metal getter, usually made of titanium. The metal getter reacts with gas species such as hydrogen, nitrogen, oxygen and carbon dioxide.

1.5 Fundamentals of β-Ga$_2$O$_3$

The crystal structure of β-Ga$_2$O$_3$ is monoclinic with a space group of C2/m. In a single unit cell, there are 8 gallium atoms and 12 oxygen atoms. Figure 1. 4 shows the crystal structure of β-Ga$_2$O$_3$ with a β angle of 103.87°, a = 12.21 Å, b = 3.04 Å, and c = 5.81 Å[27]. There are two types of coordination for Ga ions sitting in this structure: the tetrahedral site

and the octahedral site. In the case of O ions, there are three types of coordination. One of them has four-fold coordination and two of them have three-fold coordination. The (100), (010), (001) crystal planes are also shown in Figure 1.4. The (100) and (001) planes don't include the β angle, while the (010) plane provides right angle in the out-of-plane direction.
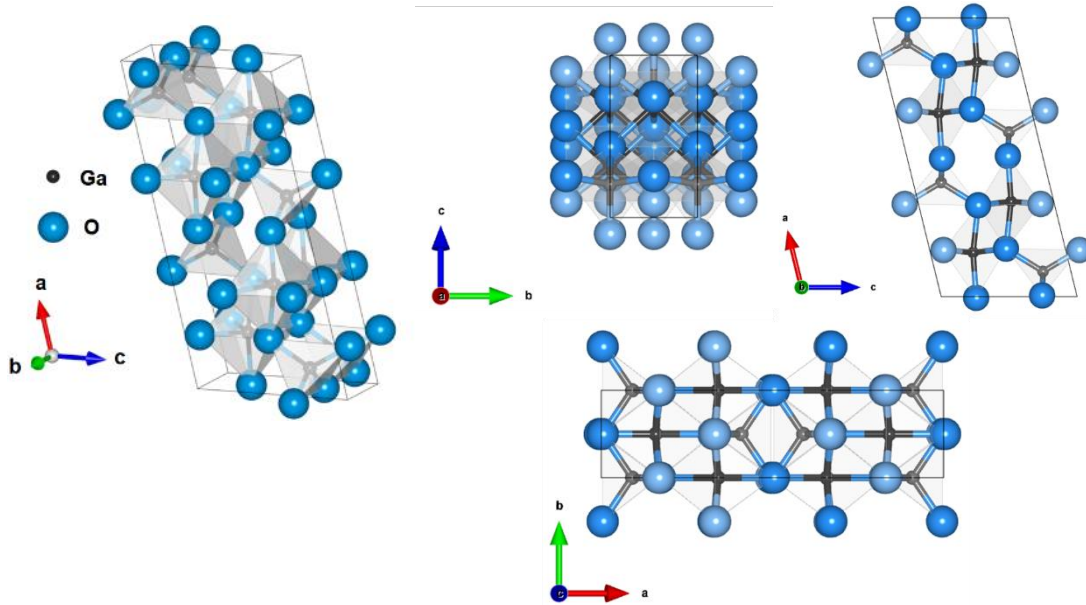
Figure 1.4. The crystal structure of β-Ga₂O₃ and its views from a, b, and c orientations

The anisotropic properties of β-Ga₂O₃'s crystal structure requires different effort of bulk growth, epitaxial growth, and characterization on every orientation. In particular, the crystal planes in the [010] zone axis such as (100) and ($\bar{2}$01) are cleavage planes, which show significantly lower growth rate than other planes during epitaxial growth. On the other hand, (001) plane in the [010] zone axis can be scaled up to large-area bulk substrates with a diameter of 4 inch to 6 inch[28]. The thermal conductivity of β-Ga₂O₃ has the anisotropic properties[29], and [010] direction has the highest thermal conductivity among [100], [001], and [$\bar{2}$01] directions.

1.6 MBE growth of β-Ga₂O₃

Epitaxial growth of high-quality β-Ga$_2$O$_3$ films by MBE on bulk substrates has been demonstrated on different crystal orientations such as (100), (010), (001) and ($\bar{2}$01)[4,13,15,30]. The primary growth parameters for a plasma-assisted MBE-grown β-Ga$_2$O$_3$ epitaxial films include substrate temperature, Ga flux (BEP), oxygen background pressure, and plasma power. Among these parameters, Ga flux is the dominant parameter to affect growth rate, crystal quality and surface morphology of β-Ga$_2$O$_3$ epitaxial films. Figure 1.5 (a) shows the growth rate dependence on Ga flux of β-Ga$_2$O$_3$ epitaxial films grown on (010) substrates at a substrate temperature of 700 ℃. As the Ga flux increases, the growth rate increases linearly in the oxygen-rich region. When the growth regime passes the stoichiometric point, the growth rate stays constant even though the Ga flux increases. This constant growth rate in the Ga rich region can be explained by the temperature dependent suboxide desorption reaction between the Ga atoms and β-Ga$_2$O$_3$ that is shown by the following reaction,

$$4Ga + Ga_2O_3 \rightarrow 3Ga_2O \text{ (eqn.1.9)}$$
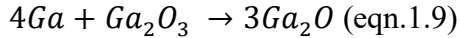
The excessive Ga atoms from the Ga effusion cell react with the β-Ga$_2$O$_3$ films and generate volatile suboxide Ga$_2$O, which reduces the growth rate of β-Ga$_2$O$_3$ to a constant value by MBE. The further increased Ga flux can result in decreasing growth rate with increasing Ga flux[31].

The crystal orientations of substrates for epitaxial growth are one of the most important factors that determine the growth rate, crystal quality, and surface morphology. In figure 1.5 (b), the Ga fluxes dependence of the growth rates on (100), (010), and (001) substrates are shown. The growth rates of β-Ga$_2$O$_3$ epitaxial films on (100) is the lowest among these three orientations since it is a cleavage plane. Also, the negative growth rates on the (001)

17

orientations are indicative of suboxide desorption without the existence of atomic oxygen generated by plasma.
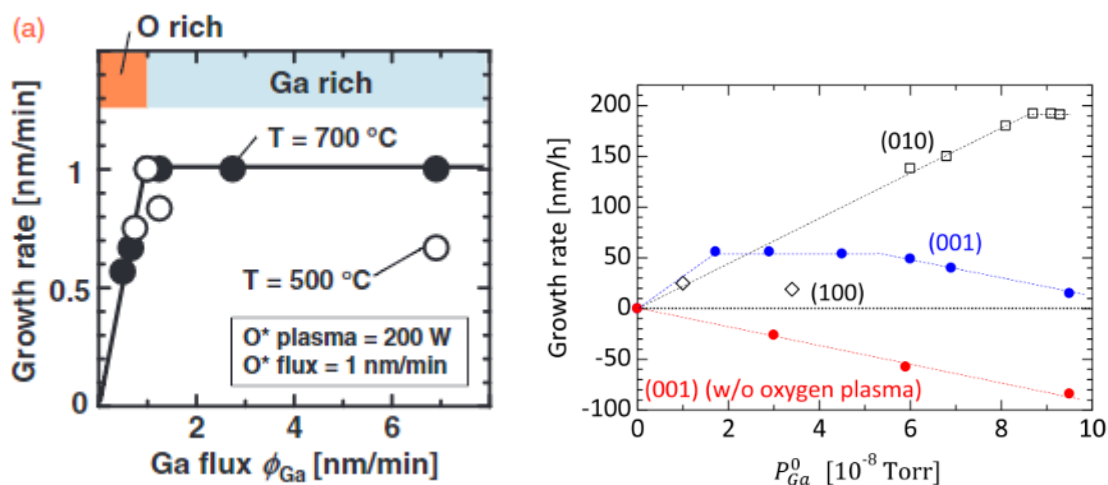
Figure 1.5. (a) The growth rate dependence of β-Ga$_2$O$_3$ epitaxial films on different Ga fluxes[16] and (b) different crystal orientations of β-Ga$_2$O$_3$ substrates[32].

The growth rates and crystal quality depend on the growth temperature and growth conditions such as Ga/O ratio and substrate orientations. The limitation of growth rates is due to the high suboxide desorption reaction at high substrate temperatures. The crystal orientations of β-Ga$_2$O$_3$ substrates are also important for optimizing the growth of since the suboxide desorption rates are different on the crystal orientations.

1.7 Metal-oxide catalyzed epitaxy (MOCATAXY) growth of β-Ga$_2$O$_3$

The limitations of conventional MBE growth of β-Ga$_2$O$_3$ epitaxial films have been the growth temperature and growth rate due to the high suboxide desorption rate at high growth temperatures or high Ga fluxes. This suboxide desorption, however, can be suppressed by

utilizing metal-exchange mechanism between In and Ga to achieve higher growth rate. Since this growth method involves a metal species that eventually acts as a catalyst, it can be called metal-oxide catalyzed epitaxy. During the epitaxial growth of β-Ga$_2$O$_3$, In flux can be supplied to enhance the growth. The first stage of this growth is the incorporation between In atom and O. While Ga only reacts with atomic O generated by such as plasma, In atom can also react with O molecules. Therefore, the reaction between In and O that forms indium oxide can have a higher growth rate than that of gallium oxide. The second stage of this catalyzed growth is the exchange of In and Ga atoms in the indium oxide films. Since the bonding strength of Ga-O is larger than that of In-O, the Ga atoms preferentially incorporated into the film to form β-Ga$_2$O$_3$. This series reactions can be expressed by the following equations,

$$2In + 3O \rightarrow In_2O_3 \text{ (eqn.1.10)}$$

$$2Ga + In_2O_3 \rightarrow Ga_2O_3 + 2In \text{ (eqn.1.11)}$$
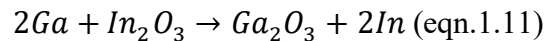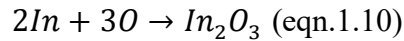
Consequently, the In atoms are not consumed during this process, which shows that In acts as a catalyst in this epitaxial growth mechanism. In this process, the formation of volatile suboxide Ga$_2$O is suppressed, which results in availability of growth at higher growth temperatures and higher growth rates than conventional MBE growth.

Therefore, the film grown by this growth technique results in higher growth rate than those of conventional MBE-grown films. Figure 1.6. shows the growth rates on conventional MBE-grown films and MOCATXY-grown films on (010), (001) and ($\bar{2}$01) orientations. While the growth rates of β-Ga$_2$O$_3$ epitaxial films by conventional MBE is around 2.5 nm/min, MOCATAXY growth has growth rates up to 5.0 nm/min on (010) and (001) orientations, which are two times higher than that of conventional MBE growth. In addition,

the maximum growth temperature of MOCATAXY is expanded to 950 ℃ for the (010)

orientation compared to 700 ℃ of the conventional MBE growth.
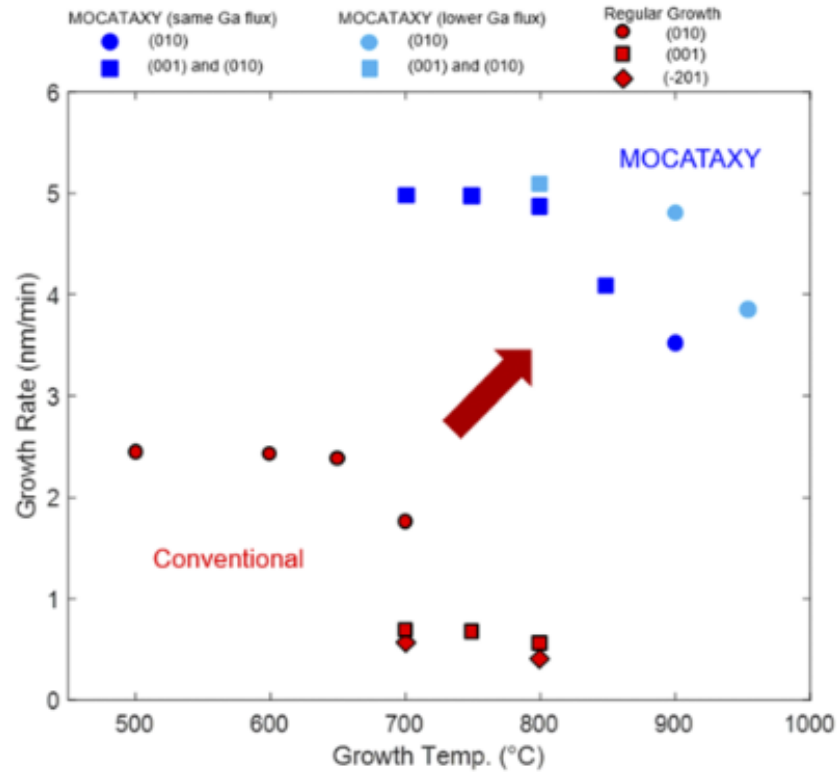
Figure 1.6. Temperature dependence of growth rates on different orientations by MOCATAXY growth on (010) and (001) substrates[17].

1.8. n-type dopants of β-Ga₂O₃

In the β-Ga$_2$O$_3$ systems, shallow hydrogenic donors such as Si, Ge, and Sn are available

for n-type doping. Since there are two sites of Ga atom exists in the β-Ga$_2$O$_3$ unit cell, the

donor level can vary depending on which Ga site is occupied by the dopant atoms. When the

dopant occupies the tetrahedral coordination of the Ga site, the dopant shows a shallower

donor level than the octahedral coordination of the Ga site[33]. The activation energies for Si

and Ge are experimentally determined to be 30 meV[33]. On the other hand, the donor state for Sn is derived by low-temperature Hall measurement showing a value of 77 meV, which is relatively deep compared to the other two donors. This result corresponds to the density functional theory calculation showing that Si and Ge are preferentially incorporated into the tetrahedral coordination of Ga site due to a lower formation energy, while Sn is preferentially incorporated into the octahedral coordination of Ga site[34].

In the growth process of n-type doping by MBE, these three donors show different behaviors when the growth conditions are varied. Ge doping[35] and Sn doping[36] in β-Ga$_2$O$_3$ epitaxial film grown by PAMBE has been studied. To accurately control the doping concentration in β-Ga$_2$O$_3$ epitaxial films, the temperatures of the effusion cells were varied. The SIMS results of Sn doping in conventional growth of β-Ga$_2$O$_3$ epitaxial films by MBE showed doping delay and surface segregation effect at a Sn concentration lower than 1×10^{18} cm^{-3}. However, it is important for the Sn doping concentration to be controllable in a range under 1×10^{17} cm^{-3} to achieve the lightly doped n-type drift layer for vertical devices. Figure 1. 7 shows the Sn and Ge concentrations dependence on effusion cell temperatures. From SIMS results of Sn-doped films, the controllability of Sn concentration is limited as the concentration changes one order of magnitude as the effusion cell temperature only changes 25℃. The SIMS Ge concentration of Ge-doped β-Ga$_2$O$_3$ epitaxial films showed no dependence on the effusion cell temperatures. While this might be explained by the suboxide desorption behavior at higher temperatures, detailed study is needed to understand the doping behavior of Ge in β-Ga$_2$O$_3$ epitaxial films.
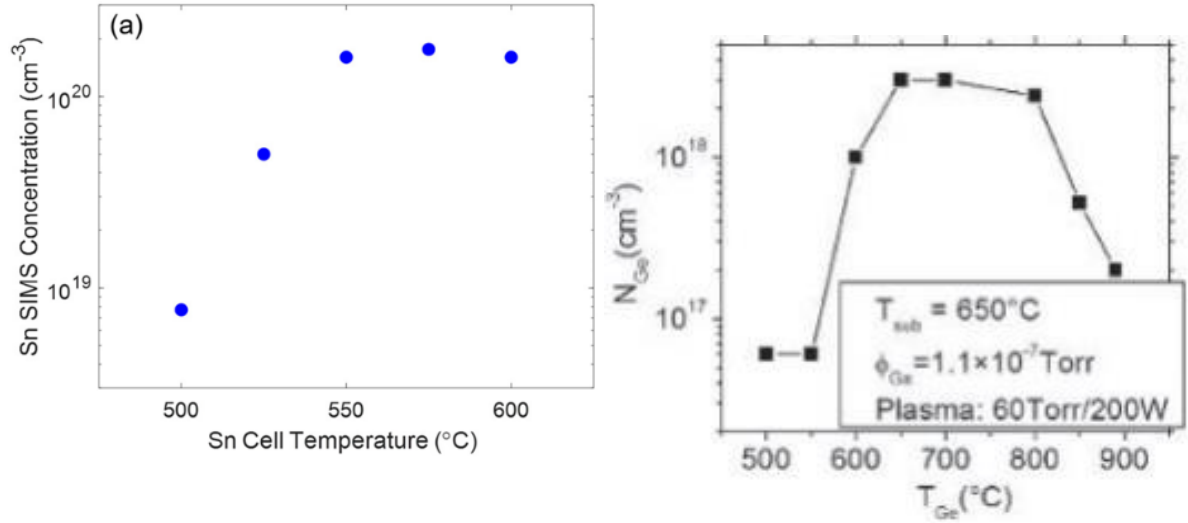
Figure1.7. Effusion cell temperature dependence of SIMS concentrations of Sn doped[36] and Ge doped β-Ga$_2$O$_3$ epitaxial films[37].

On the other hand, Sn-doped β-Ga$_2$O$_3$ epitaxial films grown by MOCATAXY showed flat doping profiles and sharp turn on/off features without doping delay or surface segregation effects. Even though the temperatures of the Sn effusion cell are higher than that of the conventional MBE growth, Sn concentration was controllable under the range of 1×10^{17} cm^{-3}, which is a desirable doping range for low background carrier concentrations for high-performance device fabrication. Since the Sn suboxide SnO is volatile gas and its vapor pressure is high when the source is at a relatively low temperature[38], the higher Sn effusion cell temperature might result in more elemental Sn atoms to incorporate into the β-Ga$_2$O$_3$ epitaxial film, which help the doping avoid delay and surface segregation. Additionally, the self-compensation effect that occurs at the Sn doping range of $>1\times10^{20}$ cm^{-3} leads to resistive films. This makes it difficult to achieve Sn-doped layers with high conductivity to achieve contact layers with low resistivities.

1.9 Acceptor doping in β-Ga₂O₃

For β-Ga$_2$O$_3$, all the available acceptors: Fe, Mg, and N have deep acceptor levels. Fe is mainly used to produce semi-insulating bulk substrates by melt methods such as EFG. The acceptor level of Fe is shown to be approximately 0.8 eV below the conduction band minimum by DFT method[39] and experiment[33]. However, it is not available through an epitaxial growth method like MOCVD due to the difficulty of the preparation of source materials. In addition, Fe shows significant surface segregation effect[40] during the epitaxial growth, which makes the intentionally doping concentration uncontrollable by MBE growth. N is promising for acceptor doping in β-Ga$_2$O$_3$ by MOCVD[30,41] and ion implantation[42,43], but it has not been realized by MBE due to lack of solid or liquid phase source. Mg doping has also been demonstrated by MOCVD[44] and ion implantation[43]. Doping by MBE[45] shows relatively high quality and ideal doping profile compared to the other two growth methods.

Figure 1.8 shows the Arrhenius plot and the SIMS result of the Mg doping profile at different Mg effusion cell temperatures. From the Arrhenius plot, the Mg concentrations exhibit an apparent activation energy of 3.0 eV. This indicates that the Mg doping behavior is well controlled, and the Mg doping concentration range can be varied from 1×10^{16} cm^{-3} to above 1×10^{20} cm^{-3}. From the SIMS doping profile at different Mg effusion cell temperatures, flat doping profile and sharp turn on/off features were obtained at the doping range from 1×10^{16} cm^{-3} to 1×10^{20} cm^{-3}. The accurately controlled Mg doping concentration provides the flexibility for fabrication of high-performance power electronic devices that need semi-insulating regions and layers for the formation of current blocking layers.
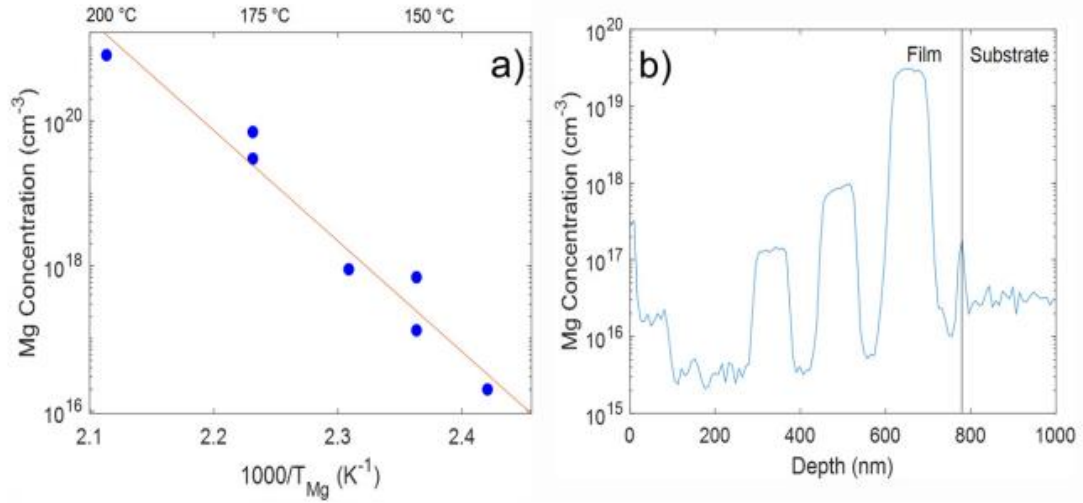
Figure1.8. (a) Arrhenius plot of Mg SIMS concentration relationship with the Mg effusion cell temperatures and (b) SIMS profiles of Mg concentrations at different temperatures[45].

Moreover, the Mg concentrations in β-Ga$_2$O$_3$ epitaxial films show nearly no dependence on the growth temperatures and Ga fluxes during the growth by MBE, which means that the process of Mg doping is robust enough to control Mg concentrations by solely changing the Mg effusion cell temperatures.

On the other hand, the diffusion behavior of Mg in the β-Ga$_2$O$_3$ films is critical toward the fabrication of β-Ga$_2$O$_3$-based power electronics since the device fabrication process needs different temperatures at different process stages. Figure 1.9. shows the SIMS profile of Mg-doped β-Ga$_2$O$_3$ samples that are annealed at different temperatures and times. The Mg spike at the interface between the substrate and the epitaxial layer is due to the contamination from the atmosphere during the handling of the substrates. While the sample without annealing showed a flat Mg profile with a concentration of 2×10^{20} cm^{-3} and the background Mg level of 1×10^{15} cm^{-3}, the annealed samples showed diffusion and the across

24

the samples including the epitaxial films and substrates, and the background level changed to above 1×10^{18} cm^{-3}. As the annealing temperatures and times become longer, the background level and the surface accumulation of Mg get larger, while the concentration of Mg doped layer becomes lower.
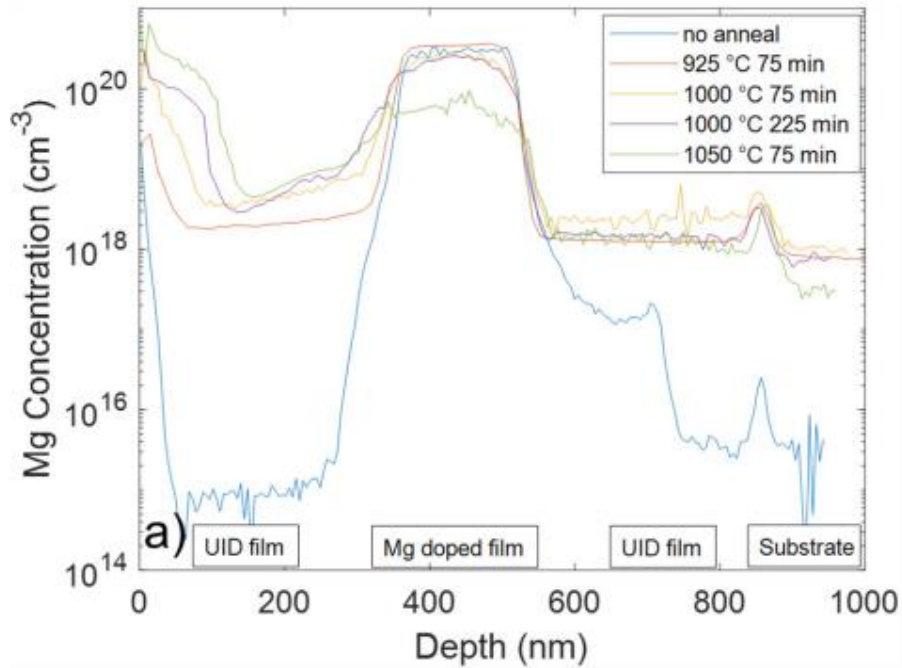
Figure 1.9. SIMS profile a Mg-doped β-Ga$_2$O$_3$ samples annealed at different temperatures[45].

The diffusion mechanism was derived from the SIMS profiles of the annealed samples combined with the DFT calculation results. Peelaers et al. predicted that Mg atoms to diffuse as a extremely mobile donor intersitial speices (Mg$_i$)[46]. On the other hand, for the Mg atoms that are incorporated into the Ga site as an acceptor, this diffusion process needs to be initiated by the interaction with an existing intersitial Ga (Ga$_i$) as the following reaction: Mg$_{Ga}$ + Ga$_i$ $\rightarrow$ Mg$_i$ +Ga$_{Ga}$. This process can also be initiated by the interaction with a Ga

vacancy (V_{Ga}), but it is less favourable due to the formation energy of V_{Ga} and the repulsion between V_{Ga} and Mg_{Ga}.

Nitrogen is considered to be a deep acceptor in the β-Ga_2O_3 materials systems[43,47]. The application of nitrogen doping in a certain area of a power device can perform as current blocking layers, especially in current aperture MOSFETs. Demonstration of current aperture MOSFET by ion implantation of nitrogen into β-Ga_2O_3 epitaxial films to form current blocking layers has shown promising device performance. Due to the easy diffusion of Mg in the β-Ga_2O_3 epitaxial films, especially at a high annealing temperature, nitrogen is a promising candidate for the formation of semi-insulating layers compared to Mg. The in-situ doping capability of nitrogen into β-Ga_2O_3 epitaxial films has been demonstrated by MOCVD by utilizing nitrous oxygen N_2O[41], N_2 and NH_3 as the nitrogen dopant[48]. Compared to N_2O, which also serves as oxidizer during growth, NH_3/N_2 gas mixture is more flexible to use for controlling the nitrogen concentration since it is not limited by the growth pressure in the chamber of MOCVD.

The nitrogen doping profiles in a MOCVD-grown β-Ga_2O_3 epitaxial films doped by ammonia diluted in nitrogen (NH_3/N_2) gas measured by SIMS is shown in Figure 1.10. The spike in the beginning of the nitrogen doped layer is due to the unstable initial gas flow fluctuation of the NH_3/N_2 mixture gas in the mass flow controller (MFC). The nitrogen doping concentration showed almost the same level as that of the hydrogen doping concentration due to hydrogen incorporation, presumably from the decomposition of NH_3 gas precursor. The hydrogen incorporation also happened in the nitrogen doped β-Ga_2O_3 epitaxial films grown by N_2O gas precursor[41]. By increasing the molar flow rate of NH_3/N_2 gas mixture, the nitrogen concentration in the β-Ga_2O_3 epitaxial films were also increased

26

linearly from 1.2×10^{18} cm^{-3} to 2.0×10^{20} cm^{-3} with additional experiments done with higher NH$_3$/N$_2$ molar flow rate. This exhibited the controllable nitrogen doping in β-Ga$_2$O$_3$ epitaxial films by changing the NH$_3$/N$_2$ molar flow rate.
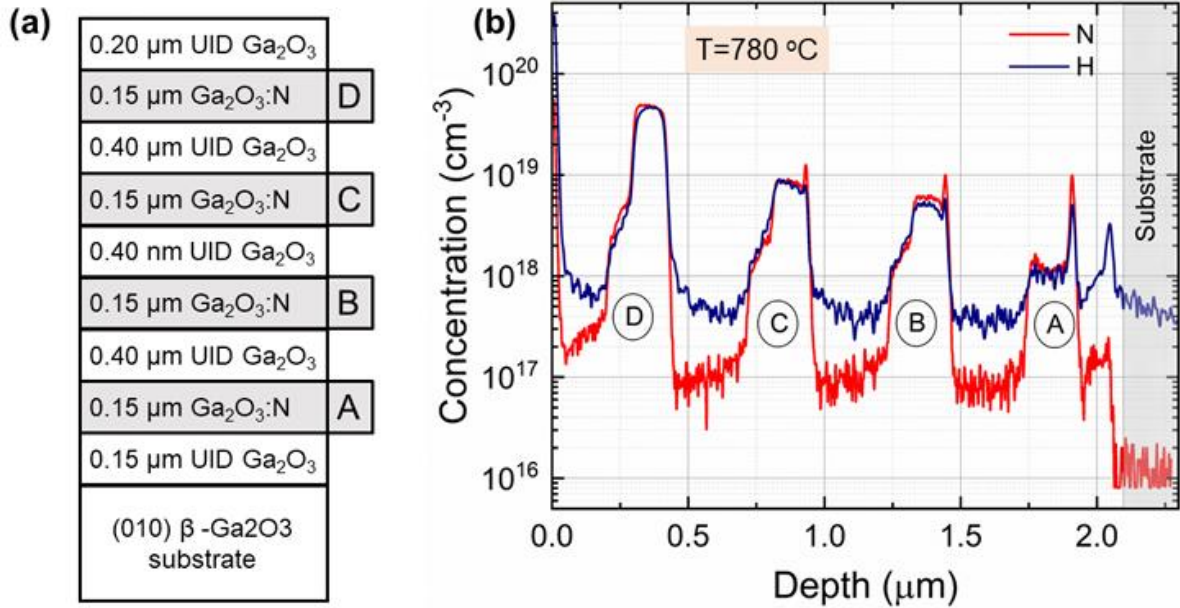
Figure 1.10. (a) SIMS-stack structure of a β-Ga$_2$O$_3$ epitaxial films grown by MOCVD with nitrogen doped layers by NH$_3$/N$_2$ and separated by UID layers at a substrate temperature of 780 °C. (b) SIMS profiles of nitrogen and hydrogen of this β-Ga$_2$O$_3$ epitaxial film with different NH$_3$/N$_2$ molar flow rates[48].

The crystal quality and surface morphologies of nitrogen doped β-Ga$_2$O$_3$ epitaxial films are shown in Figure 1.11. The crystal quality was evaluated by HRXRD out-of-plane diffraction (020) and in-plane diffraction (111). Among the samples with a nitrogen concentrations from 4.0×10^{18} cm^{-3} to 8.0×10^{18} cm^{-3}, the FWHM of the diffraction peaks of both the in-plane and out-of-plane peaks remained the values of 38 to 70 arcsec, which

indicates the crystal quality is still comparable to high-quality β-Ga$_2$O$_3$ epitaxial films[49] and bulk substrates[50] even with nitrogen and hydrogen incorporated in the 1.0×10^{18} cm^{-3} range. Additionally, the values of FWHM of the two nitrogen doped samples were approximately the same, which indicates that increased nitrogen concentration did not affect the crystal quality of β-Ga$_2$O$_3$ epitaxial films. The surface morphologies of nitrogen doped β-Ga$_2$O$_3$ epitaxial films were measured by AFM. Compared to the UID β-Ga$_2$O$_3$ epitaxial film, the nitrogen doped films showed clear groove features, which resulted in higher values of RMS roughness (~ 15 nm) due to the height difference between the top and the bottom of the grooves. These enlarged groove features might be attributed to the high-concentration hydrogen incorporating since similar large groove features were also observed on the surfaces of β-Ga$_2$O$_3$ epitaxial films grown by MOCVD using H$_2$O as oxygen source[51,52].

Though p-type conductivity is not possible in the β-Ga$_2$O$_3$ materials systems due to the extremely flat valence band[53] and the hole self-localization[54], acceptor doing by dopants such as Mg and nitrogen can form semi-insulating layers for the fabrication of vertical power electronic devices. Since Mg is easy to diffuse at a high temperature like >1000 ℃, nitrogen can be a promising candidate to form stable semi-insulating layers due to its low diffusion in β-Ga$_2$O$_3$ films. The formation of current blocking layer by acceptor doping can significantly enhance the performance of vertical devices such as current aperture MOSFETs and increase the flexibility of device designs.
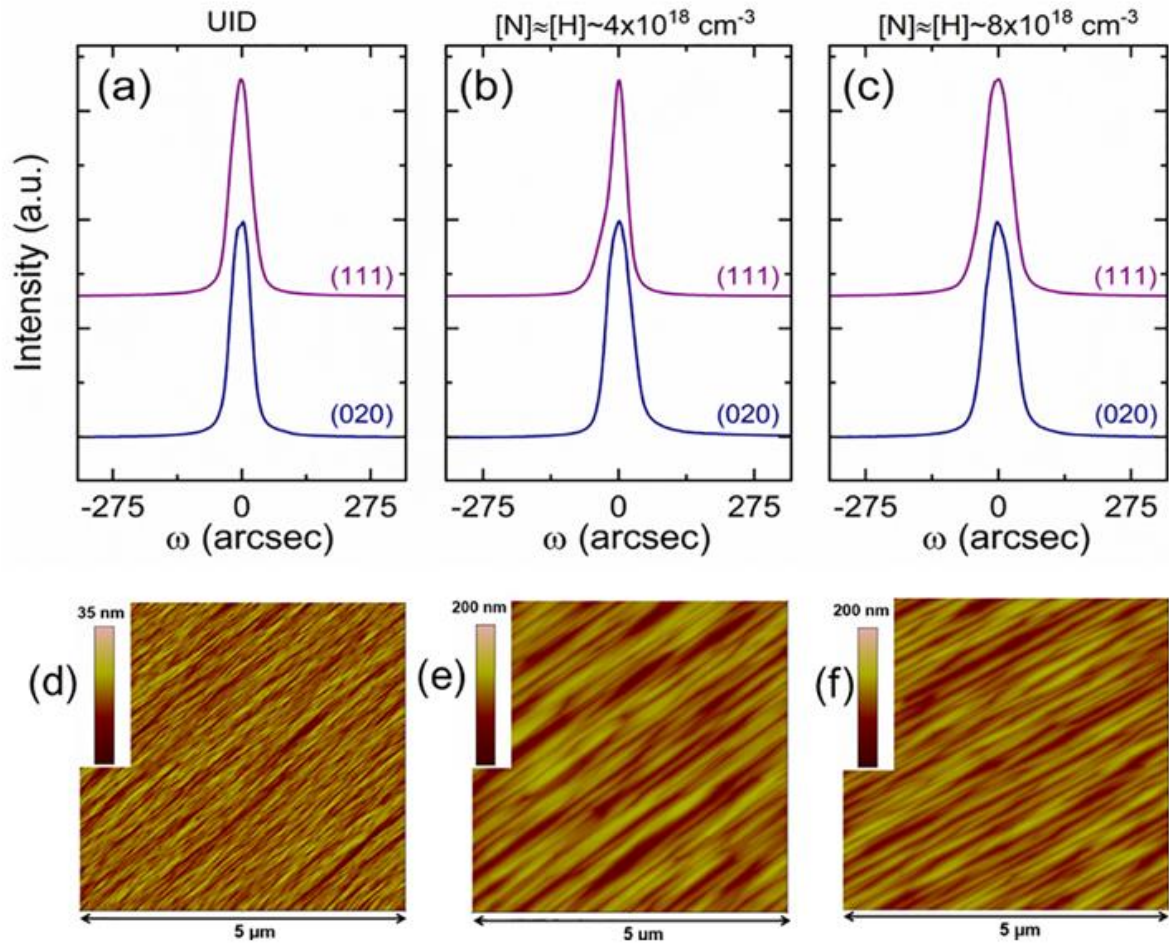
Figure 1.11. (a) The HRXRD diffraction patterns of β-Ga$_2$O$_3$ epitaxial films' in-plane (111) and out-of-plane (020) diffraction peaks at different nitrogen concentrations. (d) AFM images of nitrogen doped β-Ga$_2$O$_3$ epitaxial films exhibiting higher values of RMS roughness due to enhanced groove features[48].

1.10 Summary

β-Ga$_2$O$_3$ shows exceptional potential for the application of high-voltage, high-current power electronics. Its availability of high-quality single-crystal bulk substrates enables low-defect, high-purity epitaxial growth to achieve significantly lower background impurities compared to other semiconductor materials. Moreover, the availability of shallow donors such as Ge and Si provides wide range of n-type doping capabilities to achieve light doping in the drift region of power electronic devices. These properties ensure a large value of modified BFOM compared to other wide bandgap semiconductor materials. Epitaxial growth of β-Ga$_2$O$_3$ films and doped films by MOCVD, HVPE and MBE has shown remarkable crystal quality and electronic properties. However, the surface morphology of β-Ga$_2$O$_3$ epitaxial films shows grooved features due to surface faceting[55] on all the crystal orientations that have been studied so far. In Chapter 2, epitaxial growth on the energetic stable (110) plane is studied toward ultimate flat surface morphology. To achieve efficient and wide-range n-type doping in β-Ga$_2$O$_3$ films, Si is considered to be the most suitable donor due to its shallow donor level and near 100% ionization efficiency. Si-doping remains challenging in MBE growth due to the highly oxidation environment. In Chapter 3, a valved effusion cell is utilized to achieve continuous Si doping in β-Ga$_2$O$_3$ films on (010) and (001) orientations. The Si doping concentrations in the β-Ga$_2$O$_3$ films measured by SIMS exhibit continuous and flat profiles with sharp turn on/off, which indicates that controllable Si doping is achieved by utilizing the valved effusion cell. In Chapter 4, a pure ozone generator is utilized to provide high oxygen supply with low impurity levels for the epitaxial growth of β-Ga$_2$O$_3$ films. The ozone concentration was significantly improved by introducing a loop gas pipeline to the pure ozone generator.

References

1. S.J. Pearton, F. Ren, M. Tadjer, and J. Kim, "Perspective: Ga_2O_3 for ultra-high power rectifiers and MOSFETS," J. Appl. Phys. **124**(22), 220901 (2018).

2. G. Gupta, M. Kanamura, B. Swenson, C. Neufeld, T. Hosoda, P. Parikh, R. Lal, and U. Mishra, in *2022 International Electron Devices Meeting (IEDM)* (2022), p. 35.2.1-35.2.4.

3. M. Orita, H. Ohta, M. Hirano, and H. Hosono, "Deep-ultraviolet transparent Beta-Ga2O3 conductive thin films," Appl. Phys. Lett. **77**, 4166 (2000).

4. M. Higashiwaki, K. Sasaki, A. Kuramata, T. Masui, and S. Yamakoshi, "Gallium oxide (Ga 2O 3) metal-semiconductor field-effect transistors on single-crystal β-Ga 2O 3 (010) substrates," Appl. Phys. Lett. **100**(1), 013504 (2012).

5. B.J. Baliga, "Semiconductors for high-voltage, vertical channel field-effect transistors," J. Appl. Phys. **53**(3), 1759–1764 (1982).

6. Y. Zhang, and J.S. Speck, "Importance of shallow hydrogenic dopants and material purity of ultra-wide bandgap semiconductors for vertical power electron devices," Semicond. Sci. Technol. **35**(12), (2020).

7. A. Kuramata, K. Koshi, S. Watanabe, Y. Yamaoka, T. Masui, and S. Yamakoshi, "High-quality β-Ga 2 O 3 single crystals grown by edge-defined film-fed growth," Jpn. J. Appl. Phys. **55**, 1202A2 (2016).

8. Z. Galazka, "Growth of bulk β-Ga2O3 single crystals by the Czochralski method," J. Appl. Phys. **131**(3), (2022).

9. N. Suzuki, S. Ohira, M. Tanaka, T. Sugawara, K. Nakajima, and T. Shishido, "Fabrication and characterization of transparent conductive Sn-doped β-Ga 2 O 3 single crystal," Phys. Status Solidi C **4**(7), 2310–2313 (2007).

10. Y. Ueda, T. Igarashi, K. Koshi, S. Yamakoshi, K. Sasaki, and A. Kuramata, "Two-inch Fe-doped β-Ga2O3 (010) substrates prepared using vertical Bridgman method," Jpn. J. Appl. Phys. **62**(SF), SF1006 (2023).

11. Y. Zhang, F. Alema, A. Mauze, O.S. Koksaldi, R. Miller, A. Osinsky, and J.S. Speck, "MOCVD grown epitaxial β -Ga 2 O 3 thin film with an electron mobility of 176 cm 2 /V s at room temperature," APL Materials **7**(2), 022506 (2019).

12. F. Alema, Y. Zhang, A. Osinsky, N. Valente, A. Mauze, T. Itoh, and J.S. Speck, "Low temperature electron mobility exceeding 104 cm2/V s in MOCVD grown β -Ga2O3," APL Materials **7**(12), 121110 (2019).

13. H. Murakami, K. Nomura, K. Goto, K. Sasaki, K. Kawara, Q.T. Thieu, R. Togashi, Y. Kumagai, M. Higashiwaki, A. Kuramata, S. Yamakoshi, B. Monemar, and A. Koukitu, "Homoepitaxial growth of β-Ga 2 O 3 layers by halide vapor phase epitaxy," Applied Physics Express **8**(1), 015503 (2015).

14. J.H. Leach, K. Udwary, J. Rumsey, G. Dodson, H. Splawn, and K.R. Evans, "Halide vapor phase epitaxial growth of β -Ga 2 O 3 and α -Ga 2 O 3 films," APL Materials **7**(2), 022504 (2019).

15. K. Sasaki, A. Kuramata, T. Masui, E.G. Víllora, K. Shimamura, and S. Yamakoshi, "Device-quality β-Ga 2o 3epitaxial films fabricated by ozone molecular beam epitaxy," Appl. Phys. Express **5**(3), 035502 (2012).

16. H. Okumura, M. Kita, K. Sasaki, A. Kuramata, M. Higashiwaki, and J.S. Speck, "Systematic investigation of the growth rate of β-Ga2O3(010) by plasma-assisted molecular beam epitaxy," Applied Physics Express **7**(9), 095501 (2014).

17. A. Mauze, Y. Zhang, T. Itoh, F. Wu, and J.S. Speck, "Metal oxide catalyzed epitaxy (MOCATAXY) of β-Ga2O3 films in various orientations grown by plasma-assisted molecular beam epitaxy," APL Materials **8**(2), (2020).

18. Z. Feng, A.F.M.A.U. Bhuiyan, Z. Xia, W. Moore, Z. Chen, J.F. McGlone, D.R. Daughton, A.R. Arehart, S.A. Ringel, S. Rajan, and H. Zhao, "Probing Charge Transport and Background Doping in Metal-Organic Chemical Vapor Deposition-Grown (010) β-Ga2O3," Physica Status Solidi - Rapid Research Letters **14**(8), 1–6 (2020).

19. F. Alema, Y. Zhang, A. Osinsky, N. Orishchin, N. Valente, A. Mauze, and J.S. Speck, "Low 1 0 14 cm-3 free carrier concentration in epitaxial β-Ga2O3 grown by MOCVD," APL Materials **8**(2), 021110 (2020).

20. H. Nishinaka, T. Nagaoka, Y. Kajita, and M. Yoshimoto, "Rapid homoepitaxial growth of (010) β-Ga2O3 thin films via mist chemical vapor deposition," Mater. Sci. Semicond. Process. **128**, 105732 (2021).

21. S. Ilhom, A. Mohammad, D. Shukla, J. Grasso, B.G. Willis, A.K. Okyay, and N. Biyikli, "Low-Temperature As-Grown Crystalline β-Ga2O3 Films via Plasma-Enhanced Atomic Layer Deposition," ACS Appl. Mater. Interfaces **13**(7), 8538–8551 (2021).

22. R.K. Ramachandran, J. Dendooven, J. Botterman, S.P. Sree, D. Poelman, J.A. Martens, H. Poelman, and C. Detavernier, "Plasma enhanced atomic layer deposition of Ga2O3 thin films," J. Mater. Chem. A Mater. Energy Sustain. **2**(45), 19232–19238 (2014).

23. S. Khartsev, N. Nordell, M. Hammar, J. Purans, and A. Hallén, "High-quality Si-doped β-Ga 2 O 3 films on sapphire fabricated by pulsed laser deposition," Phys. Status Solidi B Basic Res. **258**(2), 2000362 (2021).

24. K.D. Leedy, K.D. Chabak, V. Vasilyev, D.C. Look, J.J. Boeckl, J.L. Brown, S.E. Tetlak, A.J. Green, N.A. Moser, A. Crespo, D.B. Thomson, R.C. Fitch, J.P. McCandless, and G.H. Jessen, "Highly conductive homoepitaxial Si-doped Ga2O3 films on (010) β-Ga2O3 by pulsed laser deposition," Appl. Phys. Lett. **111**(1), 012103 (2017).

25. B. Mazumder, J. Sarker, Y. Zhang, J.M. Johnson, M. Zhu, S. Rajan, and J. Hwang, "Atomic scale investigation of chemical heterogeneity in β-(AlxGa1-x)2O3 films using atom probe tomography," Appl. Phys. Lett. **115**(13), 132105 (2019).

26. A.F.M.A.U. Bhuiyan, Z. Feng, J.M. Johnson, H.L. Huang, J. Sarker, M. Zhu, M.R. Karim, B. Mazumder, J. Hwang, and H. Zhao, "Phase transformation in MOCVD growth of (AlxGa1-x)2O3 thin films," APL Materials **8**(3), 031104 (2020).

27. C. Kranert, M. Jenderka, J. Lenzner, M. Lorenz, H. von Wenckstern, R. Schmidt-Grund, and M. Grundmann, "Lattice parameters and Raman-active phonon modes of β-(AlxGa−x)2O3," J. Appl. Phys. **117**(12), 125703 (2015).

28. A.J. Green, J. Speck, G. Xing, P. Moens, F. Allerstam, K. Gumaelius, T. Neyer, A. Arias-Purdue, V. Mehrotra, A. Kuramata, K. Sasaki, S. Watanabe, K. Koshi, J. Blevins, O. Bierwagen, S. Krishnamoorthy, K. Leedy, A.R. Arehart, A.T. Neal, S. Mou, S.A. Ringel, A. Kumar, A. Sharma, K. Ghosh, U. Singisetti, W. Li, K. Chabak, K. Liddy, A. Islam, S. Rajan, S. Graham, S. Choi, Z. Cheng, and M. Higashiwaki, "β-Gallium oxide power electronics," APL Materials **10**(2), 029201 (2022).

29. Z. Guo, A. Verma, X. Wu, F. Sun, A. Hickman, T. Masui, A. Kuramata, M. Higashiwaki, D. Jena, and T. Luo, "Anisotropic thermal conductivity in single crystal β-gallium oxide," Appl. Phys. Lett. **106**(11), 111909 (2015).

30. F. Alema, T. Itoh, W. Brand, M. Tadjer, A. Osinsky, and J.S. Speck, "N2O grown high Al composition nitrogen doped β-(AlGa)2O3/β-Ga2O3 using MOCVD," J. Vac. Sci. Technol. A **41**(4), (2023).

31. P. Vogt, and O. Bierwagen, "Reaction kinetics and growth window for plasma-assisted molecular beam epitaxy of Ga2O3: Incorporation of Ga vs. Ga2O desorption," Appl. Phys. Lett. **108**(7), 072101 (2016).

32. Y. Oshima, E. Ahmadi, S. Kaun, F. Wu, and J.S. Speck, "Growth and etching characteristics of (001) β-Ga2O3 by plasma-assisted molecular beam epitaxy," Semicond. Sci. Technol. **33**(1), 015013 (2018).

33. A.T. Neal, S. Mou, S. Rafique, H. Zhao, E. Ahmadi, J.S. Speck, K.T. Stevens, J.D. Blevins, D.B. Thomson, N. Moser, K.D. Chabak, and G.H. Jessen, "Donors and deep acceptors in β-Ga2O3," Appl. Phys. Lett. **113**(6), 1–6 (2018).

34. J.B. Varley, J.R. Weber, A. Janotti, and C.G. Van de Walle, "Oxygen vacancies and donor impurities in β-Ga2O3," Appl. Phys. Lett. **97**(14), (2010).

35. E. Ahmadi, O.S. Koksaldi, S.W. Kaun, Y. Oshima, D.B. Short, U.K. Mishra, and J.S. Speck, "Ge doping of β-Ga2O3 films grown by plasma-assisted molecular beam epitaxy," Appl. Phys. Express **10**(4), 041102 (2017).

36. A. Mauze, Y. Zhang, T. Itoh, E. Ahmadi, and J.S. Speck, "Sn doping of (010) β-Ga2O3 films grown by plasma-assisted molecular beam epitaxy," Appl. Phys. Lett. **117**(22), 222102 (2020).

37. E. Ahmadi, O.S. Koksaldi, S.W. Kaun, Y. Oshima, D.B. Short, U.K. Mishra, and J.S. Speck, "Ge doping of β-Ga 2 O 3 films grown by plasma-assisted molecular beam epitaxy," Applied Physics Express **10**(4), 041102 (2017).

38. K.M. Adkison, S.-L. Shang, B.J. Bocklund, D. Klimm, D.G. Schlom, and Z.-K. Liu, "Suitability of binary oxides for molecular-beam epitaxy source materials: A comprehensive thermodynamic analysis," APL Materials **8**(8), 081110 (2020).

39. M.E. Ingebrigtsen, J.B. Varley, A.Y. Kuznetsov, B.G. Svensson, G. Alfieri, A. Mihaila, U. Badstübner, and L. Vines, "Iron and intrinsic deep level states in Ga2O3," Appl. Phys. Lett. **112**(4), 042104 (2018).

40. A. Mauze, Y. Zhang, T. Mates, and F. Wu, "Investigation of unintentional Fe incorporation in (010) β-Ga2O3 films grown by plasma-assisted molecular beam epitaxy," J. Phys. D Appl. Phys., (2019).

41. F. Alema, Y. Zhang, A. Osinsky, N. Orishchin, N. Valente, A. Mauze, and J.S. Speck, "Low 1014 cm−3 free carrier concentration in epitaxial β-Ga2O3 grown by MOCVD," APL Materials **8**(2), 021110 (2020).

42. M.H. Wong, K. Goto, H. Murakami, Y. Kumagai, and M. Higashiwaki, "Current Aperture Vertical β -Ga2O3 MOSFETs Fabricated by N- and Si-Ion Implantation Doping," IEEE Electron Device Lett. **40**(3), 431–434 (2019).

43. M.H. Wong, C.-H. Lin, A. Kuramata, S. Yamakoshi, H. Murakami, Y. Kumagai, and M. Higashiwaki, "Acceptor doping of β-Ga2O3 by Mg and N ion implantations," Appl. Phys. Lett. **113**(10), 102103 (2018).

44. Z. Feng, A. Bhuiyan, and N.K. Kalarickal, "Mg acceptor doping in MOCVD (010) β-Ga2O3," J. Phys. D Appl. Phys., (2020).

45. A. Mauze, Y. Zhang, T. Itoh, T.E. Mates, H. Peelaers, C.G. de Walle, and J.S. Speck, "Mg doping and diffusion in (010) beta-Ga2O3 films grown by plasma-assisted molecular beam epitaxy," J. Appl. Phys. **130**(23), (2021).

46. H. Peelaers, J.L. Lyons, J.B. Varley, and C.G. de Walle, "Deep acceptors and their diffusion in Ga2O3," APL MATERIALS **7**(2), (2019).

47. J.L. Lyons, "A survey of acceptor dopants for β-Ga2O3," Semicond. Sci. Technol. **33**(5), 05LT02 (2018).

48. F. Alema, T. Itoh, W. Brand, A. Osinsky, and J.S. Speck, "Controllable nitrogen doping of MOCVD Ga2O3 using NH3," Appl. Phys. Lett. **122**(25), (2023).

49. Y. Zhang, F. Alema, A. Mauze, O.S. Koksaldi, R. Miller, A. Osinsky, and J.S. Speck, "MOCVD grown epitaxial β-Ga2O3 thin film with an electron mobility of 176 cm2/V s at room temperature," APL Mater. **7**(2), 022506 (2019).

50. D. Gogova, M. Schmidbauer, and A. Kwasniewski, "Homo- and heteroepitaxial growth of Sn-doped β-Ga2O3 layers by MOVPE," CrystEngComm **17**(35), 6744–6752 (2015).

51. G. Wagner, M. Baldini, D. Gogova, M. Schmidbauer, R. Schewski, M. Albrecht, Z. Galazka, D. Klimm, and R. Fornari, "Homoepitaxial growth of β-Ga2O3layers by metal-organic vapor phase epitaxy," Phys. Status Solidi **211**(1), 27–33 (2014).

52. F. Alema, Y. Zhang, A. Mauze, T. Itoh, J.S. Speck, B. Hertog, and A. Osinsky, "H2O vapor assisted growth of beta-Ga2O3 by MOCVD," AIP Adv. **10**(8), (2020).

53. H. Peelaers, and C.G. Van de Walle, "Brillouin zone and band structure of β-Ga2O3," Physica Status Solidi (B) Basic Research **252**(4), 828–832 (2015).

54. S. Marcinkevičius, and J.S. Speck, "Ultrafast dynamics of hole self-localization in β-Ga2O3," Appl. Phys. Lett. **116**(13), 132101 (2020).

55. P. Mazzolini, P. Vogt, R. Schewski, C. Wouters, M. Albrecht, and O. Bierwagen, "Faceting and metal-exchange catalysis in (010) β-Ga 2 O 3 thin films homoepitaxially grown by plasma-assisted molecular beam epitaxy," APL Materials **7**(2), 022511 (2019).

II. Growth orientation of β-Ga$_2$O$_3$

2.1. Introduction

Epitaxial growth of β-Ga$_2$O$_3$ films with remarkable crystal quality has been achieved on various orientations of single-crystal substrates by metal organic chemical vapor deposition (MOCVD)[1,2], hydride vapor phase epitaxy (HVPE)[3,4] and molecular beam epitaxy (MBE)[5–7]. Recent reports have shown that MOCVD grown β-Ga$_2$O$_3$ films exhibited low temperature electron mobility of ~10^4 cm/Vs[2,8], while other research reported carrier concentration as low as ~2×10^{14} cm^{-3} [9]. Additionally, early lateral field effect transistors have been demonstrated on the (010) orientation[10,11]. However, there is still much improvement to be made in materials' quality and electronic properties. Achieving an extremely smooth surface morphology of β-Ga$_2$O$_3$ films is essential to minimize interface scattering in the channels of such lateral devices and is particularly important for MODFETs that utilized the β-(Al$_x$Ga$_{1-x}$)$_2$O$_3$/β-Ga$_2$O$_3$ heterostructure[12,13]. Therefore, to further improve the electronic properties of β-Ga$_2$O$_3$-based devices to overcome the obstacles for the next-generation power electronics, it is our goal to achieve atomically flat surface by selecting optimal crystal orientation system including bulk growth, epitaxial growth and device fabrication. Sasaki *et al* showed that (010) plane has the highest growth rate among the many low index crystal planes of β-Ga$_2$O$_3$, which indicates that (010) is the preferred growth plane for β-Ga$_2$O$_3$[15]. However, the surface morphology of β-Ga$_2$O$_3$ epitaxial films has room for improvement due to absence of a clear step/terrace structures which results in no step-flow growth. Moreover, Mazzolini *et al* has observed chevrons in reflection high-energy electron diffraction (RHEED) patterns during growth which were due to the formation of (110) and (-110) facets (the (110) and (010) surface structures are shown schematically in Fig. 2.1

which are constructed based on surface charge neutrality[14]. On the other hand, the presence of chevrons indicates that the (110) orientation is an energetically stable surface and suitable for epitaxial growth of β-Ga₂O₃ by MBE[15]. Because of this, it could be an interesting plane for achieving atomically flat film morphologies in epitaxial growth. In this study, we explored β-Ga₂O₃ film growth on (110) substrates via plasma-assisted MBE (PAMBE) to investigate its crystal quality, surface morphology, and growth characteristics.
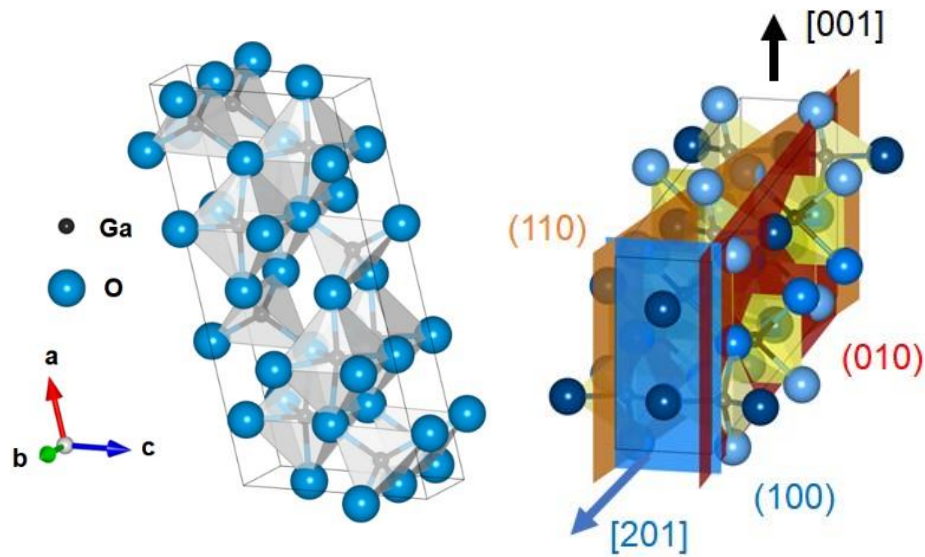
Figure 2.1. The crystal structure of β-Ga₂O₃ and the allocation of (110) plane in the unit cell with respect to other low-index planes and orientations.

The geometry and low-index planes with the relationship with the (110) plane are shown in Figure 2.1. The atomic structures were produced by VESTA software using ionic radius models. On the left, the unit cell with Ga atoms and oxygen atoms of β-Ga₂O₃ is shown. Since β-Ga₂O₃ has a crystal structure of monoclinic, the lengths of the three axes are not the same. Moreover, the unique β angle is not equal to 90 degrees, but 103.87 degrees. The

titled unit cell makes the orientation indices different from the normal cubic crystal system. The direction perpendicular to the (100) plane is not the [100] direction, but it is the [201] direction. Therefore, as shown in the right of Fig. 2.1, the substrate geometry that the vertical direction of (110) substrate is [201], and its horizontal direction is [001].

β-Ga_2O_3 epitaxial films were grown by PAMBE on Sn-doped ([Sn] = ~5×10^{18} cm^{-3}) (110) substrates grown by Novel Crystal Technology using the EFG method. The surfaces of the substrates were finished by chemical-mechanical polishing (CMP) process. Additionally, (010) substrates were co-loaded with the (110) substrates for MBE growth to use as references with identical growth conditions. Standard cleaning procedure using acetone and isopropyl alcohol (IPA) along with a 4 hour bake at 220 °C in the intro chamber was conducted before introducing the samples into the MBE chamber. The growth temperature was measured with a thermocouple and the metal fluxes were measured with a nude ion gauge as a beam equivalent pressure (BEP). The Ga flux for growth was varied from 3.0×10^{-8} Torr to 3.0×10^{-7} Torr to optimize the growth condition of epitaxial films on (110) substrates. Prior to the growth, 30 min oxygen polishing and 10 min Ga polishing were performed to clean off the impurities on the surface of the substrates similar to Ahmadi *et al*[7,16]. The oxygen plasma power was 200 W and the pressure in the chamber during the growth was around 2.0×10^{-5} Torr. The β-Ga_2O_3 epitaxial film was grown on a thin (5-10 nm) β-$(Al_xGa_{1-x})_2O_3$ layer to spatially separate it from the substrate and allow for film thickness determination via high resolution X-ray diffraction (HRXRD). RHEED was used to monitor the structure of the substrate and epitaxial film surface before and during growth. The surface morphology of the epitaxial films was characterized by atomic force microscopy (AFM).
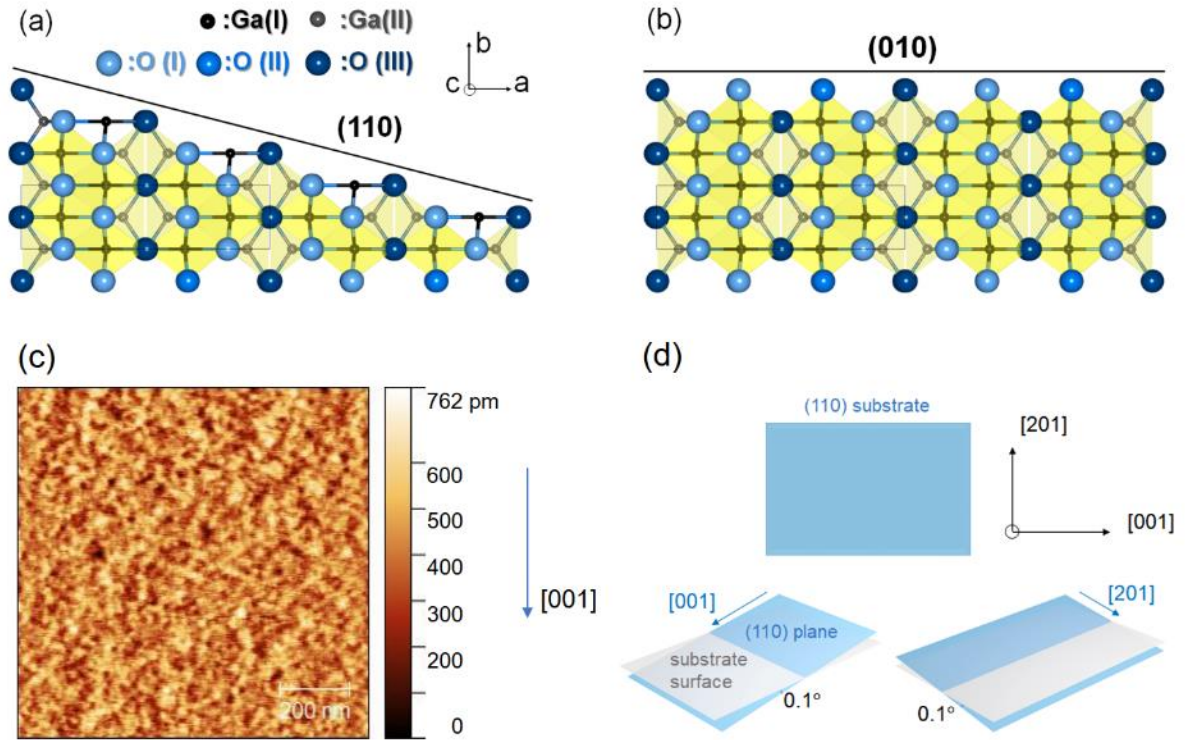
Figure 2.2. Atomic models of (a) (110) plane (b) (010) plane projected from [001] orientation. The rectangular gray lines represent unit cell of β-Ga₂O₃. (c) The AFM image for a scan area of 1×1 μm² shows a very low root mean squared (RMS) roughness of 0.08 nm for the surface of the as-received (110) Sn-doped substrate. (d) The geometry of (110) substrate and the miscut angles toward [001] and [201] directions. The miscut angles toward [001] direction and [201] directions are 0.1°.

2.2 Basics of (110) substrates

The surface morphology and crystal-quality of as-received Sn-doped (110) substrates were characterized by AFM and HRXRD. Figure 2.2 (c) shows the detailed AFM image of an as-received Sn-doped (110) substrate in 1 μm × 1 μm range. This AFM scan shows a very low root mean squared (RMS) roughness of 0.08 nm for this surface. Additionally, no step

or terrace structures but slightly elongated features along [001] direction can be confirmed from the surface. The miscut from the substrate surface was measured by HRXRD. Figure 2.2 (d) shows the schematic of (110) substrate and the orientation of miscut. The result of miscut measurement shows that the miscut angle along [001] direction and [201] direction is 0.1°, respectively. This indicates that the orientation of miscut is between [001] direction and [201] direction, while miscut orientation along [001] direction has the potential to exhibit step terrace structure.
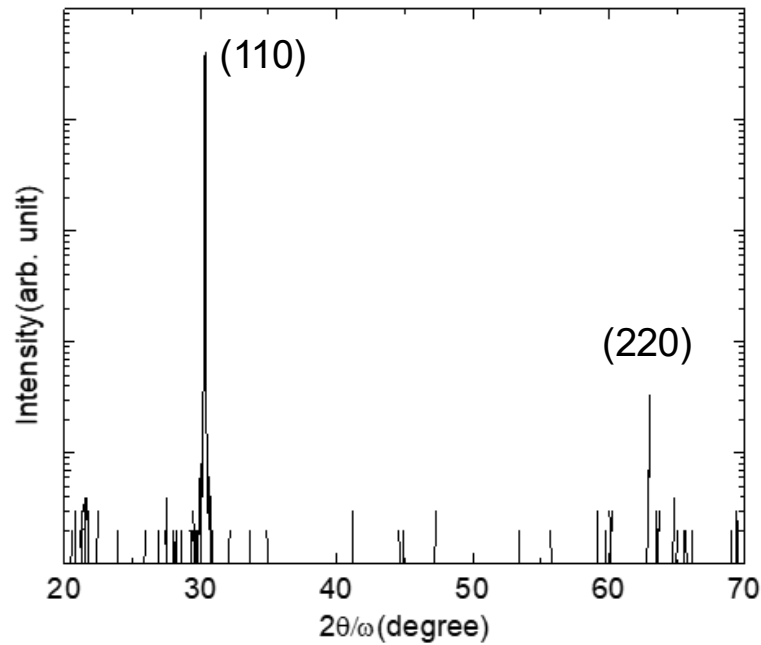

Figure 2.3. The wide angular range HRXRD diffraction patterns of an as-received β-Ga$_2$O$_3$ (110) substrate.

To further investigate the properties of the as-received 110 substrates, wide angular range high-resolution XRD measurement was performed. In figure 2.3, the wide angular range HRXRD results only show (110) peak and a (220) peak from this (110) substrate,

which shows that the 110 substrate is a single crystal and has a very high crystal quality. The high intensity of X-ray counts also indicates its outstanding crystal quality.

The RHEED patterns of the (110) and (010) substrates after 10 min Ga polishing are shown in Fig. 2.4. The chevron shape in (010) substrate reveals that the existence of the crystallographically equivalent (110) and (-110) facets when the substrate is oriented along the [001] azimuth, which was previously shown by Mazzolini *et al.*[15] The angle between the two oblique streak lines corresponds to the angle between (110) and (-110) planes, which is 28°. On the other hand, no chevrons were observed in the RHEED patterns for (110) growth for all incident RHEED beam directions. This suggests that no consistent faceting was formed on the surface of (110) substrates after Ga polishing.
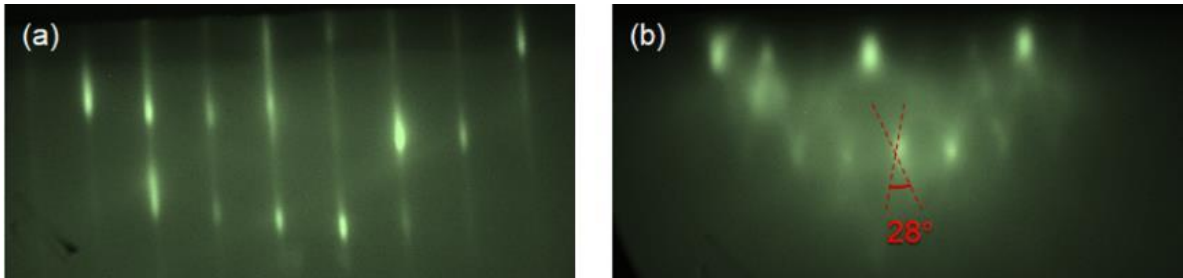
Figure 2.4. RHEED pattern of (a) (110) substrates and (b) (010) substrates after 10 min Ga polishing. Clear streaky patterns were observed from (110) substrates while (010) substrates from the [001] azimuth show chevron patterns indicative of faceting. The red crossed lines are guidelines which correspond to (110) and equivalent (-110) facets when the RHEED is taken along [001] azimuth. The angle between the two obliques is 28°, which is the angle between (110) plane and (-110) plane.

2.3 Growth of β-Ga₂O₃ on (110) substrates

To further investigate the crystal quality of β-Ga$_2$O$_3$ epitaxial films grown on (110) substrates, HRXRD of the samples was measured as shown in Fig. 2.5. The thickness fringes in HRXRD are characteristic of a smooth, abrupt interface between the β-Ga$_2$O$_3$ epitaxial film and β-(Al$_x$Ga$_{1-x}$)$_2$O$_3$ spacer layer, and consistent thickness. In addition, a HRXRD rocking curve measurement on a β-Ga$_2$O$_3$ epitaxial film on a (110) substrate is shown in Fig 2.5 (b). The full width at half maximum (FWHM) of the (110) peak is ~ 41 arcsec, which is comparable to the FWHM values reported for epitaxial films grown on (010) substrates[1] and bulk substrates[17].
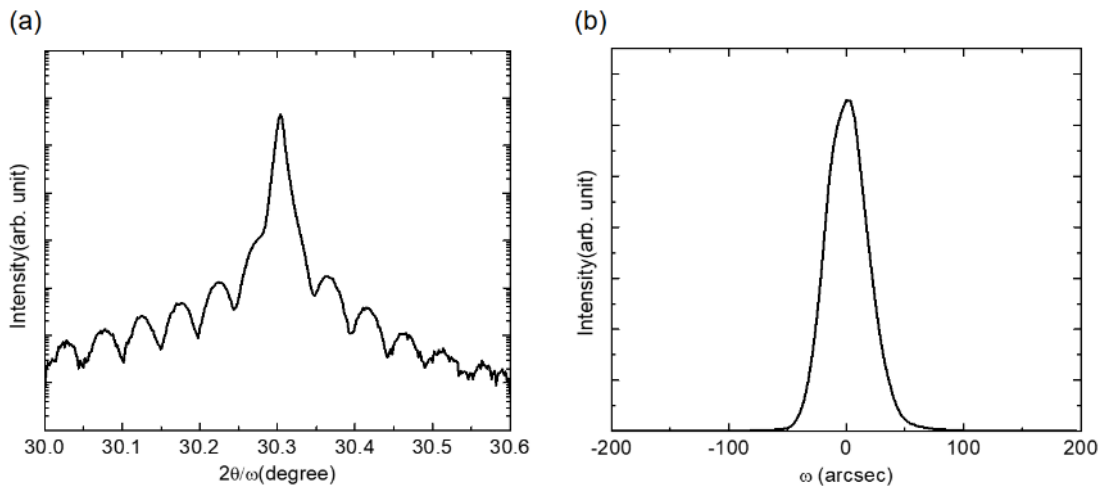
Figure 2.5. (a) HRXRD 2θ-ω scan of a 180-nm-thick β-Ga$_2$O$_3$ film on β-(Al$_x$Ga$_{1-x}$)$_2$O$_3$ spacer. Clear thickness fringes can be observed throughout a wide-angle range. (b) HRXRD rocking curve scan of a (110) β-Ga$_2$O$_3$ peak with a FWHM value of ~ 41 arcsec[18].

The dependence of the growth rate on Ga flux was also investigated as shown in Fig. 2.6, demonstrating two clear growth regimes. The O-rich regime is where the growth rates increase linearly with Ga flux. At higher Ga fluxes, growth transitions to the plateau regime

where growth rate remains constant. This maximum growth rate achieved in the plateau regime is also dependent on growth temperature as higher Ga suboxide desorption limits growth rate at higher temperatures[19–23]. This also shifts the Ga flux at which the transition to plateau regime occurs. At a substrate temperature of 600 °C, this transition is around Ga flux of 2.0×10^{-7} Torr and the maximum growth rate for (110) is 3.5 nm/min, while at 700 °C the transition is around Ga flux of 1.5×10^{-7} Torr and the maximum growth rate for (110) is 2.5 nm/min as seen in Fig. 2.6 (a). The growth rates are slightly decreasing as the Ga flux increases at a growth temperature of 700 °C, presumably due to higher Ga suboxide desorption at higher Ga flux. This trend is nearly the same between β-Ga_2O_3 epitaxial films grown on (110) and (010) substrates.
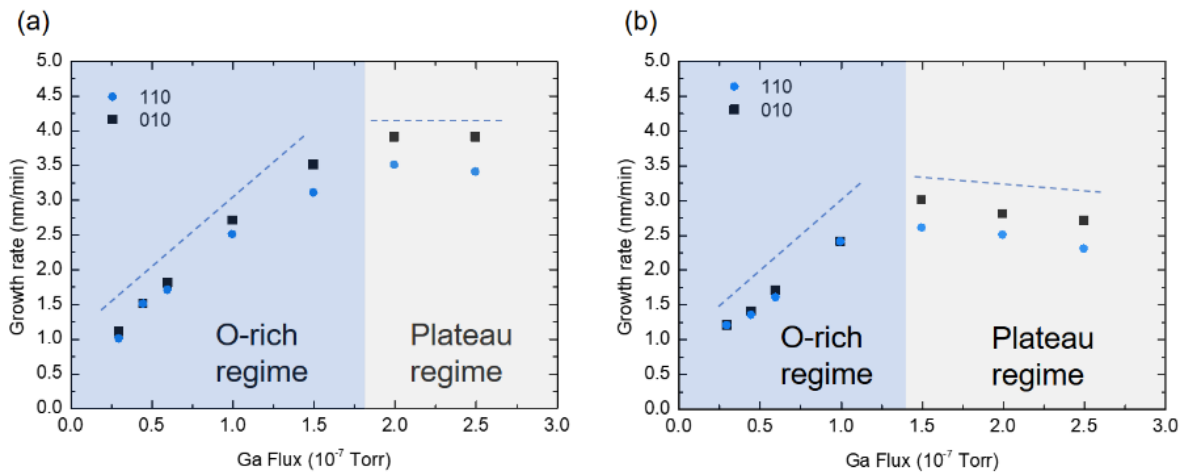

Figure 2.6. (a) Growth rates of β-Ga_2O_3 epitaxial films grown on (110) and (010) substrates at 600 °C and (b) 700 °C. In the O-rich regime the growth rate increases linearly as Ga flux increases. The stoichiometric point of Ga flux decreases as the growth temperature increases, which indicates enhanced suboxide desorption at higher growth temperature[18].

43

The growth rates of β-Ga$_2$O$_3$ epitaxial films grown on (110) and (010) substrates are approximately the same in the O-rich regime. However, in the plateau regime, the growth rates of (110) are ~10% lower than (010). Since the (110) facets are exposed in (010) growth, crystal plane through which Ga and O is incorporated is the (110) plane for both orientations of growth. However, because of the geometry of the inclined (110) facets in (010) growth, the exposed (110) surface area is ~10% more than that of (110) growth. This could suggest that the maximum growth rate is tied to the exposed (110) area. On the other hand, the difference of growth rates on (010) and (110) might be attributed to the etching rates by Ga flux at the plateau regime. The reduced growth rate of β-Ga$_2$O$_3$ epitaxial films grown on (110) substrates compared to that of (010) substrates might be explained by a higher Ga etching rate at the same Ga flux. The difference of etching rates can be investigated by using higher Ga flux during the growth than the current experiment range such as 3.0×10^{-7} Torr, 3.5×10^{-7} Torr. The difference in the Ga etching rates can also be revealed by the differences in the growth temperatures of β-Ga$_2$O$_3$ epitaxial films. The growth rates of β-Ga$_2$O$_3$ epitaxial films are approximately 30% higher at a substrate temperature of 600 ℃ than those of 700 ℃, which indicates that the Ga etching rates also strongly depends on the growth temperatures. Additionally, the decreasing growth rates on the (010) substrates at 700 ℃ also indicate that the Ga etching is enhanced at the higher growth temperatures.
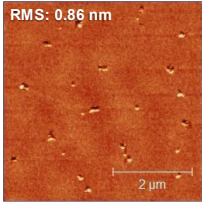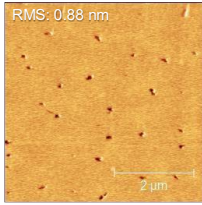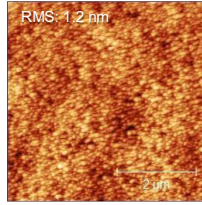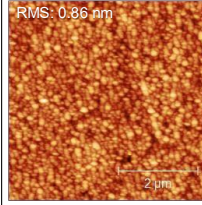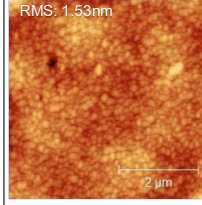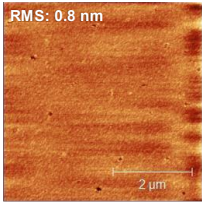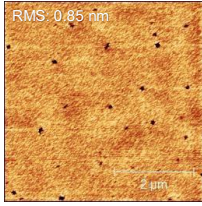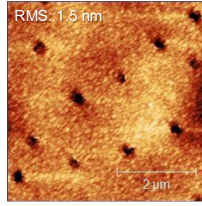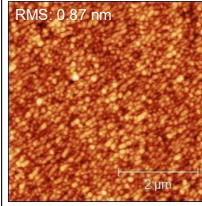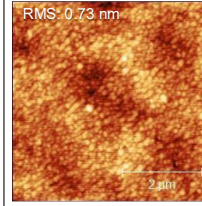
Ga flux	0.3×10^{-7} Torr	0.6×10^{-7} Torr	1.5×10^{-7} Torr	2.0×10^{-7} Torr	2.5×10^{-7} Torr
Growth on **(110)** sub.	RMS: 0.86 nm	RMS: 0.88 nm	RMS: 1.2 nm	RMS: 0.86 nm	RMS: 1.53 nm
Growth on **(010)** sub.	RMS: 0.8 nm	RMS: 0.85 nm	RMS: 1.5 nm	RMS: 0.87 nm	RMS: 0.73 nm

Figure 2.7. AFM images of β-Ga$_2$O$_3$ epitaxial films grown on (110) and (010) substrates at different Ga fluxes at 600 ℃ are measured for a scan area of 5×5 μm^2. Elongated features along [001] direction can be observed on both β-Ga$_2$O$_3$ epitaxial films grown on (110) and (010) substrates.

The surface morphologies of (110) and (010) films grown at different Ga fluxes at a substrate temperature of 600 ℃ measured by AFM are shown in Fig. 2.7. At Ga fluxes from 3.0×10^{-8} Torr to approximately 2.0×10^{-7} Torr, in the linear regime (O-rich regime), there are pits in different sizes on the surface of both β-Ga$_2$O$_3$ epitaxial films grown on (110) and (010) substrates. At higher Ga flux in the plateau regime, however, smoother surfaces without pits are achieved and the crystal size of β-Ga$_2$O$_3$ becomes larger as the Ga flux increases. The surface morphologies of β-Ga$_2$O$_3$ epitaxial films are smooth on both (110) and (010) substrates with RMS roughness less than 1.0 nm. Moreover, elongated features along the [001] direction were observed on the surface of β-Ga$_2$O$_3$ epitaxial films grown on (110) and (010) substrates.

Ga flux	6.0×10^{-8} Torr	1.0×10^{-7} Torr	1.5×10^{-7} Torr	2.0×10^{-7} Torr	2.5×10^{-7} Torr
Growth on **(110)** sub. [001]	17.8 nm · 0.0 nm · RMS: 2.0 nm	20.3 nm · 0.0 nm · RMS: 2.2 nm	5.6 nm · 0.0 nm · RMS: 0.7 nm	5.7 nm · 0.0 nm · RMS: 0.8 nm	3.2 nm · 0.0 nm · RMS: 0.4 nm
Growth on **(010)** sub. [001]	16.9 nm · 0.0 nm · RMS: 1.8 nm	15.2 nm · 0.0 nm · RMS: 1.8 nm	9.3 nm · 0.0 nm · RMS: 1.2 nm	10.3 nm · 0.0 nm · RMS: 1.2 nm	6.0 nm · 0.0 nm · RMS: 0.9 nm
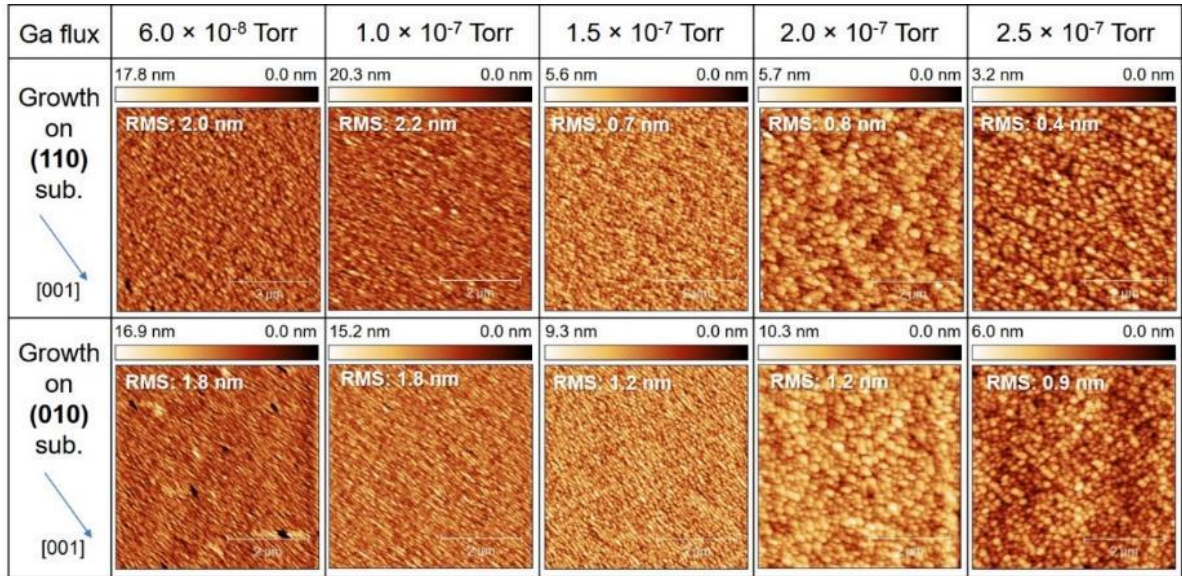
Figure 2.8. AFM images of β-Ga$_2$O$_3$ epitaxial films grown on (110) and (010) substrates at different Ga fluxes at 700 °C are measured for a scan area of 5×5 μm^2. Elongated features along [001] direction can be observed on both β-Ga$_2$O$_3$ epitaxial films grown on (110) and (010) substrates[18].

The surface morphologies of (110) and (010) films grown at different Ga fluxes at a substrate temperature of 700 °C measured by AFM are shown in Fig. 2.8. The β-Ga$_2$O$_3$ epitaxial films exhibited similar surface morphologies with close values of RMS roughness. Pits were observed on the surface of β-Ga$_2$O$_3$ epitaxial films with a Ga flux in the O-rich regime due to the lack of Ga supply during the epitaxial growth. Moreover, the surface morphologies of β-Ga$_2$O$_3$ epitaxial films showed slightly larger values of RMS roughness in the O-rich regime than that of the films grown at a substrate temperature of 600 °C. This result corresponds to the previous study on the surface roughness dependence on the substrate temperature of β-Ga$_2$O$_3$ epitaxial films grown by PAMBE. As the Ga flux

increases in the plateau regime, the value of RMS roughness decreases to form smoother surfaces with larger crystal sizes.

Additionally, elongated features oriented along the [001] direction are exhibited in the plateau regime on both (110) and (010) substrates grown at 600 °C and 700 °C, while this feature is not expected on the β-Ga$_2$O$_3$ epitaxial films grown on the (110) substrates due to the absence of clear faceting. Despite the appearance of (110) facets in growth of (010) β-Ga$_2$O$_3$, the (110) plane does not have tendency to show a well-defined step-terrace structure. This may be attributed to the absence of step features on the as-received (110) substrates potentially due to negligible miscut.

For the improvement of the performance of electronic devices based on β-Ga$_2$O$_3$, the epitaxial growth of high-quality β-(Al$_x$Ga$_{1-x}$)$_2$O$_3$ with high Al composition is the key to realize high channel mobility and current density. One of the challenges for the epitaxial growth of β-(Al$_x$Ga$_{1-x}$)$_2$O$_3$ is the limitation of Al composition. Since the thermally stable crystal structure for Ga$_2$O$_3$ and Al$_2$O$_3$ is different, β-Ga$_2$O$_3$ with monoclinic unit cell (space group C2/m) and α-Al$_2$O$_3$ with corundum unit cell (space group: R-3c), the solubility of Al$_2$O$_3$ into β-Ga$_2$O$_3$ is expected to be limited. This phase diagram predicts the limitation of Al composition in β-(Al$_x$Ga$_{1-x}$)$_2$O$_3$ to be ~67%. However, the highest Al composition has been achieved by MBE on (010) substrate is around 23%. Higher Al fluxes during the MBE growth of β-(Al$_x$Ga$_{1-x}$)$_2$O$_3$ epitaxial film at conventional growth temperature (~700°C) results in phase separation. On the other hand, MOCVD grown β-(Al$_x$Ga$_{1-x}$)$_2$O$_3$ epitaxial film on other substrate orientations such as (100) and ($\bar{2}$01) has recently been expanded up to ~50%[25]. However, the crystal quality and surface morphology still have much room to be

47

improved before this high Al composition β-$(Al_xGa_{1-x})_2O_3$ can be used as the channel materials of β-$(Al_xGa_{1-x})_2O_3/\beta$-$Ga_2O_3$ heterojunction electronic devices.

Investigations of β-$(Al_xGa_{1-x})_2O_3$ films on (110) substrate has been conducted by PAMBE. (010) substrates were co-loaded on the same Si supporting wafer to use as references with identical growth conditions in the MBE system. The crystal quality and Al composition of β-$(Al_xGa_{1-x})_2O_3$ films on (110) substrate was investigated by HRXRD. A 50-nm-thick β-$(Al_xGa_{1-x})_2O_3$ epitaxial film was grown on (110) substrate. Figure 2.9 (a) shows the HRXRD result which indicates a β-$(Al_xGa_{1-x})_2O_3$ peak is separated from the β-Ga_2O_3 (110) peak. Moreover, the surface morphology of β-$(Al_xGa_{1-x})_2O_3$ epitaxial films grown on (110) substrates measured by AFM scan shows smooth surface. The features on the surface of β-$(Al_xGa_{1-x})_2O_3$ epitaxial films are similar to that on (010) substrates. Thickness fringes in the HRXRD patterns can be observed but the intensity of the fringes was not large enough to be shown clearly on the diffraction pattern. It should be noted that the structure factor of (110) plane is about 1/6 of that of the (020) plane ((110): 28.08, (020):178.83). While clear thickness fringes were confirmed from β-$(Al_xGa_{1-x})_2O_3$ epitaxial film on (010) substrate, the thickness fringes were not clear from β-$(Al_xGa_{1-x})_2O_3$ epitaxial film (110) substrate, which is presumably due to the much lower structure factor than (010) orientation. However, the Al composition is still not determined from these results because the strain parameters of (110) β-$(Al_xGa_{1-x})_2O_3$ film has not been investigated yet. To identify the Al composition, X-ray photoelectron spectroscopy (XPS), energy-dispersive X-ray spectroscopy (EDX), atom probe tomography (ATP) can be used throughout the depth profile of β-$(Al_xGa_{1-x})_2O_3$ film. Future work of β-$(Al_xGa_{1-x})_2O_3$ growth on (110) substrates is to vary the growth temperature

and Ga flux to investigate their dependence on Al composition by HRXRD and ATP in order to enable the derivation of Al composition from HRXRD results.
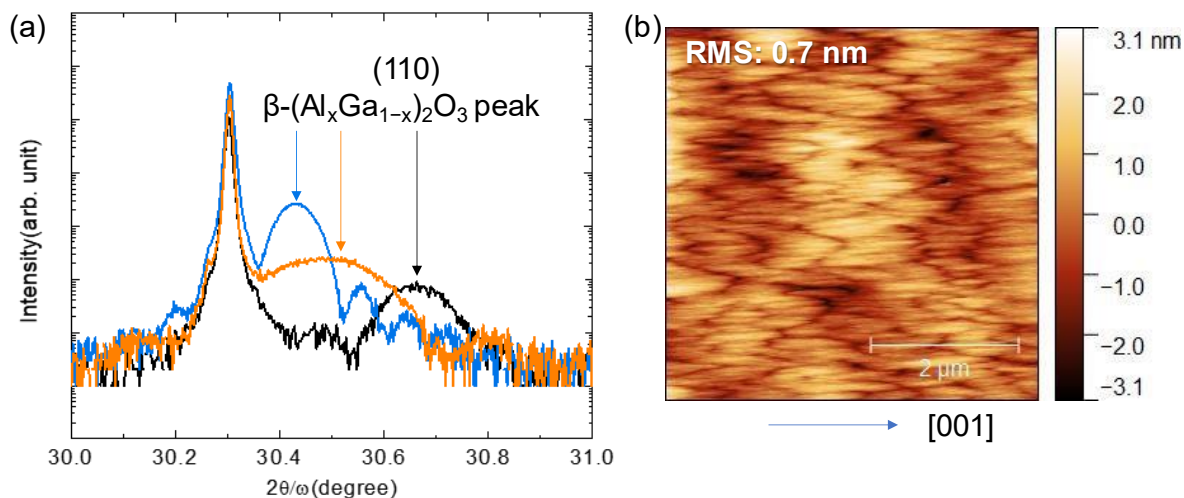
Figure 2.9. (a) HRXRD patterns of β-(Al$_x$Ga$_{1-x}$)$_2$O$_3$ films grown on (110) substrates with different Al compositions and (b) a 5 μm × 5 μm AFM scan of the surface morphology of β-(Al$_x$Ga$_{1-x}$)$_2$O$_3$ epitaxial film.

2.4 MOCATAXY growth on (110) substrates

To further explore the potential of epitaxial growth on (110) substrates, MOCATAX growth was introduced. Previously, this growth method showed that a supplied In flux during growth can significantly improve the growth rate of β-Ga$_2$O$_3$ on various orientations[7,26]. This enhancement of growth rate of β-Ga$_2$O$_3$ by MOCATAXY has been demonstrated to be due to a catalytic mechanism where In accesses more oxygen in the MBE growth environment, presumably both molecular O$_2$ and atomic O, rather than just the atomic O that acts as the active oxygen flux for conventional PAMBE growth. A metal-exchange mechanism between In and Ga then allows Ga to preferentially incorporate over In

49

in the β-Ga_2O_3 crystal structure, allowing for growth of pure β-Ga_2O_3 at sufficiently high Ga fluxes[27]. The presence of In also suppresses Ga_2O suboxide desorption, allowing for higher temperature growth. The substrate temperature for MOCATAXY growth was varied from 600 ℃ to 900 ℃. While there were no thickness fringes in HRXRD for growth at the substrate temperature 600 ℃ suggesting poor growth quality, thickness fringes in HRXRD were observed for growth temperatures of 700 ℃ - 900 ℃ suggesting high crystal-quality films for a similar temperature range as (010). The HRXRD pattern of 200-nm-thick β-Ga_2O_3 epitaxial films on (110) substrate is shown in Fig. 2.8 (a). Within this temperature range, the maximum growth rate of 4.5 nm/min was achieved for epitaxial growth on (110) substrate, which is ~10% lower than the growth rate of 5.0 nm/min on (010) substrate. This difference of growth rate between (110) and (010) was also observed while using non-MOCATAXY (conventional) growth. Furthermore, the growth temperature is increased to as high as 900 ℃ for (110) substrate while there is no growth above 800 ℃ via conventional growth. The AFM image of β-Ga_2O_3 epitaxial film grown on (110) substrate via MOCATAXY is shown in Fig. 2.10 (b). The surface morphology is also improved by utilizing MOCATAXY as elongated surface features (elongated in the [001] direction) were observed and the value of RMS roughness is as low as 0.4 nm.
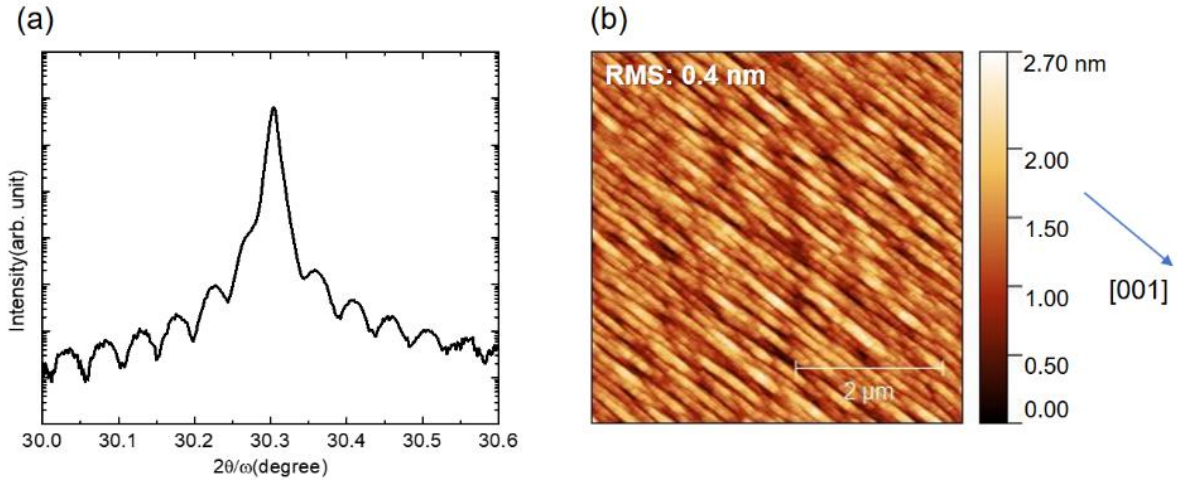
Figure 2.10. (a) HRXRD 2θ-ω scan of a 200-nm-thick MOCATAXY grown β-Ga$_2$O$_3$ epitaxial films on (110) substrate. (b) AFM image of MOCATAXY grown β-Ga$_2$O$_3$ epitaxial films on (110) substrate which shows extremely smooth surface morphology with an RMS roughness as low as 0.4 nm.

In summary, epitaxial growth of β-Ga$_2$O$_3$ films with high crystal quality and smooth surface morphology on (110) substrates were successfully performed via PAMBE at different substrate temperatures and Ga fluxes. While (110) facets were confirmed on (010) substrates that results in elongated features on the surface of the samples, similar features were also confirmed on (110) substrates. The absence of step features on as-received (110) substrates with minimal miscut may result in the lack of a well-defined step-terrace surface morphology for epitaxial films. Additionally, MOCATAXY growth enables epitaxial growth on (110) substrates to achieve higher growth rate up to 4.5 nm/min, growth temperatures up to 900 °C and smoother surface morphology. Future investigation into surface treatment such as wet etching prior to growth and application of an optimal miscut angle may further contribute to smooth film morphologies.

51

References

1. Y. Zhang, F. Alema, A. Mauze, O.S. Koksaldi, R. Miller, A. Osinsky, and J.S. Speck, "MOCVD grown epitaxial β -Ga 2 O 3 thin film with an electron mobility of 176 cm 2 /V s at room temperature," APL Materials **7**(2), 022506 (2019).

2. F. Alema, Y. Zhang, A. Osinsky, N. Valente, A. Mauze, T. Itoh, and J.S. Speck, "Low temperature electron mobility exceeding 104 cm2/V s in MOCVD grown β -Ga2O3," APL Materials **7**(12), 121110 (2019).

3. H. Murakami, K. Nomura, K. Goto, K. Sasaki, K. Kawara, Q.T. Thieu, R. Togashi, Y. Kumagai, M. Higashiwaki, A. Kuramata, S. Yamakoshi, B. Monemar, and A. Koukitu, "Homoepitaxial growth of β-Ga 2 O 3 layers by halide vapor phase epitaxy," Applied Physics Express **8**(1), 015503 (2015).

4. J.H. Leach, K. Udwary, J. Rumsey, G. Dodson, H. Splawn, and K.R. Evans, "Halide vapor phase epitaxial growth of β -Ga 2 O 3 and α -Ga 2 O 3 films," APL Materials **7**(2), 022504 (2019).

5. K. Sasaki, A. Kuramata, T. Masui, E.G. Víllora, K. Shimamura, and S. Yamakoshi, "Device-quality β-Ga 2o 3epitaxial films fabricated by ozone molecular beam epitaxy," Appl. Phys. Express **5**(3), 035502 (2012).

6. H. Okumura, M. Kita, K. Sasaki, A. Kuramata, M. Higashiwaki, and J.S. Speck, "Systematic investigation of the growth rate of β-Ga2O3(010) by plasma-assisted molecular beam epitaxy," Applied Physics Express **7**(9), 095501 (2014).

7. A. Mauze, Y. Zhang, T. Itoh, F. Wu, and J.S. Speck, "Metal oxide catalyzed epitaxy (MOCATAXY) of β -Ga2O3 films in various orientations grown by plasma-assisted molecular beam epitaxy," APL Materials **8**(2), (2020).

8. Z. Feng, A.F.M.A.U. Bhuiyan, Z. Xia, W. Moore, Z. Chen, J.F. McGlone, D.R. Daughton, A.R. Arehart, S.A. Ringel, S. Rajan, and H. Zhao, "Probing Charge Transport and Background Doping in Metal-Organic Chemical Vapor Deposition-Grown (010) β-Ga2O3," Physica Status Solidi - Rapid Research Letters **14**(8), 1–6 (2020).

9. F. Alema, Y. Zhang, A. Osinsky, N. Orishchin, N. Valente, A. Mauze, and J.S. Speck, "Low 1 0 14 cm-3 free carrier concentration in epitaxial β-Ga2O3 grown by MOCVD," APL Materials **8**(2), 021110 (2020).

10. Y. Zhang, C. Joishi, Z. Xia, M. Brenner, S. Lodha, and S. Rajan, "Demonstration of β-(AlxGa1-x)2O3/Ga2O3 double heterostructure field effect transistors," Appl. Phys. Lett. **112**(23), 233503 (2018).

11. S. Krishnamoorthy, Z. Xia, C. Joishi, Y. Zhang, J. McGlone, J. Johnson, M. Brenner, A.R. Arehart, J. Hwang, S. Lodha, and S. Rajan, "Modulation-doped β-(Al0.2Ga0.8)2O3/Ga2O3 field-effect transistor," Appl. Phys. Lett. **111**(2), 023502 (2017).

12. B. Mazumder, J. Sarker, Y. Zhang, J.M. Johnson, M. Zhu, S. Rajan, and J. Hwang, "Atomic scale investigation of chemical heterogeneity in β-(AlxGa1-x)2O3 films using atom probe tomography," Appl. Phys. Lett. **115**(13), 132105 (2019).

13. A.F.M.A.U. Bhuiyan, Z. Feng, J.M. Johnson, H.L. Huang, J. Sarker, M. Zhu, M.R. Karim, B. Mazumder, J. Hwang, and H. Zhao, "Phase transformation in MOCVD growth of (AlxGa1-x)2O3 thin films," APL Materials **8**(3), 031104 (2020).

14. V.M. Bermudez, "The structure of low-index surfaces of β-Ga2O3," Chem. Phys. **323**(2–3), 193–203 (2006).

15. P. Mazzolini, P. Vogt, R. Schewski, C. Wouters, M. Albrecht, and O. Bierwagen, "Faceting and metal-exchange catalysis in (010) β-Ga 2 O 3 thin films homoepitaxially grown by plasma-assisted molecular beam epitaxy," APL Materials **7**(2), 022511 (2019).

16. E. Ahmadi, O.S. Koksaldi, X. Zheng, T. Mates, Y. Oshima, U.K. Mishra, and J.S. Speck, "Demonstration of β-(AlxGa1-x)2O3/β-Ga2O3 modulation doped field-effect transistors with Ge as dopant grown via plasma-assisted molecular beam epitaxy," Appl. Phys. Express **10**(7), 071101 (2017).

17. D. Gogova, M. Schmidbauer, and A. Kwasniewski, "Homo- and heteroepitaxial growth of Sn-doped β-Ga2O3 layers by MOVPE," CrystEngComm **17**(35), 6744–6752 (2015).

18. T. Itoh, A. Mauze, Y. Zhang, and J.S. Speck, "Epitaxial growth of β-Ga2O3 on (110) substrate by plasma-assisted molecular beam epitaxy," Appl. Phys. Lett., **117**, 152105 (2020).

19. P. Vogt, and O. Bierwagen, "Comparison of the growth kinetics of In2O3 and Ga2O3 and their suboxide desorption during plasma-assisted molecular beam epitaxy," Appl. Phys. Lett. **109**(6), 062103 (2016).

20. P. Vogt, and O. Bierwagen, "Reaction kinetics and growth window for plasma-assisted molecular beam epitaxy of Ga2O3: Incorporation of Ga vs. Ga2O desorption," Appl. Phys. Lett. **108**(7), 072101 (2016).

21. M.Y. Tsai, O. Bierwagen, M.E. White, and J.S. Speck, "β-Ga2O3 growth by plasma-assisted molecular beam epitaxy," J. Vac. Sci. Technol. A **28**(2), 354 (2010).

22. E. Ahmadi, O.S. Koksaldi, S.W. Kaun, Y. Oshima, D.B. Short, U.K. Mishra, and J.S. Speck, "Ge doping of β-Ga 2 O 3 films grown by plasma-assisted molecular beam epitaxy," Applied Physics Express **10**(4), 041102 (2017).

23. Y. Oshima, E. Ahmadi, S. Kaun, F. Wu, and J.S. Speck, "Growth and etching characteristics of (001) β-Ga2O3 by plasma-assisted molecular beam epitaxy," Semicond. Sci. Technol. **33**(1), 015013 (2018).

24. V.G. Hill, R. Roy, and E.F. Osborn, "The system alumina-gallia-water," J. Am. Ceram. Soc. **35**(6), 135 (1952).

25. A.F.M.A.U. Bhuiyan, Z. Feng, J.M. Johnson, H.-L. Huang, J. Hwang, and H. Zhao, "MOCVD growth of β-phase (AlxGa1−x)2O3 on (2¯01) β-Ga2O3 substrates," Appl. Phys. Lett. **117**(14), 142107 (2020).

26. P. Mazzolini, A. Falkenstein, C. Wouters, R. Schewski, T. Markurt, Z. Galazka, M. Martin, M. Albrecht, and O. Bierwagen, "Substrate-orientation dependence of β -Ga2O3 (100), (010), (001), and (2¯01) homoepitaxy by indium-mediated metal-exchange catalyzed molecular beam epitaxy (MEXCAT-MBE)," APL Materials **8**(1), 011107 (2020).

27. P. Vogt, O. Brandt, H. Riechert, J. Lähnemann, and O. Bierwagen, "Metal-Exchange Catalysis in the Growth of Sesquioxides: Towards Heterostructures of Transparent Oxide Semiconductors," Phys. Rev. Lett. **119**(19), 196001 (2017).

III. Doping of β-Ga$_2$O$_3$

3.1. Introduction

Compared to other ultra-wide bandgap semiconductors such as AlN and diamond, β-Ga$_2$O$_3$ has shallow hydrogenic donors[1], such as Ge[2–4], Sn[5–7], and Si[8–10]. The availability of cost-effective bulk substrates allows the growth of β-Ga$_2$O$_3$ epitaxial films with superior crystal quality[11–13], which lead to exceptionally low background carrier concentration[14,15]. The crystal orientation of β-Ga$_2$O$_3$ bulk substrates for epitaxial growth is also critical toward the application of β-Ga$_2$O$_3$-based power electronics. Vertical power electron devices are typically large and thus[16,17], the scalability of the β-Ga$_2$O$_3$ bulk substrates is the key to determining which crystal orientation is the most efficient for the epitaxial growth. While the [010] zone is a scalable orientation in β-Ga$_2$O$_3$ crystal system, both (100) and (001) orientations are in the [010] zone, which means they are suitable for large-scale bulk substrates. Moreover, even 100 mm diameter of (001) β-Ga$_2$O$_3$ oriented wafers are commercially available. Therefore, (001) orientation is promising for future large-size power electronics applications[18].

Among all the shallow hydrogenic donors of β-Ga$_2$O$_3$, the importance of Si doping in β-Ga$_2$O$_3$ has been proven by its outstanding electrical properties and thus the application to lateral and vertical electronic devices[19–22]. High-performance enhancement-mode metal-oxide semiconductor field effect transistors (MOSFETs)[23] and current aperture vertical electron transistors (CAVETs)[24,25] have been achieved by Si-doped β-Ga$_2$O$_3$ films. While Ion implantation is a well-established technique to obtain Si-doping at certain area in β-Ga$_2$O$_3$ films, damage by ion radiation is inevitable during this process[26]. The Si-doping for

55

β-Ga$_2$O$_3$ epitaxial film has been widely studied in different growth methods such as metal-organic chemical vapor deposition (MOCVD)[9,27] , halide vapor phase epitaxy (HVPE)[28] ,and pulsed laser deposition (PLD)[29]. Moreover, for the application of β-(Al$_x$Ga$_{1-x}$)$_2$O$_3$/β-Ga$_2$O$_3$ heterostructures, Si-doping in the β-(Al$_x$Ga$_{1-x}$)$_2$O$_3$ has revealed its importance by showing superior conductivity[30] and record-low contact resistance[31]. On the other hand, the rapid oxidation of Si source in molecular beam epitaxy (MBE) has limited its ability of Si doping to δ-doping[32]. Effusion cell with an endplate[33] and Si suboxide (SiO) source[34] have been used to achieve controllable Si-doping in β-Ga$_2$O$_3$ epitaxial films grown by MBE. Due to the existence of a high background O$_2$ partial pressure, typically >10^{-5} torr, and the presence of active oxygen (presumably atomic oxygen O) inside the MBE growth environment, the Si source material in the effusion cell needs to be protected from oxidation. In this work, we report the continuous doping of Si in β-Ga$_2$O$_3$ epitaxial films on (010) and (001) substrates by utilizing a valved effusion cell.

3.2 Growth and Si doping techniques

β-Ga$_2$O$_3$ epitaxial films were grown on Fe-doped (010) and (001) semi-insulating β-Ga$_2$O$_3$ substrates from Novel Crystal Technology by plasma-assisted MBE (PAMBE). The growth temperature of was varied from 700 °C to 800 °C. The MBE system was equipped with a Veeco Unibulb radio-frequency plasma source running at 200 W with a foreline pressure of 60 torr for the generation of O plasma to produce 1% - 2% atomic O from pure O$_2$ gas. Prior to the epitaxial growth, the substrate was Ga polished, and O polished at a substrate temperature of 800 °C to remove the impurities on the surface of β-Ga$_2$O$_3$ substrates. Ga polishing is proven to be capable of effectively removing impurities and

chemical-mechanical polish (CMP)-related damage on the surface and smoothing the surface of both (010) and (001) substrates[2,35]. O polishing by O plasma can further remove impurities to make sure the surface is ready for epitaxial growth. For Si doping, the temperature of the Si effusion cell was varied from 900 °C to 1200 °C. Figure 3.1 shows the schematic of a valved effusion cell used in this study. The cell uses a needle valve to control the flux into the growth chamber. The effusion cell of Si source is designed to prevent the exposure of Si to the high oxygen background in the chamber while provide Si flux at the same time. The needle valve on the top of the crucible minimizes the exposure of the crucible to the environment in the main growth chamber, while sustaining the Si flux from the source material. When the needle valve is fully open (100% open), the needle and the body seats are separated so that the Si flux can flow out of the cell through the openings. When the valve is fully closed (0% open), the needle and the body seats have no gap between each other, which results in no flux between the effusion cell and the growth. The opening of the needle valve is controlled by a programmable motor with a precision valve opening of ~2.5 μm level to further control the Si doping concentration. While the Si flux can be controlled by changing the cell temperature, this requires time for cooling down/heating up and stabilizing of the Si flux, the needle valve can instantly change the Si flux to achieve controllable Si doping. During the growth, the Ga flux was varied from 1.0×10^{-7} to 3.0×10^{-7} torr for conventional growth. We further performed metal-oxide catalyzed epitaxy (MOCATAXY) to improve the crystal quality of Si-doped (010) and (001) β-Ga_2O_3 epitaxial films[36–38]. During the MOCATAXY growth, In flux was provided simultaneously with Ga flux to serve as a catalyst for the β-Ga_2O_3 epitaxial growth[39]. Previously, the MOCATAXY growth showed that the growth rate of β-Ga_2O_3 epitaxial films

were significantly enhanced by introducing an In flux into the MBE growth environment[37]. This improvement of the growth rate of β-Ga$_2$O$_3$ epitaxial films is due to the catalytic mechanism of In during the growth of β-Ga$_2$O$_3$. In the conventional MBE growth, Ga can only access atomic O as the active oxygen flux. On the other hand, in the MOCATAXY growth environment, In catalyst layer can access more oxygen, presumably molecular O$_2$. Subsequently, a metal-exchange mechanism between Ga and In then allows Ga to preferentially incorporate in the β-Ga$_2$O$_3$ epitaxial film over In. As all the In is replaced by Ga during the growth, pure β-Ga$_2$O$_3$ epitaxial films with high growth rates can be grown at sufficiently high Ga fluxes. In addition, the maximum growth temperature can also be enhanced due to the suppression of Ga$_2$O suboxide desorption by the presence of In in the MBE growth environment[40]. Here, the Ga flux was fixed at 2.5×10^{-7} torr with In flux at 4.0×10^{-7} torr for catalyzed growth. Prior to the growth of the Si-doped β-Ga$_2$O$_3$ epitaxial films, unintentionally doped (UID) buffer layer was grown to prevent the impurities on the surface of the substrate from incorporating into the Si-doped layer. Followed by the UID buffer layer, a 2-nm-thick β-(Al$_{1-x}$Ga$_x$)$_2$O$_3$ spacer layer with a target Al composition of 2 to 3% was grown to enable the observation of thickness fringes in high resolution x-ray diffraction (HRXRD) ω-2θ scans, which helps determine the thickness of Si-doped layer and characterize the crystal quality. Reflection high energy electron diffraction (RHEED) was used to observe the surface structure during the MBE growth. Surface morphologies of the epitaxial films were characterized by atomic force microscopy (AFM). For the determination of Si concentrations in the β-Ga$_2$O$_3$ epitaxial films, secondary ion mass spectrometry (SIMS) using a CAMECA IMS 7f tool. Hall measurements were performed with Ti/Au electrodes deposited on the corners of the samples in van der Pauw geometry.
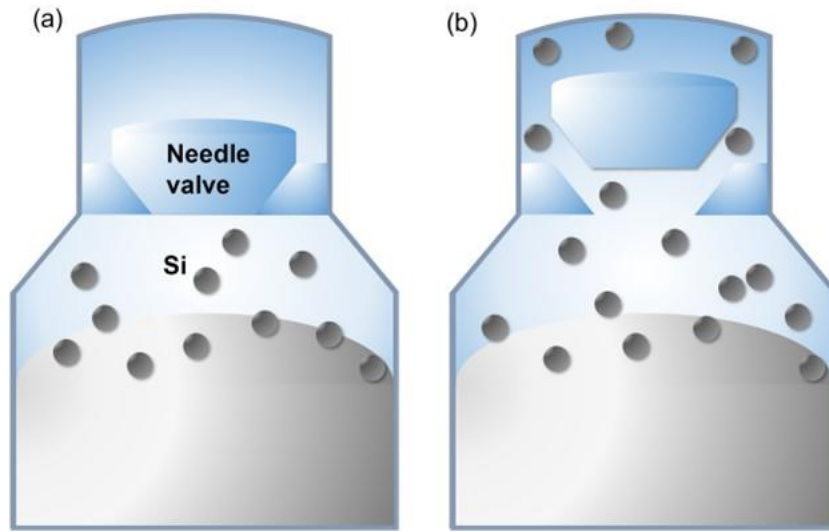
Figure 3.1. (a) The schematic of the valved effusion cell at the needle valve aperture of 0% and (b) the needle valve aperture of 100%. The needle valve aperture can be varied continuously from 0% to 100% by a programmable motor to control the Si doping concentration[41].

3.3 Si doping on (010) substrates

During the growth, RHEED patterns were monitored to confirm the surface structure of Si-doping in β-Ga$_2$O$_3$ epitaxial films. Figure 3.2 (a), (b) shows the RHEED patterns of conventional MBE growth and (c), (d) MOCATAXY growth of Si-doped β-Ga$_2$O$_3$ epitaxial films. The thickness of the UID layers and Si-doped layers grown by both grow methods were 100 nm and 200 nm, respectively. The RHEED images of conventional MBE growth of UID buffer layer and Si-doped β-Ga$_2$O$_3$ epitaxial films did not show clear streaky patterns indictive of rough surface morphologies. The pattern of the Si-doped film was even more blurry than that of the UID buffer layer, which indicates surface roughening during Si

59

doping of β-Ga$_2$O$_3$ by conventional MBE growth. This suggests that Si can be an anti-surfactant in the β-Ga$_2$O$_3$ epitaxial growth, which is also confirmed by the following HRXRD and AFM results. On the other hand, both UID buffer layer and Si-doped film grown by MOCATAXY growth showed clear streaky patterns during the whole growth.
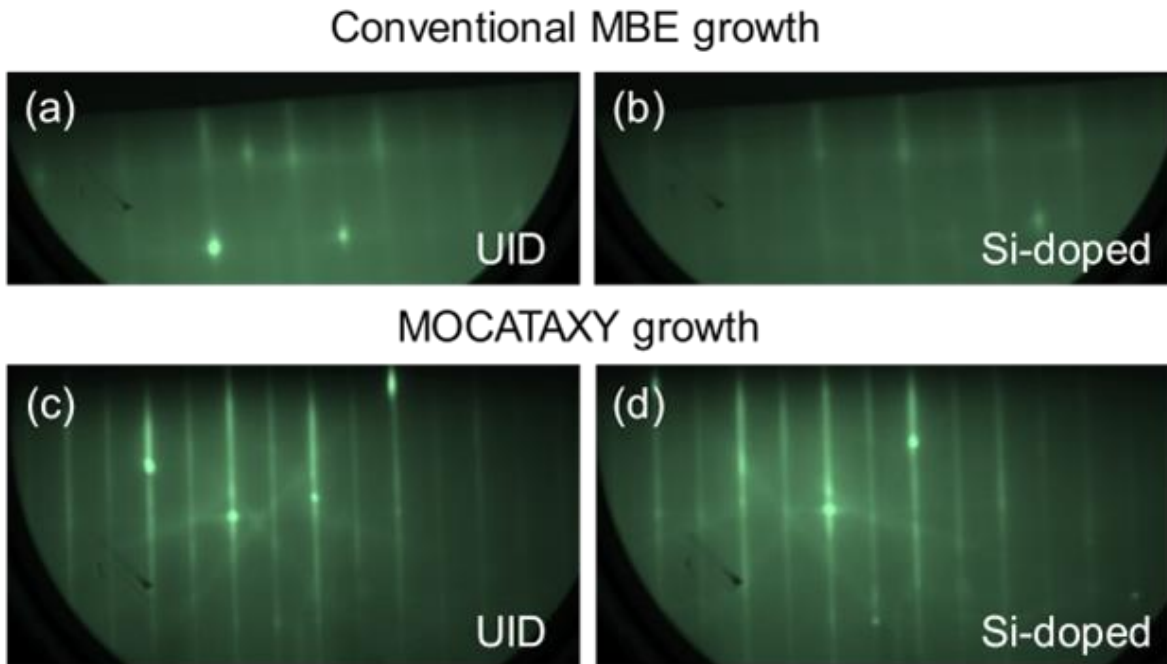
Figure 3.2. RHHED images of conventional MBE growth of β-Ga$_2$O$_3$ (a) UID buffer layer (thickness: 100 nm) and (b) Si-doped film (thickness: 200 nm). The patterns are not clear on the UID films and got even more blurry on the Si-doped film indicative of surface roughing during Si-doping of β-Ga$_2$O$_3$. On the other hand, MOCATXY-grown β-Ga$_2$O$_3$ (c) UID buffer layer (thickness: 100 nm) and (d) Si-doped film (thickness: 200 nm) shows similarly clear streaky patterns. This suggests that MOCATAXY-grown Si-doped films have smooth surface morphologies and no surface roughening during Si-doping[41].

Figure 3.3 shows the SIMS result of a stack of Si-doped β-Ga$_2$O$_3$ layers separated by UID layers grown by MOCATAXY on (010) β-Ga$_2$O$_3$ substrate. The spike of Si concentration at the film/substrate interface was due to the residual impurities on the surface of the β-Ga$_2$O$_3$ substrate though Ga polishing has reduced the Si concentration by more than one order of magnitude[42]. Continuous Si doping in β-Ga$_2$O$_3$ epitaxial films with flat doping profiles and sharp turn-on/off was achieved by exploiting the valved effusion cell. The Si doping concentration was able to be either controlled by the aperture of the needle valve or the temperature of the effusion cell with an upper limit of $\sim 1.0 \times 10^{20}$ cm^{-3} and a lower limit below the background impurity level of $\sim 5 \times 10^{16}$ cm^{-3}, which is the detection limit of SIMS measurement. The temperature of the Si effusion cell was varied from 900 °C to 1200 °C. At the effusion cell temperature of 1000 °C, the Si concentration was approximately 4.0×10^{17} cm^{-3} with the needle valve opening of 20%. When the needle valve was fully open (100%), the Si concentration increased to $\sim 2.0 \times 10^{18}$ cm^{-3}, which is 5 times larger than that of the needle opening at 20%. This result demonstrates that the linear control of Si concentration in β-Ga$_2$O$_3$ epitaxial film was realized by utilizing the valved effusion cell. On the other hand, some surface segregation effect was observed in the turn-off of the doping profiles, which indicates possible surface riding of Si or a "memory" effect during the growth of β-Ga$_2$O$_3$ epitaxial films on (010) β-Ga$_2$O$_3$ substrates.
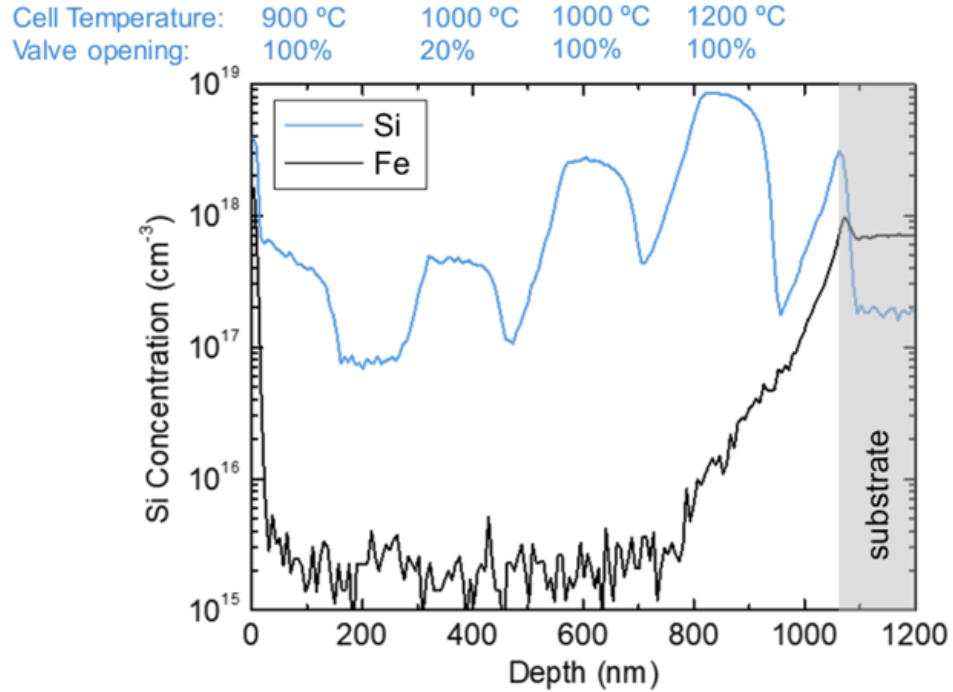
Figure 3.3: SIMS profile of a β-Ga$_2$O$_3$ (010) film with different Si doping levels separated by UID layers grown by MOCATAXY growth at a substrate temperature of 800°C. The Si concentrations were controlled by varying effusion cell temperatures from 900°C to 1200°C and needle valve apertures at 20% opening and 100% opening. The Fe profile is an indicator of the interface between the epitaxial film and the Fe-doped (010) semi-insulating substrate[41].

Additional Si-doped (010) β-Ga$_2$O$_3$ SIMS-stack sample was prepared to investigate the Si doping behaviors at high temperatures (>1000 °C) range. Each Si-doped layer was grown for 240 nm with a growth rate of 4 nm/min to confirm the stability of Si doping during the growth. The SIMS profile of Si-doped (010) β-Ga$_2$O$_3$ film shown in Fig 3.4 (a) reveals the cell temperature dependence of Si doping concentrations. The Si-doped layers with Si effusion cell temperatures at 1200 °C, 1100 °C, and 1000 °C showed flat Si doping profiles

and sharp turn on/off. Moreover, two doping regions were observed from a single Si-doped layer. The first region (Region A) of the doping has slightly larger Si concentration than the following region (Region B). Considering the needle valve is closed during the growth of the UID layer (prior to the Si-doped layers), excessive gas species including Si and suboxide SiO that could be active dopants after incorporated into the β-Ga_2O_3 epitaxial films, were accumulated inside the Si effusion cell. Since this phenomenon is more obvious when the Si effusion cell is at a higher temperature, this suggests that the continuous Si doping by the valved cell is conducted by gas species that are able to be accumulated in an effusion cell[43,44].

Figure 3.4 (b) shows the apparent activation energy extracted from the Arrhenius plot of the cell temperatures and Si doping concentrations. To derive the activation energy, the Arrhenius equation, which is shown in the following, is used,

$$k = A exp\left(\frac{-E_a}{RT}\right) \text{ (eqn. 3.1)}$$

whereas E_a is the apparent activation energy of the Si effusion cell, T is the temperature in the degree of K, R (8.617×10^{-5} eV·K^{-1}) is the idea gas constant, and A is the coefficient of the Arrhenius equation. By plotting the relationship between the reciprocal of absolute temperature and the SIMS concentration of Si, the graph exhibits a linear dependence of doping concentration on the inverse of cell temperature. The plot can be fitted by a natural exponential function in the shape of,

$$y = A exp(-Bx) \text{ (eqn. 3.2)}$$

Whereas y is the SIMS concentration of Si, x is the reciprocal of absolute temperature (1/T), A and B are the results of fitting by the natural exponential function to the plot. Here, the apparent activation energy can be derived from the value of B since $E_a = R \cdot B$.

The activation energy showed a value of approximately 1.3 eV, which was lower than that of the element Si flux ($\sim$5.0 eV)[45] or SiO flux ($\sim$3.6 eV)[34]. However, the identification of exact gas species coming out from the Si effusion cell needs to be further investigated at actual MBE growth conditions and is beyond the scope of this study. Future studies can be conducted by using a gas analyzer that is mounted directly to identify the gas species coming from the valved effusion cell.
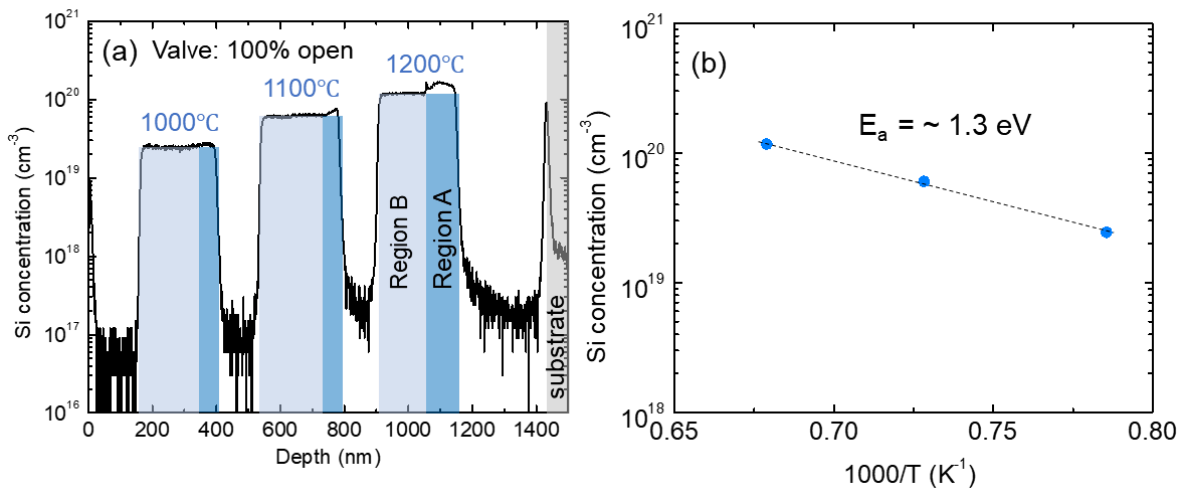
Figure 3.4: (a) SIMS profile of a Si-doped β-Ga$_2$O$_3$ (010) SIMS-stack sample with 240 nm Si-doped layers grown at different Si cell temperatures separated by UID spacer layers. (b) Arrhenius plot of the cell temperatures and Si doping concentrations, showing an apparent activation energy of $\sim$1.3 eV[41].

The crystal quality of the Si-doped (010) β-Ga$_2$O$_3$ epitaxial films was investigated by HRXRD shown in Fig. 3.5. While the films with a film thickness of 200 nm and Si concentration under 1×10^{17} cm^{-3} shows clear thickness fringes, indicating high quality film and abrupt substrate-film interface. Thickness fringes were not observed from films with Si

concentrations beyond 6×10^{17} cm^{-3}, either by MOCATAXY (film thickness: 200 nm) or by conventional PAMBE (film thickness: 150 nm). In addition, a peak appears next to the (020) β-Ga$_2$O$_3$ peak on the higher angle side at Si concentrations larger than 6.0×10^{17} cm^{-3}. This can be attributed to the strain introduction while Si are doped into (010) β-Ga$_2$O$_3$ films. The coherency strain calculated from the peak separation[46] from the β-Ga$_2$O$_3$ (020) peak showed a value of -0.023%, which indicates Si doping might introduce tensile stress into β-Ga$_2$O$_3$ epitaxial films during the growth. Similar shoulder peaks indicative of strain introduction into the Si ion-implanted β-Ga$_2$O$_3$ films were observed in previous studies[47,48]. The ion-implanted β-Ga$_2$O$_3$ film with relatively high Si concentrations showed an κ-phase transition when it was ion-implanted at room temperature. Further work is ongoing to understand the peak separation in the HRXRD results.

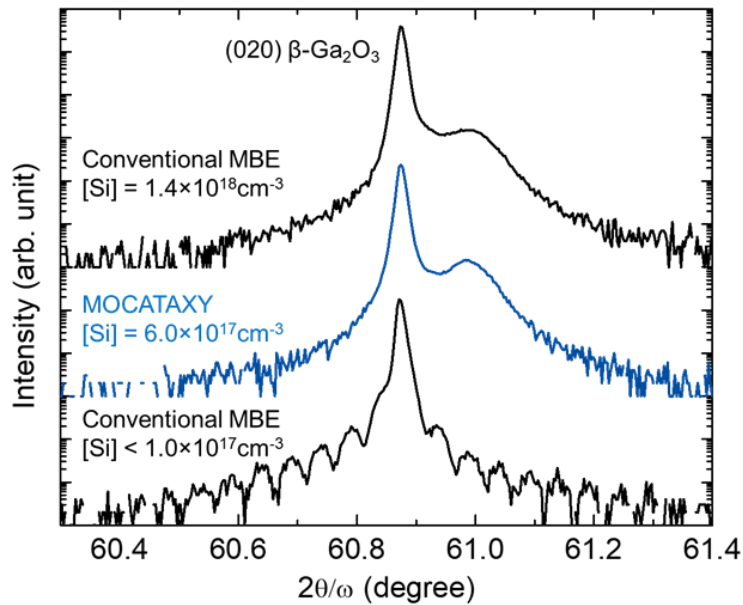Figure 3.5. (a) HRXRD 2θ-ω scan of Si-doped β-Ga$_2$O$_3$ (010) films grown by conventional MBE and (b) (c) MOCATAXY. In (b) and (c), the broad peak next to the (020) is the characteristic of strain introduced to the β-Ga$_2$O$_3$ (010) films while Si are doped in the

$>10^{17}$ cm^{-3} range. On the other hand, clear thickness fringes was observed at the Si concentration $<10^{17}$ cm^{-3}.

Figure 3.6 shows the AFM images of Si-doped β-Ga$_2$O$_3$ films grown by conventional MBE and MOCATAXY. The surface morphologies of Si-doped β-Ga$_2$O$_3$ films with Si concentrations above mid-10^{17} cm^{-3} range have larger RMS roughness than films with Si concentrations under 10^{16} cm^{-3}. Hall measurement was performed on Si-doped β-Ga$_2$O$_3$ epitaxial films grown on (010) substrates by conventional MBE growth and MOCATAXY growth. While MOCATAXY-grown Si-doped (010) films showed 1.8×10^{18} cm^{-3} Hall concentration and 72 cm^2/Vs mobility, conventional MBE-grown Si-doped (010) films showed mobility under 10 or even unmeasurable results. This suggests that MOCATAXY growth can enhance the electronic properties by improving the crystal quality of β-Ga$_2$O$_3$ epitaxial films. Therefore, the HRXRD,AFM and Hall results suggest that Si is potentially an anti-surfactant during the growth of β-Ga$_2$O$_3$ epitaxial films causing microstructure degradation and surface roughening along with the previous studies showing Si is known as an anti-surfactant in GaN growth[49,50]. MOCATAXY growth showed its potential to act as surfactant to counteract the anti-surfactant effect of Si in β-Ga$_2$O$_3$ epitaxial growth.
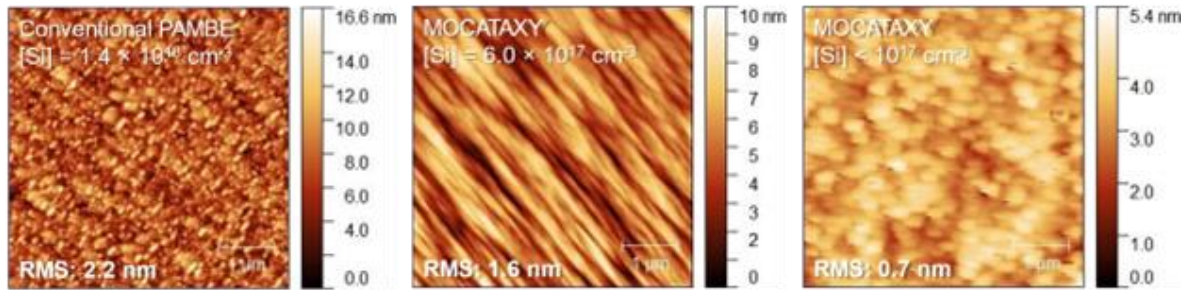
Figure 3.6. (a) AFM images of Si-doped β-Ga$_2$O$_3$ (010) films grown by conventional MBE and (b) (c) MOCATAXY. Grooved features along the [001] direction can be observed from the films grown by either conventional MBE growth and MOCCATAXY growth. The value of RMS roughness on MOCATAXY-grown β-Ga$_2$O$_3$ epitaxial films are lower than that of conventional MBE-grown films, which corresponds to the streaky patterns on MOCATAXY-grown films from the RHEED measurement[41].

3.4 Si doping on (001) substrates

The Si doping availability of β-Ga$_2$O$_3$ was further investigated on the scalable (001) substrates. Since the (001) substrates were co-loaded with the (010) substrates into the MBE system, the growth conditions of (001) Si-doped films were identical to those on the (010) substrates, which were shown in the II. Growth and Si doping part. By growing with MOCATAXY, co-loaded (010) and (001) β-Ga$_2$O$_3$ films exhibited the best crystal qualities at the same growth conditions, which were confirmed by Mauze et al[37]. A (001) β-Ga$_2$O$_3$ substrate that was co-loaded with the (010) substrate for the growth of Si-doped SIMS stack sample with a same growth condition as shown in Figure 3.4. The growth rate on (001) β-Ga$_2$O$_3$ substrate was lower than that of the (010) substrate, which corresponds to the previous study showing that (010) has the highest growth rate among all the crystal

67

orientations of β-Ga$_2$O$_3$[35]. Figure 3.7 shows the SIMS doping profile of the Si-doped β-Ga$_2$O$_3$ epitaxial layers with different Si effusion cell temperatures of 1000 °C, 1100 °C and 1200 °C. On the other hand, the turn on/off of the Si-doped layers was not as sharp as that of the layers grown on (010) β-Ga$_2$O$_3$ substrates. Additionally, the difference between region A and region B, which was mentioned in the Si doping of (010) β-Ga$_2$O$_3$ epitaxial films, was not as obvious as that of on the (010) β-Ga$_2$O$_3$ substrates. These different behaviors of Si doping on (001) and (010) substrates can be attributed to the lower growth rate on (001) substrates compared to (010) substrates and different Si incorporation process on the different crystal orientations. Moreover, the Si SIMS concentration was lower in (001) β-Ga$_2$O$_3$ epitaxial films than that of the (010) β-Ga$_2$O$_3$ layers even though the growth rate on (001) was lower than that of (010) substrates. The background Si concentration of β-Ga$_2$O$_3$ epitaxial films grown on (001) substrate is higher than that of (010) when comparing the Si concentrations of the UID layers. This further suggests that the mechanism of Si incorporation is different from that on the (010) substrates. Figure 3.7 (b) shows the Arrhenius plot of the temperature dependence of Si concentrations measured by SIMS, indicating an apparent activation energy of 1.3 eV. The value of the activation energy is the same as that of the Si-doped β-Ga$_2$O$_3$ epitaxial films grown on (010) substrates, indicating a similar Si incorporating behavior on both the (001) and (010) orientations of β-Ga$_2$O$_3$ grown by PAMBE.
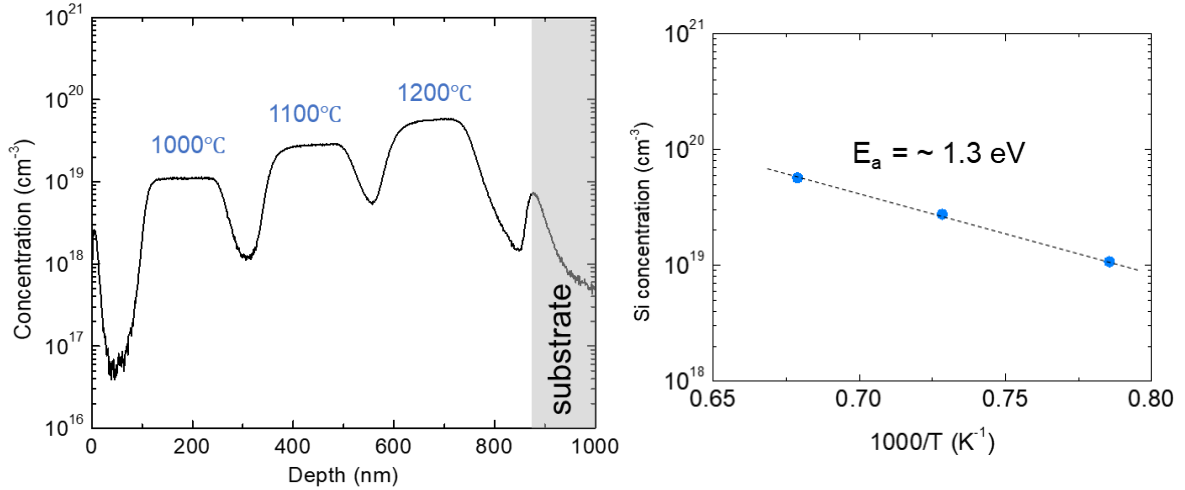
Figure 3.7. SIMS profile of Si-doped layers with different Si effusion cell temperatures separated by UID layers. The (001) Si-doped β-Ga$_2$O$_3$ SIMS stack was co-loaded with the (010) Si-doped β-Ga$_2$O$_3$ SIMS stack sample. The Arrhenius plot shows an apparent activation energy of ~ 1.3 eV.

Figure 3.8 shows the HRXRD and AFM results of continuous Si-doped β-Ga$_2$O$_3$ films grown on (001) substrates by MOCATAXY growth. Clear thickness fringes in the XRD patterns indicate the Si-doped (001) β-Ga$_2$O$_3$ epitaxial films have superior crystal quality and smooth surface morphology even at the Si concentration of high 10^{18} cm^{-3} range. The growth rates on (001) substrates were 5.0 nm/min, which corresponds to the results from previous MOCATAXY-grown UID films[37,38]. The RHEED patterns during the MOCATAXY growth of Si-doped β-Ga$_2$O$_3$ epitaxial films showed clear streaky patterns, along with the AFM image showing the smooth surface morphology. The results of Hall measurements of the Si-doped films on (001) substrates are shown in the figures. For the 200-nm-thick Si-doped film with Hall electron concentration of 3×10^{18} cm^{-3}, the electron

mobility was 67 cm^2/Vs. The electron mobility of this Si-doped film is superior to previous studies on Sn-doped and Ge-doped β-Ga$_2$O$_3$ epitaxial film grown on (001) substrates[18,37,51].
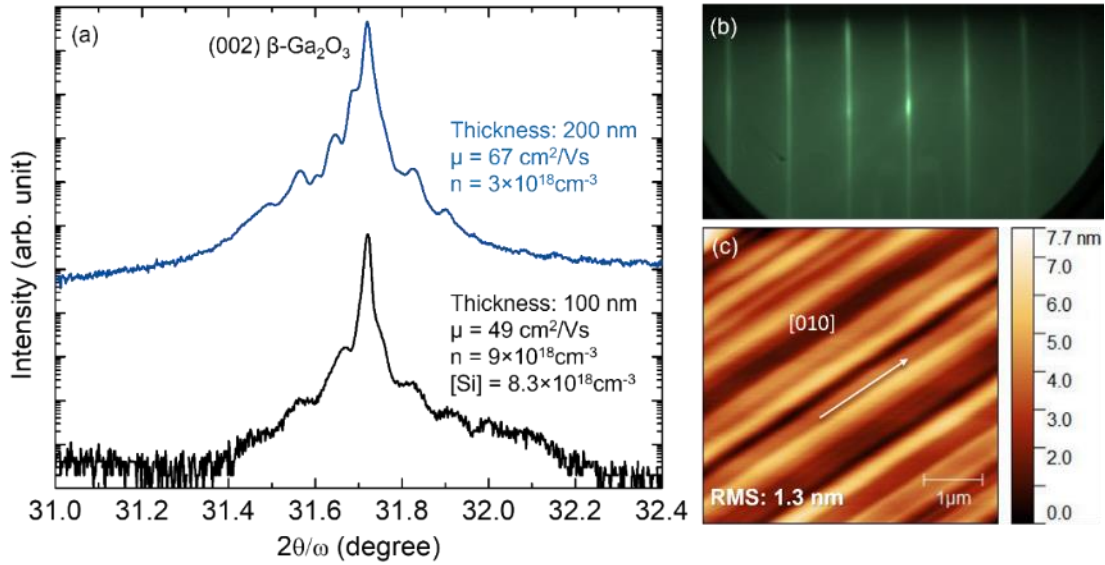
Figure 3.8. (a) HRXRD results of Si-doped β-Ga$_2$O$_3$ films grown on (001) substrates by MOCATAXY growth at a substrate temperature of 800°C. Thickness fringes were confirmed at a Si concentration up to 8.3×10^{18} cm^{-3}. (b) Clear streaky RHEED patterns were observed during the growth of Si-doped β-Ga$_2$O$_3$ film on (001) substrate. (c) AFM image of Si-doped 200-nm-thick β-Ga$_2$O$_3$ films grown on (001) substrates with an RMS roughness as low as 1.3 nm[41].

Figure 3.9 shows the SIMS depth profile of this 100-nm-thick Si-doped β-Ga$_2$O$_3$ epitaxial film grown on (001) substrate with the Hall measured electron concentration of 9×10^{18} cm^{-3} and electron mobility of 49 cm^2/Vs. This result shows that flat Si doping profile at 8.3×10^{18} cm^{-3} with sharp turn on was achieved throughout the Si-doped (001) β-Ga$_2$O$_3$ epitaxial film. The Si concentration is approximately 1.0×10^{19} cm^{-3} at the interface between

70

the Fe-doped substrate and the epitaxial film. This interface impurity of Si, which is due to the contamination from the atmosphere during the storage, preparation and handling of the β-Ga$_2$O$_3$ substrates, can vary from 1.0×10^{18} cm^{-3} to 1.0×10^{20} cm^{-3}. This wide range of Si impurity concentration can be related to the uncertainty of Additionally, this indicates that the doped Si has sufficiently high ionization efficiency, which is also proven by previous studies suggesting that Si is a shallow donor in the β-Ga$_2$O$_3$ materials system[1]. Therefore, the continuous Si-doping capability in β-Ga$_2$O$_3$ epitaxial films grown on (001) substrates was achieved in the range from below the background impurity level to a heavy doping level as high as $\sim 1.0\times10^{20}$ cm^{-3}.
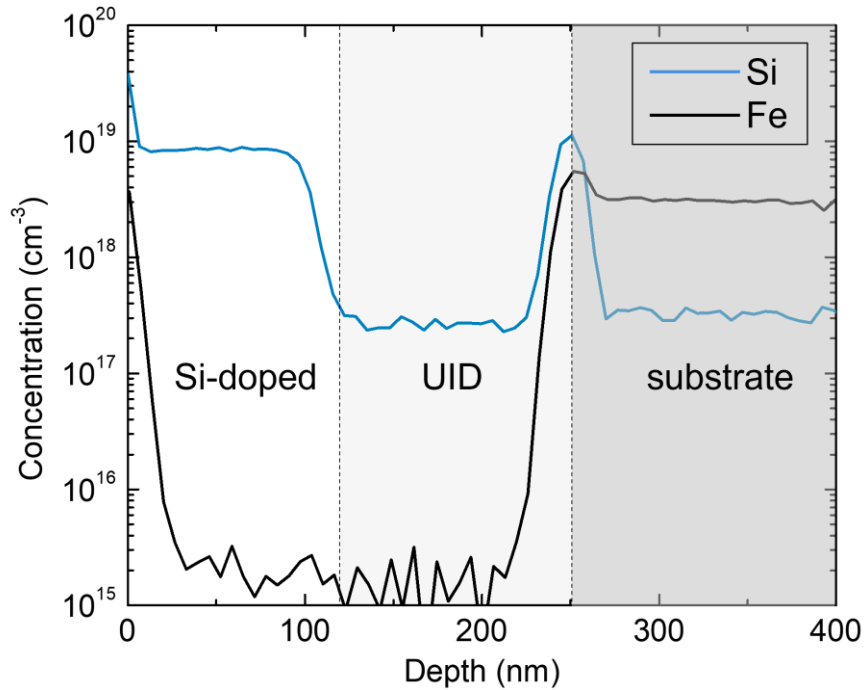

Figure 3.9. SIMS depth profile of a 100-nm-thick Si-doped β-Ga$_2$O$_3$ film grown on Fe-doped (001) substrate by MOCATAXY growth. Flat Si doping profile was obtained by

utilizing the valved effusion cell. The spike of Si concentration at the interface between the UID layer and the substrate is due to the residual impurities on the surface of the substrate[41].

In conclusion, continuous Si doping in β-Ga$_2$O$_3$ epitaxial films on (010) and (001) substrates grown by PAMBE was achieved by utilizing the valved effusion cell for the Si source material. By varying the effusion cell temperatures and valve aperture, the Si doping concentration can be precisely controlled on a linear scale corresponding to the opening of the needle vale. The clear thickness fringes confirmed from the HRXRD results prove that the Si-doped MOCATAXY-grown β-Ga$_2$O$_3$ epitaxial films exhibited high crystal quality. The strain introduced into the Si-doped β-Ga$_2$O$_3$ epitaxial films can potentially be resolved by annealing the films at high temperature. In addition, AFM images showed that the surface morphology of Si-doped films were smooth with a value of RMS roughness of around 1.0 nm. Controllable Si continuous doping is crucial to the β-Ga$_2$O$_3$ toward the application of power electronics, especially vertical devices that require large uniform donor doping area.

3.5 Mg doping on (001) substrates

Acceptor doping on the scalable (001) substrates is important for forming semi-insulating layers in large-size electronics, especially for the formation of current-blocking layers in a vertical power device such as current aperture vertical MOSFETs[25]. To understand the Mg doping behavior in the (001) β-Ga$_2$O$_3$ epitaxial films grown by PAMBE, a SIMS-stack structure was designed to have approximately 300-nm-thick Mg-doped layers with the effusion cell temperatures from 170 °C to 200 °C in a step of 5 °C. MOCATAXY

growth with a growth rate of approximately 5.0 nm/min at a substrate temperature of 750 °C was used for this SIMS-stack sample. Between the Mg-doped layers, UID layers with similar film thickness were grown to separate the Mg-doped layers at different Mg effusion cell temperatures for clearer identification of Mg doping levels. The SIMS results of this sample is shown in figure 3.10. A Mg concentration spike at the interface between the substrate and the β-Ga_2O_3 epitaxial film, which is in the range of 1.0×10^{17} cm^{-3}, reflects the surface impurities from the atmosphere during sample preparation and handling. Moreover, the growth of UID layers between the Mg-doped layers make the time for the stabilization of Mg effusion cell after changing of the temperature set point. On the other hand, the Mg background levels in the UID β-Ga_2O_3 layers became higher as the Mg effusion cell temperature increased. In the first UID layer, the Mg background level is in the range of 5×10^{16} cm^{-3}, and the background levels increased as the cell temperature was ramped up. This indicates that the Mg background levels are affected by the Mg effusion cell temperatures. The increased background level of Mg can be further controlled by optimizing the shutter unit to prevent leaking of Mg from the effusion cell when the shutter is closed. Another approach to reduce the Mg background levels is to use valved effusion cell. By fully closing the needle valve when the shutter is closed, the leakage of Mg flux from the effusion can be sealed to reduce the Mg background level if other layers such as lightly doped n-type drift layer or heavily doped contact layer is being grown when the Mg cell temperature is relatively high such as 150 °C.
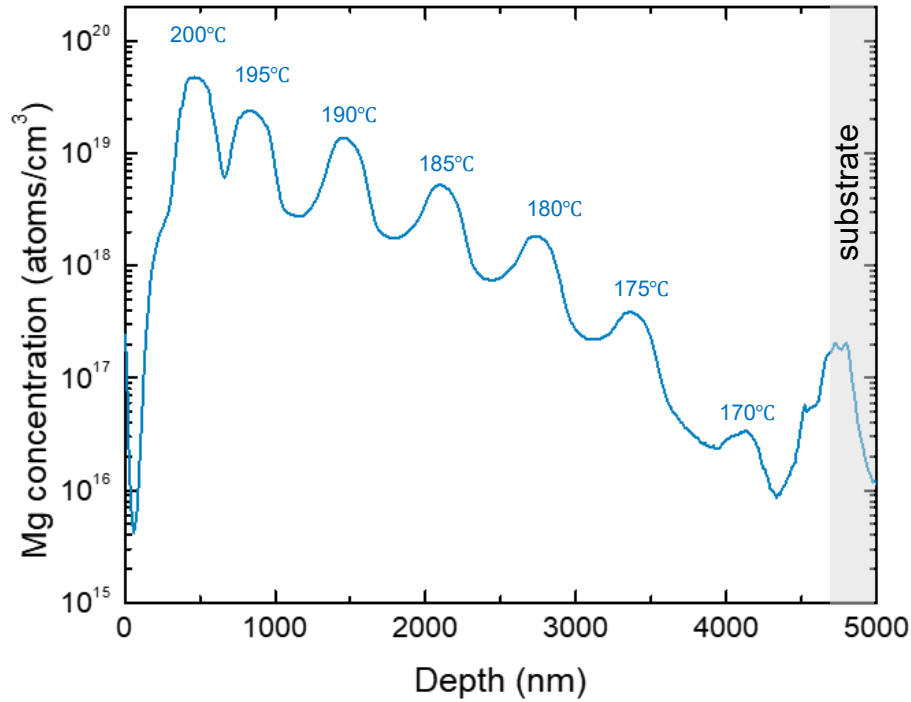
Figure 3.10. SIMS profile of a β-Ga$_2$O$_3$ epitaxial film with Mg-doped layers at different Mg cell temperatures. UID layers were grown between the Mg-doped layers for clearer identification of doping levels and stabilization of Mg effusion cell after changing of temperature set point. The Mg effusion cell temperatures are varied from 170 °C to 200 °C in a step of 5 °C.

To further understand the Mg doping behaviors in the (001) β-Ga$_2$O$_3$ epitaxial films, the Si doping concentrations obtained by SIMS measurement were plotted against the reciprocal of the Mg effusion cell temperatures. By fitting this Arrhenius plot, an apparent activation energy E$_a$ of approximately 2.96 eV was derived from the results from the natural function approximation. This value of activation energy corresponds to the results from the activation energy of Mg-doped β-Ga$_2$O$_3$ epitaxial films grown on (010) substrates (~3.0 eV) [52].
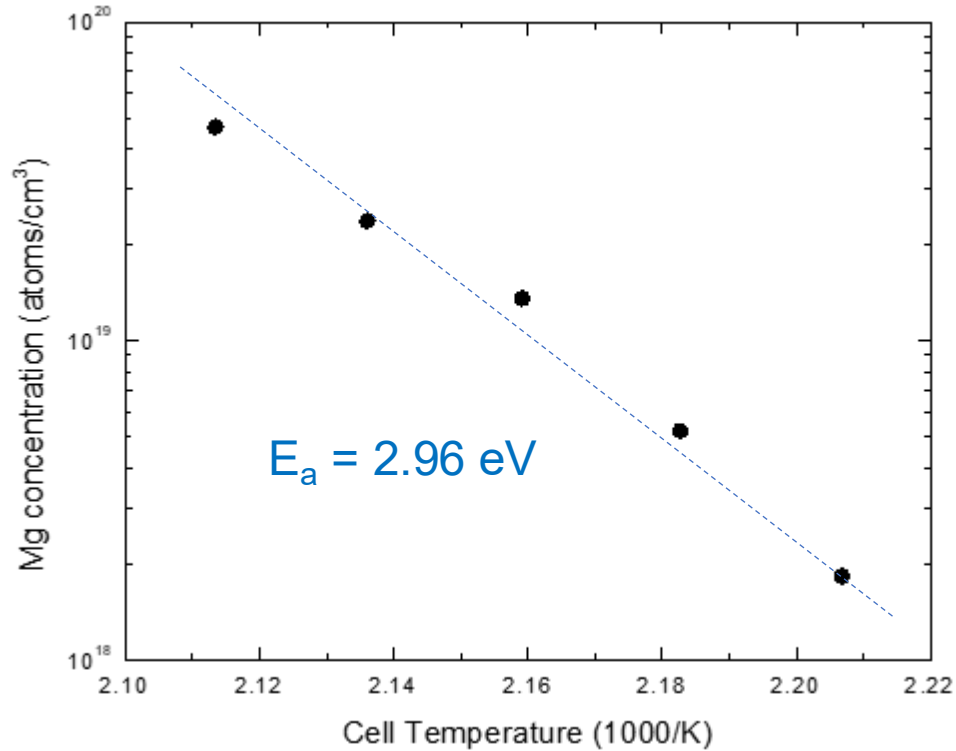
Figure 3.11. The apparent activation energy derived from the Arrhenius plot shows a value of approximately 2.96 eV for Mg doping concentration in (001) β-Ga$_2$O$_3$ films.

The behavior of Mg doping in (001) β-Ga$_2$O$_3$ epitaxial films by PAMBE is controllable and consistent within a wide range of 1.0×10^{16} cm^{-3} to 1.0×10^{20} cm^{-3}. This doping controllability is similar to the results from Mg-doped (010) β-Ga$_2$O$_3$ epitaxial films[52]. The growth conditions of β-Ga$_2$O$_3$ epitaxial films can be further investigated by varying the substrate temperatures and Ga fluxes. Additionally, the diffusion behavior of Mg in the (001) β-Ga$_2$O$_3$ epitaxial films still has room to explore. The robustness of Mg doping controllability is important to the formation of semi-insulating layers in the β-Ga$_2$O$_3$ epitaxial films for the further development of vertical power electronics.

3.6 Summary

The doping controllability of Si in (010) and (001) β-Ga$_2$O$_3$ epitaxial films and Mg in (001) β-Ga$_2$O$_3$ epitaxial films by PAMBE are investigated. While Si doping by elemental Si source with normal effusion cell is limited to δ-doping due to the repaid oxidation of the Si surface in an oxide MBE environment, continuous Si doping on (010) and scalable (001) substrates is achieved by utilizing the valved Si effusion cell. The Si doping concentration can be controlled by varying the temperatures of the effusion cell. Moreover, changing the opening of the needle valve can precisely and instantly change the Si doping concentration in the β-Ga$_2$O$_3$ epitaxial films. On the other hand, the surface morphologies of Si-doped β-Ga$_2$O$_3$ epitaxial films with a Si concentration larger than 1.0×10^{18} cm^{-3} need to be improved by optimizing the growth conditions. HRXRD results also revealed that strain was introduced in the Si-doped β-Ga$_2$O$_3$ epitaxial films with relatively high Si doping concentrations. Further investigation of the strains can be conducted by annealing the Si-doped β-Ga$_2$O$_3$ epitaxial films at different temperatures and pressures. The transport properties of Si-doped β-Ga$_2$O$_3$ epitaxial films showed nearly 100% ionization efficiency, which is promising for the formation of layers with high conductivity. Especially for the heavily doping regime with n-type concentration higher than 1.0×10^{20} cm^{-3}, Sn shows significant decline of conductivity due to self-compensation[6], while heavily Si doped β-Ga$_2$O$_3$ epitaxial films show outstanding conductivity.

Mg doping on (001) β-Ga$_2$O$_3$ substrate by PAMBE was investigated by changing the temperature of the Mg effusion cell and measured by SIMS. The doping behavior on (001) substrate is similar to that on (010) substrate, with an approximately same apparent activation energy (~3.0 eV) derived from the Arrhenius plots. The crystal quality and

surface morphology can be further investigated by HRXRD and AFM for the optimization of growth conditions. A valved effusion cell can be used to reduce the background level of Mg during the growth when the cell is hot. Consequently, the controllability of n-type dopant Si and acceptor dopant Mg by MBE on the scalable (001) substrate is critical to the application of large-scale vertical power electronic devices. These results suggest that MBE is a robust growth technique that enables formation of layers with different doping levels to achieve high-quality lightly n-type doped drift layers, heavily n-type doped ohmic contact layers and semi-insulating current blocking layers. Furthermore, the capability of controlling acceptor doping levels can be used to compensate the Si impurity at the regrowth interface during the fabrication process.

References

1. A.T. Neal, S. Mou, S. Rafique, H. Zhao, E. Ahmadi, J.S. Speck, K.T. Stevens, J.D. Blevins, D.B. Thomson, N. Moser, K.D. Chabak, and G.H. Jessen, "Donors and deep acceptors in β-Ga2O3," Appl. Phys. Lett. **113**(6), 1–6 (2018).

2. E. Ahmadi, O.S. Koksaldi, S.W. Kaun, Y. Oshima, D.B. Short, U.K. Mishra, and J.S. Speck, "Ge doping of β-Ga2O3 films grown by plasma-assisted molecular beam epitaxy," Appl. Phys. Express **10**(4), 041102 (2017).

3. F. Alema, G. Seryogin, A. Osinsky, and A. Osinsky, "Ge doping of β-Ga2O3 by MOCVD," APL Materials **9**(9), 091102 (2021).

4. P. Ranga, A. Bhattacharyya, L. Whittaker-Brooks, M.A. Scarpulla, and S. Krishnamoorthy, "N-type doping of low-pressure chemical vapor deposition grown β-Ga2O3 thin films using solid-source germanium," J. Vac. Sci. Technol. A **39**(3), 030404 (2021).

5. K. Sasaki, A. Kuramata, T. Masui, E. G. Villora, K. Shimamura and S. Yamakoshi, "Device-Quality β-Ga2O3 Epitaxial Films Fabricated by Ozone Molecular Beam Epitaxy," Appl. Phys. Express **5**, 035502 (2012).

6. A. Mauze, Y. Zhang, T. Itoh, E. Ahmadi, and J.S. Speck, "Sn doping of (010) β-Ga2O3 films grown by plasma-assisted molecular beam epitaxy," Appl. Phys. Lett. **117**(22), 222102 (2020).

7. X. Du, Z. Li, C. Luan, W. Wang, M. Wang, X. Feng, H. Xiao, and J. Ma, "Preparation and characterization of Sn-doped β-Ga2O3 homoepitaxial films by MOCVD," J. Mater. Sci. **50**(8), 3252–3257 (2015).

8. S. Krishnamoorthy, Z. Xia, S. Bajaj, M. Brenner, and S. Rajan, "Delta-doped β-gallium oxide field-effect transistor," Appl. Phys. Express **10**(5), 051102 (2017).

9. Z. Feng, A.F.M. Anhar Uddin Bhuiyan, M.R. Karim, and H. Zhao, "MOCVD homoepitaxy of Si-doped (010) β-Ga2O3 thin films with superior transport properties," Appl. Phys. Lett. **114**, 250601 (2019).

10. K. Sasaki, M. Higashiwaki, A. Kuramata, T. Masui, and S. Yamakoshi, "Si-Ion Implantation Doping in β-Ga2O3 and Its Application to Fabrication of Low-Resistance Ohmic Contacts," Appl. Phys. Express **6**(8), 086502 (2013).

11. F. Alema, Y. Zhang, A. Osinsky, N. Valente, A. Mauze, T. Itoh, and J.S. Speck, "Low temperature electron mobility exceeding 104 cm2/V s in MOCVD grown β-Ga2O3," APL Materials **7**(12), 121110 (2019).

12. Y. Zhang, F. Alema, A. Mauze, O.S. Koksaldi, R. Miller, A. Osinsky, and J.S. Speck, "MOCVD grown epitaxial β-Ga2O3 thin film with an electron mobility of 176 cm2/V s at room temperature," APL Mater. **7**(2), 022506 (2019).

13. G. Seryogin, F. Alema, N. Valente, H. Fu, E. Steinbrunner, A.T. Neal, S. Mou, A. Fine, and A. Osinsky, "MOCVD growth of high purity Ga2O3 epitaxial films using trimethylgallium precursor," Appl. Phys. Lett. **117**(26), 262101 (2020).

14. F. Alema, Y. Zhang, A. Osinsky, N. Orishchin, N. Valente, A. Mauze, and J.S. Speck, "Low 1014 cm−3 free carrier concentration in epitaxial β-Ga2O3 grown by MOCVD," APL Materials **8**(2), 021110 (2020).

15. F. Alema, Y. Zhang, A. Mauze, T. Itoh, J.S. Speck, B. Hertog, and A. Osinsky, "H2O vapor assisted growth of beta-Ga2O3 by MOCVD," AIP Adv. **10**(8), (2020).

16. M.H. Wong, and M. Higashiwaki, "Vertical β-Ga$_2$O$_3$ Power Transistors: A Review," IEEE Trans. Electron Devices **67**(10), 3925–3937 (2020).

17. A.J. Green, J. Speck, G. Xing, P. Moens, F. Allerstam, K. Gumaelius, T. Neyer, A. Arias-Purdue, V. Mehrotra, A. Kuramata, K. Sasaki, S. Watanabe, K. Koshi, J. Blevins, O. Bierwagen, S. Krishnamoorthy, K. Leedy, A.R. Arehart, A.T. Neal, S. Mou, S.A. Ringel, A. Kumar, A. Sharma, K. Ghosh, U. Singisetti, W. Li, K. Chabak, K. Liddy, A. Islam, S. Rajan, S. Graham, S. Choi, Z. Cheng, and M. Higashiwaki, "β-Gallium oxide power electronics," APL Materials **10**(2), 029201 (2022).

18. S.-H. Han, A. Mauze, E. Ahmadi, T. Mates, Y. Oshima, and J.S. Speck, "n-type dopants in (001) β-Ga2O3 grown on (001) β-Ga2O3 substrates by plasma-assisted molecular beam epitaxy," Semicond. Sci. Technol. **33**(4), 045001 (2018).

19. M. Higashiwaki, K. Sasaki, A. Kuramata, T. Masui, and S. Yamakoshi, "Gallium oxide (Ga2O3) metal-semiconductor field-effect transistors on single-crystal β-Ga2O3 (010) substrates," Appl. Phys. Lett. **100**(1), 013504 (2012).

20. Y. Zhang, C. Joishi, Z. Xia, M. Brenner, S. Lodha, and S. Rajan, "Demonstration of β-(AlxGa1-x)2O3/Ga2O3 double heterostructure field effect transistors," Appl. Phys. Lett. **112**(23), 233503 (2018).

21. E. Farzana, F. Alema, W.Y. Ho, A. Mauze, T. Itoh, A. Osinsky, and J.S. Speck, "Vertical beta-Ga2O3 field plate Schottky barrier diode from metal-organic chemical vapor deposition," Appl. Phys. Lett. **118**(16), (2021).

22. N.K. Kalarickal, Z. Xia, J.F. McGlone, Y. Liu, W. Moore, A.R. Arehart, S.A. Ringel, and S. Rajan, "High electron density β-(Al0.17Ga0.83)2O3/Ga2O3 modulation doping using an ultra-thin (1 nm) spacer layer," J. Appl. Phys. **127**(21), 215706 (2020).

23. M.H. Wong, Y. Nakata, A. Kuramata, S. Yamakoshi, and M. Higashiwaki, "Enhancement-mode Ga2O3 MOSFETs with Si-ion-implanted source and drain," Appl. Phys. Express **10**(4), 041101 (2017).

24. M.H. Wong, K. Goto, H. Murakami, Y. Kumagai, and M. Higashiwaki, "Current Aperture Vertical β -Ga2O3 MOSFETs Fabricated by N- and Si-Ion Implantation Doping," IEEE Electron Device Lett. **40**(3), 431–434 (2019).

25. M.H. Wong, H. Murakami, Y. Kumagai, and M. Higashiwaki, "Enhancement-mode β - Ga2O3 current aperture vertical MOSFETs with N-ion-implanted blocker," IEEE Electron Device Lett. **41**(2), 296–299 (2020).

26. A. Nikolskaya, E. Okulich, D. Korolev, A. Stepanov, D. Nikolichev, A. Mikhaylov, D. Tetelbaum, A. Almaev, C.A. Bolzan, A. Buaczik, R. Giulian, P.L. Grande, A. Kumar, M. Kumar, and D. Gogova, "Ion implantation in β-Ga2O3: Physics and technology," J. Vac. Sci. Technol. A **39**(3), 030802 (2021).

27. A.F.M.A.U. Bhuiyan, Z. Feng, L. Meng, A. Fiedler, H.-L. Huang, A.T. Neal, E. Steinbrunner, S. Mou, J. Hwang, S. Rajan, and H. Zhao, "Si doping in MOCVD grown (010) β-(AlxGa1−x)2O3 thin films," J. Appl. Phys. **131**(14), 145301 (2022).

28. K. Goto, K. Konishi, H. Murakami, Y. Kumagai, B. Monemar, M. Higashiwaki, A. Kuramata, and S. Yamakoshi, "Halide vapor phase epitaxy of Si doped β-Ga2O3 and its electrical properties," Thin Solid Films **666**, 182–184 (2018).

29. K.D. Leedy, K.D. Chabak, V. Vasilyev, D.C. Look, J.J. Boeckl, J.L. Brown, S.E. Tetlak, A.J. Green, N.A. Moser, A. Crespo, D.B. Thomson, R.C. Fitch, J.P. McCandless, and G.H. Jessen, "Highly conductive homoepitaxial Si-doped Ga2O3 films on (010) β-Ga2O3 by pulsed laser deposition," Appl. Phys. Lett. **111**(1), 012103 (2017).

30. F. Alema, T. Itoh, S. Vogt, J.S. Speck, and A. Osinsky, "Highly conductive epitaxial β-Ga2O3 and β-(Al x Ga1−x)2O3 films by MOCVD," Jpn. J. Appl. Phys. **61**(10), 100903 (2022).

31. F. Alema, C. Peterson, A. Bhattacharyya, S. Roy, S. Krishnamoorthy, and A. Osinsky, "Low Resistance Ohmic Contact on Epitaxial MOVPE Grown β-Ga2O3 and β-(AlxGa1−x)2O3 Films," IEEE Electron Device Lett. **43**(10), 1649–1652 (2022).

32. N.K. Kalarickal, Z. Xia, J. McGlone, S. Krishnamoorthy, W. Moore, M. Brenner, A.R. Arehart, S.A. Ringel, and S. Rajan, "Mechanism of Si doping in plasma assisted MBE growth of β-Ga2O3," Appl. Phys. Lett. **115**(15), 152106 (2019).

33. J.P. McCandless, V. Protasenko, B.W. Morell, E. Steinbrunner, A.T. Neal, N. Tanen, Y. Cho, T.J. Asel, S. Mou, P. Vogt, H.G. Xing, and D. Jena, "Controlled Si doping of β-Ga2O3 by molecular beam epitaxy," Appl. Phys. Lett. **121**(7), 072108 (2022).

34. A. Ardenghi, O. Bierwagen, A. Falkenstein, G. Hoffmann, J. Lähnemann, M. Martin, and P. Mazzolini, "Toward controllable Si-doping in oxide molecular beam epitaxy using a solid SiO source: Application to β-Ga2O3," Appl. Phys. Lett. **121**(4), 042109 (2022).

35. Y. Oshima, E. Ahmadi, S. Kaun, F. Wu, and J.S. Speck, "Growth and etching characteristics of (001) β-Ga2O3 by plasma-assisted molecular beam epitaxy," Semicond. Sci. Technol. **33**(1), 015013 (2018).

36. P. Vogt, A. Mauze, F. Wu, B. Bonef, and J.S. Speck, "Metal-oxide catalyzed epitaxy (MOCATAXY): the example of the O plasma-assisted molecular beam epitaxy of β-(Al x Ga1− x)2O3/β-Ga2O3 heterostructures," Appl. Phys. Express **11**(11), 115503 (2018).

37. A. Mauze, Y. Zhang, T. Itoh, F. Wu, and J.S. Speck, "Metal oxide catalyzed epitaxy (MOCATAXY) of β-Ga2O3 films in various orientations grown by plasma-assisted molecular beam epitaxy," APL Materials **8**(2), 021104 (2020).

38. P. Mazzolini, A. Falkenstein, C. Wouters, R. Schewski, T. Markurt, Z. Galazka, M. Martin, M. Albrecht, and O. Bierwagen, "Substrate-orientation dependence of β -Ga2O3 (100), (010), (001), and (2¯01) homoepitaxy by indium-mediated metal-exchange catalyzed molecular beam epitaxy (MEXCAT-MBE)," APL Materials **8**(1), 011107 (2020).

39. P. Vogt, O. Brandt, H. Riechert, J. Lähnemann, and O. Bierwagen, "Metal-Exchange Catalysis in the Growth of Sesquioxides: Towards Heterostructures of Transparent Oxide Semiconductors," Phys. Rev. Lett. **119**(19), 196001 (2017).

40. P. Vogt, and O. Bierwagen, "Reaction kinetics and growth window for plasma-assisted molecular beam epitaxy of Ga2O3: Incorporation of Ga vs. Ga2O desorption," Appl. Phys. Lett. **108**(7), 072101 (2016).

41. T. Itoh, A. Mauze, Y. Zhang, and J.S. Speck, "Continuous Si doping in (010) and (001) β-Ga2O3 films by plasma-assisted molecular beam epitaxy," APL Materials **11**(4), (2023)
.
42. T.J. Asel, E. Steinbrunner, J. Hendricks, and A.T. Neal, "Reduction of unintentional Si doping in β - Ga 2 O 3 grown via plasma-assisted molecular beam epitaxy Reduction of unintentional Si doping in β -Ga 2 O 3 grown via plasma-assisted molecular beam epitaxy," J. Vac. Sci. Technol. A **043403**(May), 2–7 (2020).

43. D. Starodub, E.P. Gusev, E. Garfunkel, and T. Gustafsson, "Silicon oxide decomposition and desorption during the thermal oxidation of silicon," Surf. Rev. Lett. **06**(01), 45–52 (1999).

44. C. Gelain, A. Cassuto, and P. Le Goff, "Kinetics and mechanism of low-pressure, high-temperature oxidation of silicon-II," Oxid. Met. **3**(2), 139–151 (1971).

45. F. Afroz Faria, J. Guo, P. Zhao, G. Li, P. Kumar Kandaswamy, M. Wistey, H. (Grace) Xing, and D. Jena, "Ultra-low resistance ohmic contacts to GaN with high Si doping concentrations grown by molecular beam epitaxy," Appl. Phys. Lett. **101**(3), 032109 (2012).

46. Y. Oshima, E. Ahmadi, S.C. Badescu, F. Wu, and J.S. Speck, "Composition determination of β-(AlxGa1−x)2O3layers coherently grown on (010) β-Ga2O3substrates by high-resolution X-ray diffraction," Appl. Phys. Express **9**(6), 061102 (2016).

47. A. Azarov, C. Bazioti, V. Venkatachalapathy, P. Vajeeston, E. Monakhov, and A. Kuznetsov, "Disorder-Induced Ordering in Gallium Oxide Polymorphs," Phys. Rev. Lett. **128**(1), 015704 (2022).

48. A. Sardar, T. Isaacs-Smith, J. Lawson, T. Asel, R.B. Comes, J.N. Merrett, and S. Dhar, "High conductivity β-Ga2O3 formed by hot Si ion implantation," Appl. Phys. Lett. **121**(26), 262101 (2022).

49. J. Neugebauer, "Surfactants and antisurfactants on group-III-nitride surfaces," Phys. Status Solidi C **0**(6), 1651–1667 (2003).

50. A.L. Rosa, J. Neugebauer, J.E. Northrup, C.-D. Lee, and R.M. Feenstra, "Adsorption and incorporation of silicon at GaN(0001) surfaces," Appl. Phys. Lett. **80**(11), 2008–2010 (2002).

51. K. Hoshikawa, T. Kobayashi, E. Ohba, and T. Kobayashi, "50 mm diameter Sn-doped (001) β-Ga2O3 crystal growth using the vertical Bridgeman technique in ambient air," J. Cryst. Growth **546**, 125778 (2020).

52. A. Mauze, Y. Zhang, T. Itoh, T.E. Mates, H. Peelaers, C.G. de Walle, and J.S. Speck, "Mg doping and diffusion in (010) beta-Ga2O3 films grown by plasma-assisted molecular beam epitaxy," J. Appl. Phys. **130**(23), (2021).

IV. Pure ozone MBE

4.1. Introduction

β-Ga$_2$O$_3$ epitaxial films with outstanding crystal quality and transport properties has been realized by PAMBE. The exceptional results in the early stage of the β-Ga$_2$O$_3$ materials system have been achieved by MBE-grown epitaxial films. On the other hand, the background compensation level (N$_a$) has been limited by the residual impurities in the oxygen source cylinder. As mentioned in Chapter 1, the background impurity level is critical toward the performance of β-Ga$_2$O$_3$-based power electronics since low net charge concentration (N$_d$ − N$_a$) is necessary for high breakdown voltage. Moreover, β-Ga$_2$O$_3$ epitaxial films with low background compensation level have shown exceptional transport properties such as extremely high low temperature Hall mobilties[1–3]. Therefore, pursuing the ultimate purity of β-Ga$_2$O$_3$ epitaxial films can pave the way toward the application of β-Ga$_2$O$_3$ as high-performance power electronics with low on-resistance and high breakdown voltage. Identifying the impurities that are incorporated into the β-Ga$_2$O$_3$ epitaxial films grown by PAMBE is necessary and subsequently prevents the identified impurities from incorporating into the β-Ga$_2$O$_3$ epitaxial films during the growth.

4.2. Unintentional doping in PAMBE of β-Ga$_2$O$_3$

PAMBE utilizes pure oxygen gas tank with a purity of 5N: 99.9999% as source material to grow β-Ga$_2$O$_3$ epitaxial film. The oxygen gas is introduced into the RF plasma source so that a flux of active atomic oxygen (O) can be generated to react with the Ga atoms evaporated from effusion cell on the surface of the substrate. Here, about 1-2% of the oxygen gas is transformed to active atomic O, which is a primary active oxygen species that

can react with Ga atoms. However, the residual nitrogen gas with a concentration of ~ 1 ppm in the pure oxygen gas source is not negligible to the epitaxial growth by PAMBE because nitrogen can also be excited into active atomic nitrogen in a RF plasma source. The active atomic nitrogen is also reactive with Ga atoms on the surface of the substrate, which results in nitrogen incorporation during the growth of β-Ga_2O_3 epitaxial films by PAMBE. Previous studies have revealed that nitrogen incorporation into the β-Ga_2O_3 epitaxial film during the growth by PAMBE. The SIMS nitrogen concentration in the β-Ga_2O_3 epitaxial film exhibited oxygen flow rate dependence[4]. When the oxygen flow rate increases, the nitrogen concentration incorporated into the β-Ga_2O_3 epitaxial film decreases.

To identify the amount of nitrogen incorporated in the β-Ga_2O_3 epitaxial film, detailed secondary ion mass spectrometry (SIMS) was performed by sending samples to TORAY research center Inc.'s analysis group. While conventional SIMS facilities have higher detection limit for the measurement of nitrogen, TORAY research center's SIMS facility was optimized to measure nitrogen concentration with a detection limit of ~1.0×10^{15} /cm^3, which is two orders lower than conventional SIMS facility. SIMS-stack samples with different growth temperatures and Ga fluxes were prepared for investigation of nitrogen incorporation into β-Ga_2O_3 epitaxial films by SIMS. During the growth, the oxygen supply was fixed at a fore line pressure of 60 Torr with a background oxygen pressure at around 2.0×10^{-5} Torr in the MBE growth chamber. The structure of the SIMS stack samples with different growth conditions grown by MOCATAXY is shown in Fig. 4.1 (a). In addition, stacked samples grown by conventional MBE method were also prepared to compare the nitrogen incorporation into β-Ga_2O_3 epitaxial films. The growth rates of the MOCATAXY-grown sample and the conventional MBE were 5.0 nm/min and 2.5 nm/min, respectively.

The growth temperature of the MOCATAXY growth was 800 ℃, while the growth temperature of the conventional MBE growth was 700 ℃. Sn-doped layers with different Sn cell temperature from 700 ℃ to 850 ℃ were added to separate the UID layers to have clear identification of individual layers with different growth conditions. The UID layers are also used for the stabilization of the Sn effusion cell during the changing of the temperature set point. On the other hand ,the Ga flux was varied at either $2.5{\times}10^{-7}$ Torr or $2.8{\times}10^{-7}$ Torr during the whole growth sequence. The In flux was fixed at $4.0{\times}10^{-7}$ Torr for the MOCATAXY growth. This fixed indium flux is appropriate for MOCATAXY growth of β-Ga_2O_3 layers with outstanding crystal qualities at this Ga fluxes range. The surface morphology measured by AFM is shown in Fig 4.1 (b). An RMS roughness value of 0.24 nm indicates that the film is extremely smooth for the thickness of 1300 nm. Therefore, this SIMS-stack structure for nitrogen SIMS measurement has sufficient quality to perform as a standard of nitrogen level in the β-Ga_2O_3 films grown by PAMBE. The film thickness was estimated from the growth rate of all the β-Ga_2O_3 layers, and it was also confirmed by the SIMS results in the following figures.

SIMS-stack structure | Growth conditions

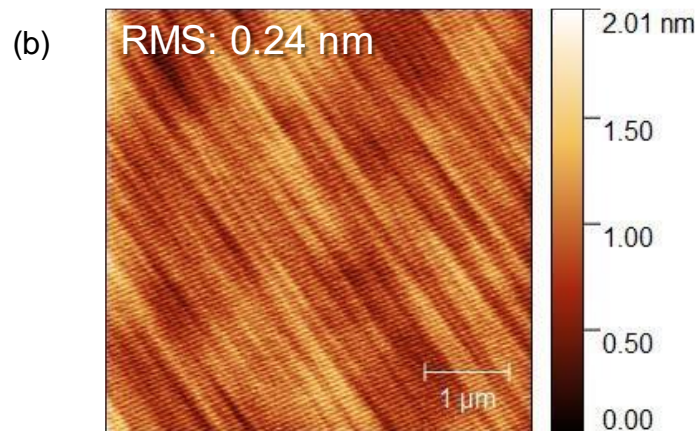| SIMS-stack structure	Growth conditions
Sn-doped β-Ga$_2$O$_3$ 200 nm	Tsub=800 ℃, Ga Flux: 2.5E-7 Torr (T$_{Ga}$:1050/1025℃) In Flux: 4E-7 Torr (T$_{In}$:745), **T$_{Sn}$:950/925℃**
UID β-Ga$_2$O$_3$ 100 nm	Tsub=800 ℃, Ga Flux: 2.5E-7 Torr (T$_{Ga}$:1050/1025℃) In Flux: 4E-7 Torr (T$_{In}$:745)
Sn-doped β-Ga$_2$O$_3$ 200 nm	Tsub=850 ℃, Ga Flux: 2.8E-7 Torr (T$_{Ga}$:1057/1032℃) In Flux: 4E-7 Torr (T$_{In}$:745), **T$_{Sn}$:950/925℃**
UID β-Ga$_2$O$_3$ 100 nm	Tsub=850 ℃, Ga Flux: 2.8E-7 Torr (T$_{Ga}$:1057/1032℃) In Flux: 4E-7 Torr (T$_{In}$:745)
Sn-doped β-Ga$_2$O$_3$ 200 nm	Tsub=700 ℃, Ga Flux: 2.8E-7 Torr (T$_{Ga}$:1057/1032℃) In Flux: 4E-7 Torr (T$_{In}$:745), **T$_{Sn}$:950/925℃**
UID β-Ga$_2$O$_3$ 100 nm	Tsub=700 ℃, Ga Flux: 2.8E-7 Torr (T$_{Ga}$:1057/1032℃) In Flux: 4E-7 Torr (T$_{In}$:745), **T$_{Sn}$:950/925℃**
Sn-doped β-Ga$_2$O$_3$ 200 nm	Tsub=800 ℃, Ga Flux: 2.8E-7 Torr(T$_{Ga}$:1057/1032℃) In Flux: 4E-7 Torr (T$_{In}$:745), **T$_{Sn}$:950/925℃**
UID β-Ga$_2$O$_3$ 200 nm	Tsub=800 ℃, Ga Flux: 2.8E-7 Torr(T$_{Ga}$:1057/1032℃) In Flux: 4E-7 Torr (T$_{In}$:745),
β-Ga$_2$O$_3$ substrate (Fe doped)	

(b)

Figure 4.1. (a) The growth structure of the SIMS-stack sample grown by MOCATAXY. The growth conditions including growth temperatures and effusion cell temperatures along with the BEPs are shown on the right of the SIMS-stack structure. (b) The surface morphology of this approximately 1300-nm-thick β-Ga$_2$O$_3$ epitaxial film measured by AFM with an RMS roughness of 0.24 nm.

The resulting nitrogen concentration in the β-Ga$_2$O$_3$ epitaxial film grown by MOCATAXY showed slight difference between the different growth conditions such as Ga fluxes, growth temperatures and Sn doping concentration in Fig. 4.2. The film thickness corresponds to the estimated thickness derived from the growth rate by MOCATAXY growth. A nitrogen concentration of approximately 1.0×10^{17} cm^{-3} is uniformly incorporated into the β-Ga$_2$O$_3$ epitaxial film. In the substrate, however, the nitrogen concentration is under the detection limit of SIMS. Therefore, the incorporated nitrogen can be determined to originate from the growth environment. On the other hand, while the Sn doping concentrations were varied from 3.0×10^{17} cm^{-3} to 3.0×10^{19} cm^{-3}, the nitrogen concentration at the Sn-doped regions didn't show a tendency to change with the changing Sn concentrations. While the substrate temperatures was changed from 700 °C to 850 °C during the growth, the nitrogen concentrations were not changed by the growth temperature. Additionally, the incorporated nitrogen concentration showed a slightly higher concentration at the interface between the substrate and the β-Ga$_2$O$_3$ epitaxial film, presumably due to a larger oxygen vacancy concentration at the initial stage of the growth and impurities from the atmosphere during the preparation of the sample[4].
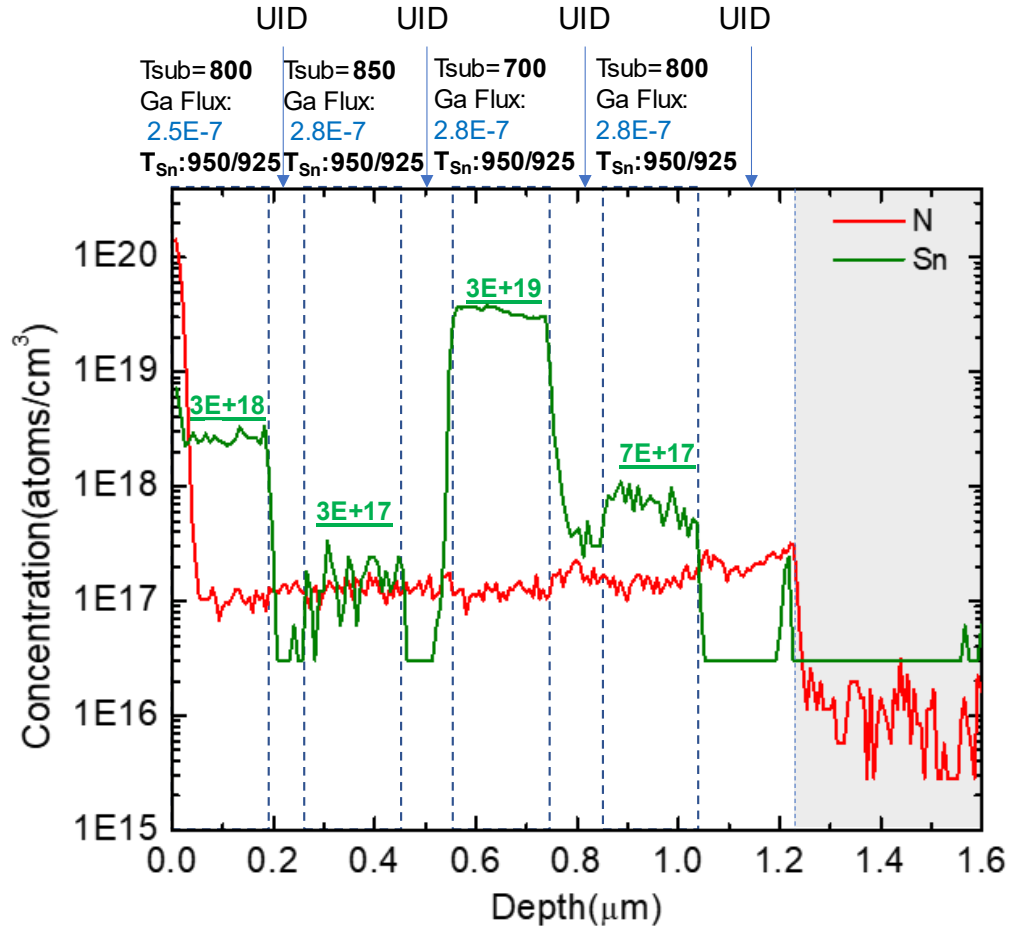
Figure 4.2. Nitrogen and Sn SIMS profile of the sample grown by MOCATAXY. The detection limit of nitrogen is around 1.0×10^{15} cm^{-3}.

While the growth conditions of β-Ga$_2$O$_3$ epitaxial film can affect the nitrogen incorporation, the difference between conventional growth and MOCATAXY growth should also be investigated to reveal the mechanism of unintentional nitrogen incorporation. A β-Ga$_2$O$_3$ epitaxial film with similar growth structure with approximately same thickness as the previous sample shown in Fig. 4.2 was prepared for SIMS measurement.
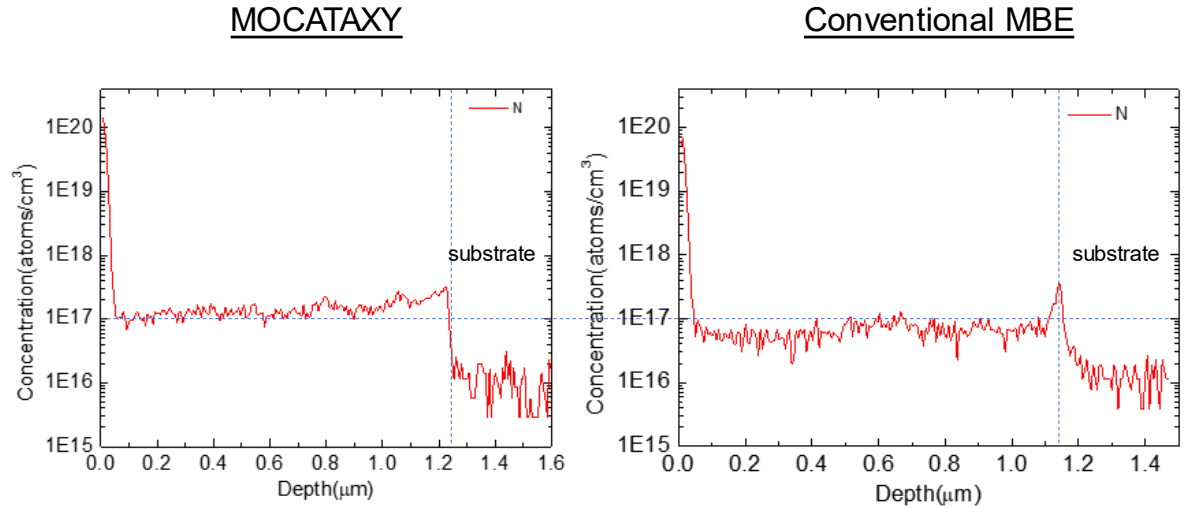
MOCATAXY   Conventional MBE

Figure 4.3. Nitrogen SIMS concentration in ~ 1 μm thick β-Ga$_2$O$_3$ epitaxial films grown by MOCATAXY and conventional MBE growth.

The results of nitrogen SIMS show that the nitrogen concentration in β-Ga$_2$O$_3$ epitaxial film grown by MOCATAXY is ~1.0×10^{17} /cm^3 and differs upon growth temperatures and Ga fluxes. The nitrogen SIMS results of both conventional growth and MOCATAXY growth are shown in Fig 4.3. The nitrogen concentration in the MOCATAXY method grown film is slightly higher than that of conventional method grown film. The growth rate for MOCATAXY method is around 5.0 nm/min while that of the conventional film is approximately 2.5 nm/min. The larger nitrogen incorporation into MOCATAXY method grown film can be attributed to the degree of nitrogen incorporation has been proved to depend on oxygen vacancies[4], while the higher growth rate of MOCATAXY may result in more oxygen vacancies as the amount of active oxygen adatoms is constant during the growth. The pure oxygen gas tank was changed to a new tank with lower N concentration measured by the manufacturer.
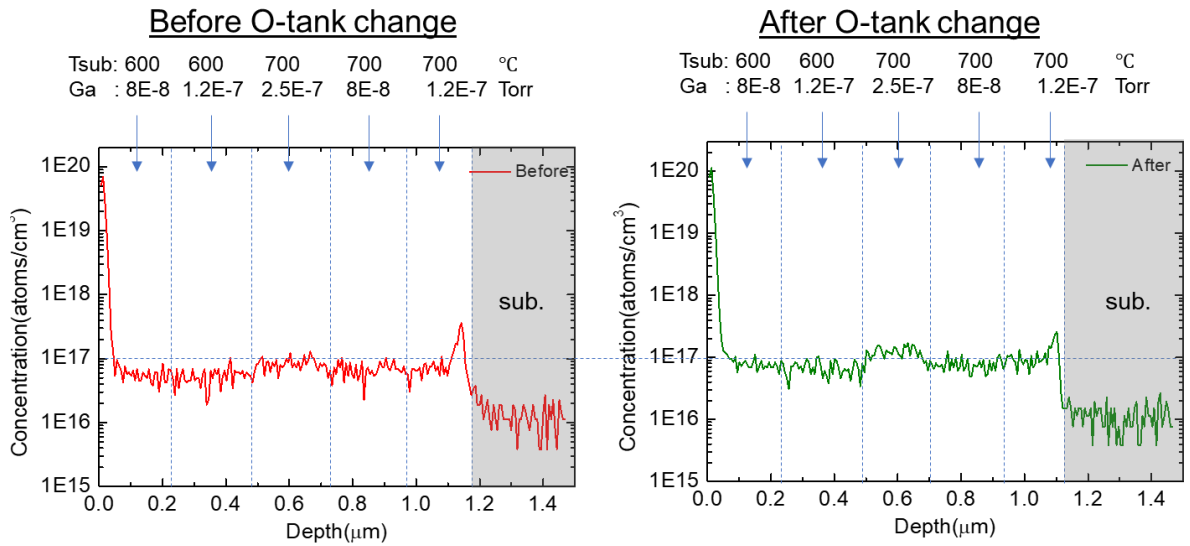
Conventional growth

Before O-tank change

After O-tank change

Figure 4.4. Nitrogen SIMS results on PAMBE-grown β-Ga$_2$O$_3$ films for before the oxygen tank change ([N] = 0.840 ppm) and after the oxygen tank change ([N] = 0.294 ppm).

On the other hand, the nitrogen concentration in β-Ga$_2$O$_3$ epitaxial film did not change in spite of changing an oxygen tank with lower nitrogen level measured by the manufacturer as shown in Fig. 4.4. After carefully investigating the residual nitrogen level in the oxygen tanks, the results show that the old oxygen tank had a nitrogen concentration of 0.840 ppm and the new oxygen tank had 0.294 ppm. The nitrogen concentration was only reduced to approximately 1/2 by changing to a newer oxygen tank. This change was not enough to achieve an obvious reduction of nitrogen incorporation into β-Ga$_2$O$_3$ epitaxial films. To eliminate the nitrogen incorporation into β-Ga$_2$O$_3$ epitaxial film, replacement of RF plasma source is necessary for the homoepitaxial growth of ultra-pure material in order to realize high-performance electronics devices. Moreover, investigation of MOCVD-grown β-Ga$_2$O$_3$ epitaxial film with superior electron mobility revealed that the nitrogen concentration was

lower than the detection limit, which suggested that nitrogen affects the electronic properties

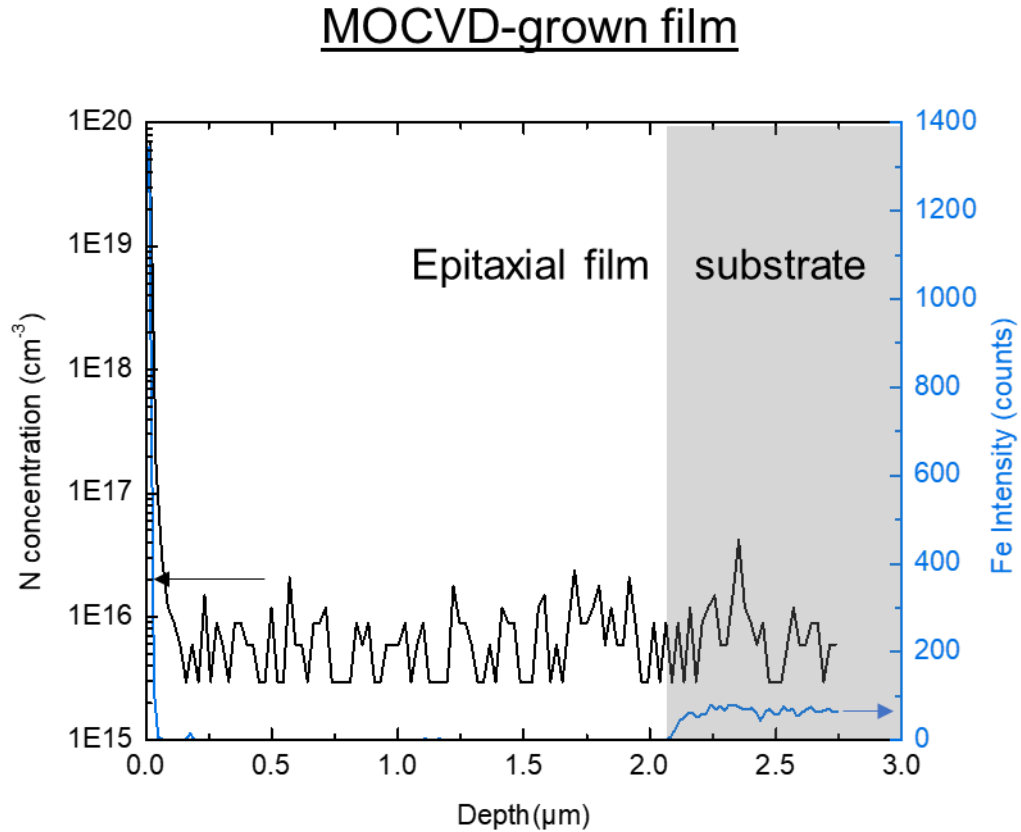of β-Ga_2O_3 epitaxial film.

MOCVD-grown film

Figure 4.5. Nitrogen SIMS profile of a MOCVD-grown film with record transport properties. The Fe profile is used to distinguish the interface between the substrate and epitaxial film.

Nitrogen has been identified as a deep acceptor in β-Ga_2O_3 system and used to make the film semi-insulating or guard-ring in a MOSFET by ion implantation[5,6]. To achieve β-Ga_2O_3 epitaxial film with high purity and superior electronic properties, it is inevitable to remove residual nitrogen gas in the oxygen source. One of the methods to prevent nitrogen atom from incorporating into β-Ga_2O_3 epitaxial film is to use pure ozone generator instead of RF

91

plasma source. This can both avoid generating active atomic nitrogen by plasma and use 100% pure ozone as oxygen source without nitrogen gas contamination as residual gas.
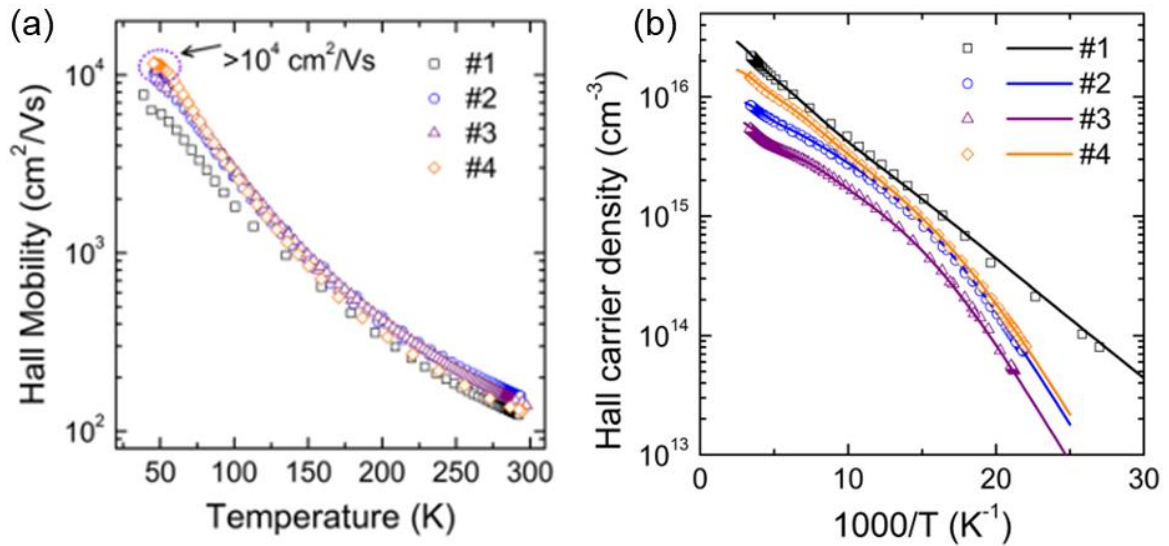

Figure 4.6. (a) Record low-temperature Hall mobility and (b) carrier density result of the MOCVD-grown β-Ga$_2$O$_3$ film measured by SIMS in the previous figure[2].

Figure 4.6 shows the low-temperature Hall mobilities and carrier densities of the MOCVD-grown β-Ga$_2$O$_3$ films. The Hall mobility of this β-Ga$_2$O$_3$ epitaxial film reached above 10^4 cm^2/Vs, which is comparable to those of GaN and SiC. Moreover, by fitting the results of Hall mobility, the value of N_a was derived to be as low as 8×10^{14} cm^{-3}. This extremely low value of N_a corresponds to the SIMS results in Fig. 4.5 that showed a nitrogen concentration under the detection limit. Therefore, the key to the improvement of the transport properties of β-Ga$_2$O$_3$ films is to prevent impurities such as nitrogen from incorporating into the film during the growth. Since PAMBE-grown β-Ga$_2$O$_3$ has nitrogen incorporation due to the residual nitrogen in the oxygen gas source, alternative growth

method without using plasma to generate active atomic oxygen is necessary for the growth of β-Ga$_2$O$_3$ epitaxial film with high purity to realize superior transport properties.

Homoepitaxial growth of β-Ga$_2$O$_3$ by ozone-enhanced MBE has been investigated on various substrate orientations[7]. Here, the ozone source is a gas mixture consisting of ozone (5%) and oxygen (95%) because the concentration of ozone is limited by the generation rate of the ozone generator. Since oxygen gas is not reactive with Ga atoms, the growth rate and crystal quality are mostly determined by the amount of supplied ozone gas species. A pure ozone generator has recently been developed to realize 100% ozone generation with minimum nitrogen level. Falson *et al.* reported transport properties of a two-dimensional electron gas (2DEG) of MgZnO/ZnO heterostructures with electron mobility exceeding 1.0×10^6 cm^2/Vs at around 100 mK grown by MBE using pure ozone as oxygen source[8]. This extremely high electron mobility was achieved by the improved crystallinity with reduced impurity levels due to the usage of pure ozone as oxygen source. Moreover, this mobility is higher than the record the 2DEG of AlGaN/GaN heterostructure, which was 167,000 cm^2/Vs at 300 mK achieved by Manfra *et al*[9]. Therefore, it is essential to reduce the impurity levels such as nitrogen to improve the crystallinity of β-Ga$_2$O$_3$ epitaxial film. The potential of β-Ga$_2$O$_3$ with availability of high-quality bulk substrates may be fully explored by utilizing pure ozone MBE as growth method.

4.3 Oxide MBE system

To realize the growth of β-Ga$_2$O$_3$ epitaxial film with low impurities level, a new Scienta Omicron EVO 50 oxide MBE system was introduced. This system is a vertical MBE system with a background pressure in the main growth chamber up to 1.0×10^{-10} mBar. The new

MBE system is targeted to provide ultra-high-purity β-Ga$_2$O$_3$ epitaxial films without a history of growing other materials. To assemble the system from separated components, which is shown in Fig. 4.7, every step should be taken with exceptional caution to avoid any contamination to the MBE system. Two main parts were shipped to assemble this system, one is the main growth chamber, the other is the intro chamber and the buffer chamber that are already connected to each other. The buffer chamber and the main growth chamber were sealed by blank flanges on the connecting ports. After removing the blank flanges, and quickly connecting the two ports on both sides with a gasket to complete the connection between the buffer chamber and the main growth chamber. A detailed leak check by He gas was performed on every connection on the MBE system after all the pumps, including scroll pumps and turbo pumps are in normal operation model.

Among the three chambers, the intro chamber is the only chamber that can be open to the atmosphere for loading/unloading samples. Due to its relatively small volume, it can be pumped faster than the other two chambers, with a pressure down to 1.0×10^{-7} mBar within 30 minutes after starting the turbo pump. It was equipped with a lamp heater to bake off most of the water from the newly loaded samples. However, since the lamp heater cannot evenly heat the samples on the stage due to its sided location, this baking step can be skipped until further baking in the buffer chamber. The buffer chamber is kept at the pressure of 1.0×10^{-10} mBar range. When the pressure difference between the intro chamber and buffer chamber is less than two or three orders of magnitude, the gate valve between these two chambers can be open to transfer new samples to the stage in the buffer chamber. This process does not affect the vacuum pressure in the buffer chamber after closing the gate valve. The buffer chamber is equipped with a bake station that bakes off water and other

impurities. During this process, the pressure first surges up to the 1.0×10^{-6} mBar range due to the vaporization of the water on the newly loaded sample. The pressure quickly fell back to the 1.0×10^{-8} mBar range after the water was depleted from the sample. After two hours of this baking process, the pressure in the buffer chamber stabilized at around 1.0×10^{-9} mBar range, and it will resume to the normal idling pressure when the baking temperature is back to the room temperature. The sample can then be transferred from the buffer chamber to the main growth chamber after this pre-growth baking process by opening the gate valve between the buffer chamber and the main growth chamber. In the main chamber, the sample temperature can be raised higher for pre-growth baking and epitaxial growth.
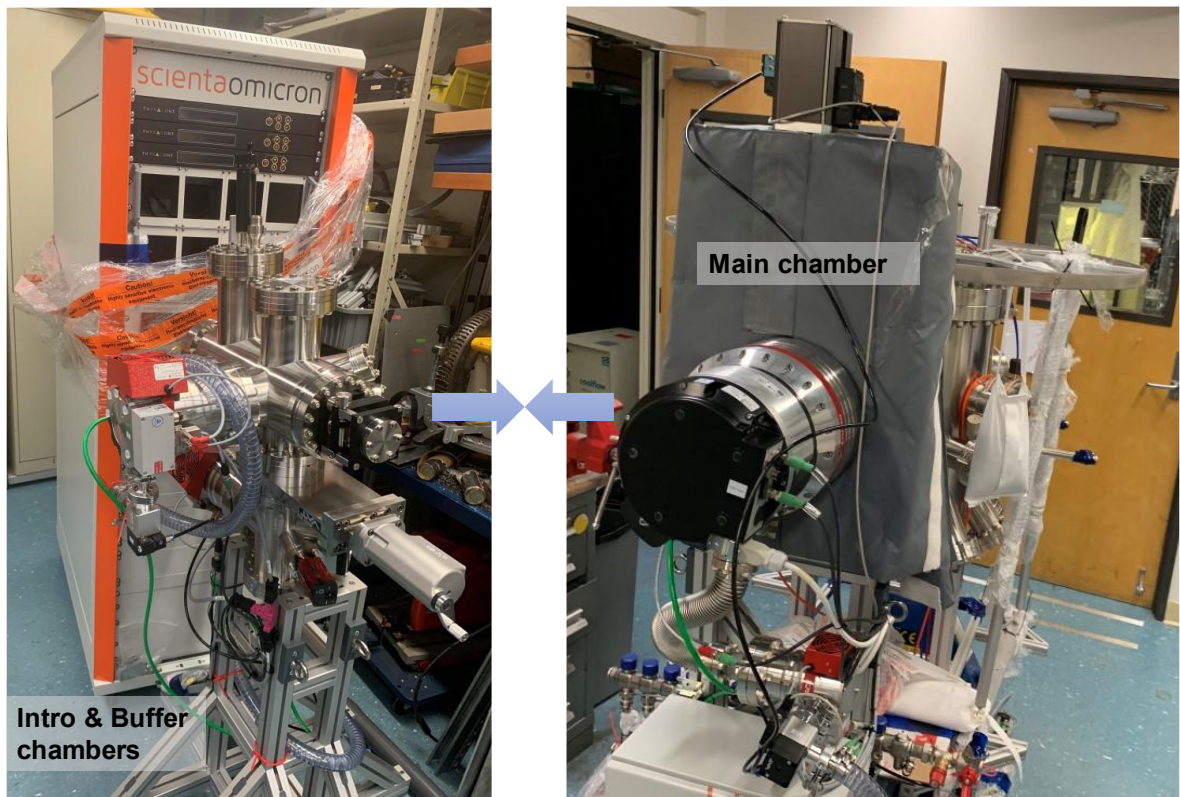

Figure 4.7. Individual components of a new MBE system including the intro, buffer and main chambers. The components were connected to each other for full MBE operation.
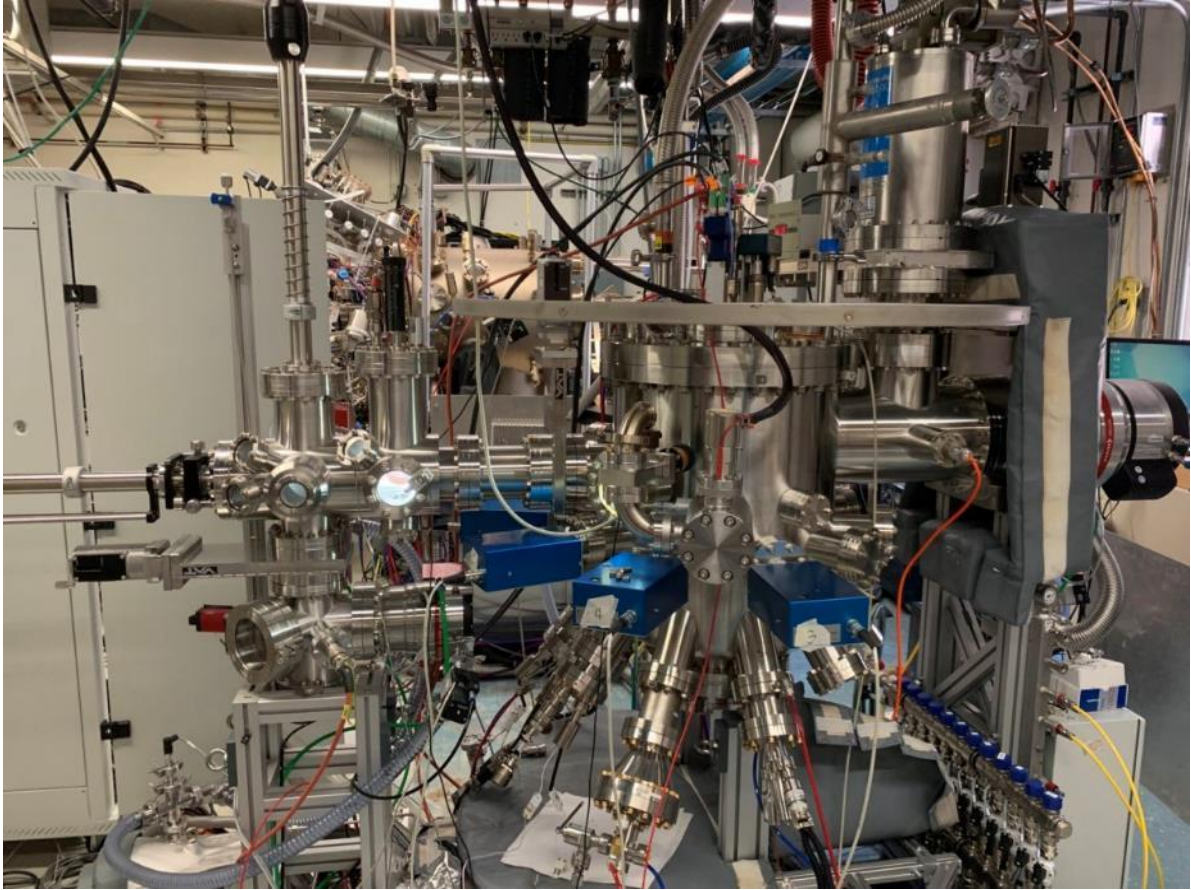
Figure 4.8. The completed MBE system and all components including effusion cells and plasma unit attached to the main chamber.

4.4 Effusion cells and oxygen supply

The elemental metal fluxes are provided from the effusion cells filled with high-purity metal sources, as mentioned in Chapter 1. Group III elemental source materials are always kept in liquid phase by maintaining the cell temperature above their melting points. The supplying metal beam fluxes can be varied by adjusting the cell temperatures and monitored by the beam flux gauge. To obtain a perspective for the calibration of growth conditions for β-Ga$_2$O$_3$ epitaxial films, the new MBE system needs to establish growth conditions based on the previous MBE system's results. However, due to the difference of designs and

geometries between the new MBE system and the previous MBE system, the parameters used for the growth conditions need to be transformed to fit the new system. Since the measured elemental beam fluxes such as Ga flux depends on the position of the beam flux monitor and the distance between the cell and monitor, the BEPs acquired in the previous system cannot be directly applied to the new system for growth studies. Therefore, a universal parameter that is independent of the design of MBE systems is required to transform the growth conditions. Here, instead of using BEPs in the unit of Torr or mbar, the Ga flux can be derived from the number of atoms reaching the surface of the samples per second per area, which can be expressed as atoms/nm^2/s. To calculate this parameter, the dimensions of β-Ga$_2$O$_3$ unit cell and monolayers are shown in Fig. 4.9.
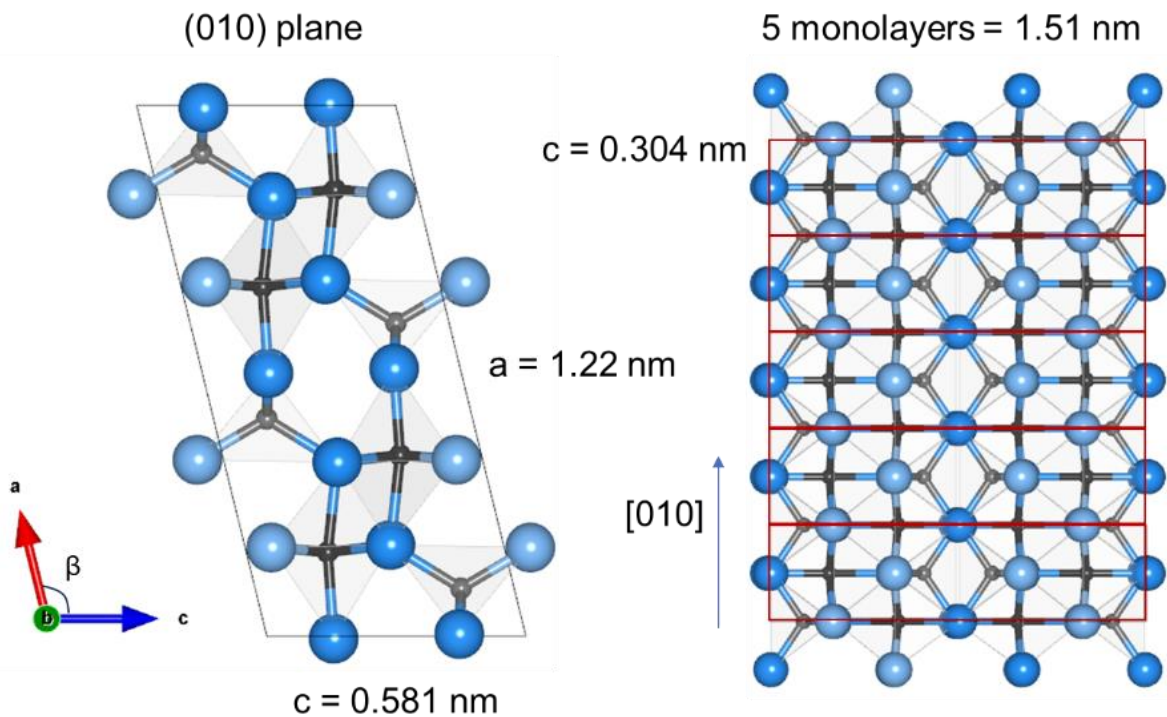

Figure 4.9. The unit cell of β-Ga$_2$O$_3$ projected from the b [010] direction and the cross-section view of the monolayers grown on the (010) substrate.

In a β-Ga$_2$O$_3$ unit cell, there are eight Ga atoms. Four of the Ga atoms are in the tetrahedral sites and the other four are in the octahedral sites. When one monolayer (ML) of β-Ga$_2$O$_3$ is epitaxially grown on the surface of the substrate, the atomic density can be calculated by the following equation,

$$\frac{8 \ Ga \ atoms/ML}{0.581 \ nm \ \times 1.22 \ nm} = 11.29 \ atoms/ML/nm^2$$

Next, the growth rate of β-Ga$_2$O$_3$ epitaxial films can be applied to this equation to get the universal Ga flux. From a growth rate that is in the oxygen-rich regime, which means there is no excessive Ga to etch the β-Ga$_2$O$_3$ epitaxial films to cause reduction in growth rate, the universal flux can be calculated. It should be noted that the growth rates of β-Ga$_2$O$_3$ epitaxial films also depend on the substrate temperature and oxygen background pressure, which is shown in Chapter 2. Here, when the growth rate with a measured BEP Ga flux of 1.5×10^{-7} Torr in the previous MBE system at the stoichiometric point is 3 nm/min, which was obtained from fitting thickness fringes of HRXRD results, then the number of monolayers that is grown in one second is,

$$\frac{3.0 \ nm/min}{0.304 \ nm/ML \times 60 \ s/min} = \ 0.0164 \ ML/s$$

Therefore, the universal Ga flux in the previous MBE system can be calculated form the above equations,

$$11.29 \ atoms/ML/nm^2 \times 0.164 \ ML/s = 1.86 \ atoms/nm^2/s$$

Consequently, the BEP Ga flux in the previous MBE system is transformed to a universal Ga flux based on the Ga atoms deposited on the surface of the sample per area per time. Here, a BEP Ga flux of 1.5×10^{-7} Torr in the previous is equivalent to 1.86 atoms/nm^2/s. For a similar substrate temperature and oxygen background pressure, the universal Ga flux

that is independent of MBE systems can be applied to the new MBE system as a starting point for the initial growth calibration studies.

For the initial growth rate calibration of β-Ga_2O_3 epitaxial films, the growth rates dependence on the Ga fluxes are shown in Fig. 4.10. The oxygen flow rates used in the growths were determined by the resulting main chamber background pressure in the previous system, which is approximately 2.0×10^{-5} Torr. In addition, the growth rates were determined by fitting the thickness fringes of HRXRD results.
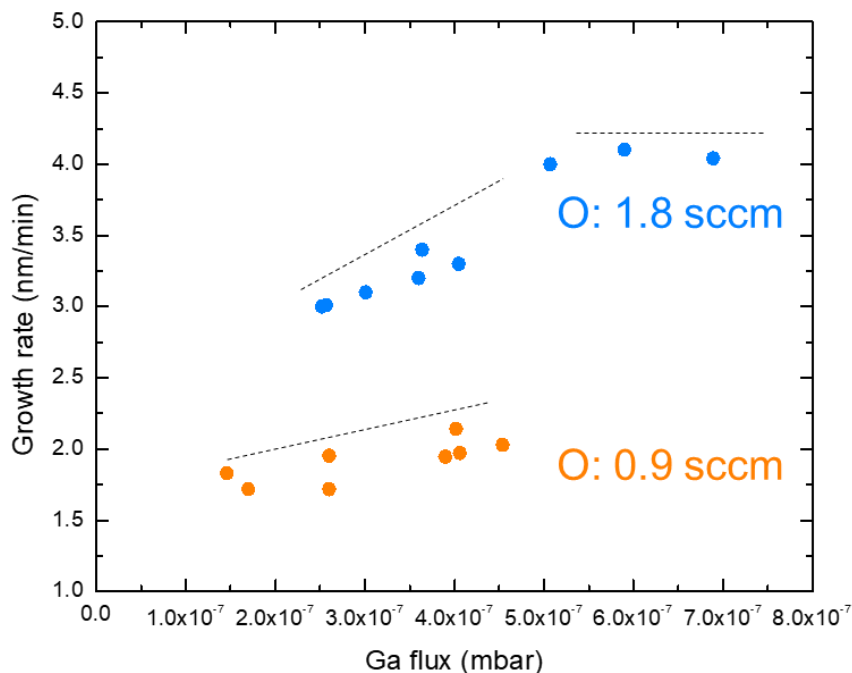

Figure 4.10. The growth rates dependence on the Ga fluxes at different oxygen flow rates with a substrate temperature of 700 °C by PAMBE. The growth rates at an oxygen flow rate of 0.9 sccm is shown in yellow and oxygen flow rate of 1.8 sccm is shown in blue.

When the oxygen flow rate is at 0.9 sccm, the growth rates of β-Ga_2O_3 epitaxial films increase linear as the Ga fluxes increase. The slope of the trendline is steeper at an oxygen

flow rate of 1.8 sccm than those of 0.9 sccm, which is presumably due to the higher active atomic oxygen existence around the sample at a higher oxygen flow rate. The growth rates at the oxygen flow rate of 1.8 sccm are approximately twice higher than those of the oxygen flow rates of 0.9 sccm, which is also revealed in the following paragraph illustrating the oxygen flow rate depending on the growth rates. The surface morphologies of β-Ga_2O_3 epitaxial films were measured by AFM to optimize the growth conditions with smooth surface morphology.
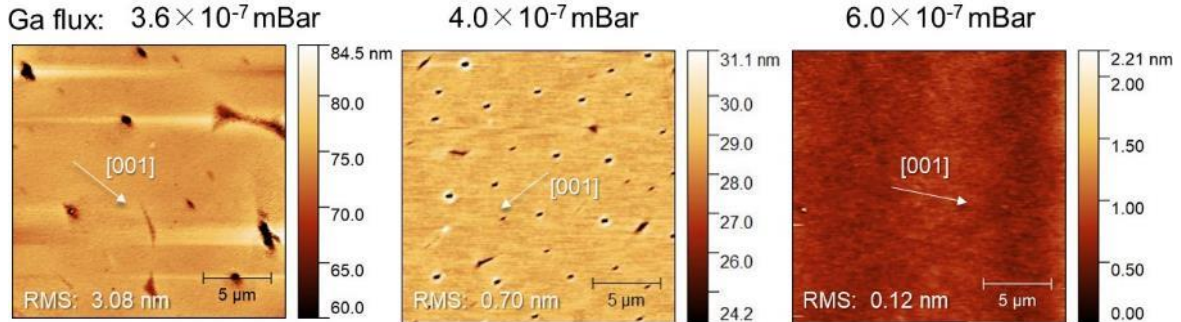

Figure 4.11. AFM images of PAMBE-grown β-Ga_2O_3 epitaxial films grown at different Ga fluxes at a substrate temperature of 700 °C and the oxygen flow rate of 1.8 sccm.

The surface morphologies of β-Ga_2O_3 epitaxial films grown at different Ga fluxes with a substrate temperature of 700 °C and oxygen flow rate of 1.8 sccm are shown in Fig. 4.11. The resulting MBE main chamber pressure is approximately 5.0×10^{-5} mBar, which is equivalent to 3.75×10^{-5} Torr. When the Ga fluxes are under 6.0×10^{-7} mBar, pits show on the surface of β-Ga_2O_3 epitaxial films due to insufficient Ga supply during the growth. On the other hand, the surface of the β-Ga_2O_3 epitaxial film grown with a Ga flux of 6.0×10^{-7} mBar exhibited extremely smooth surface morphology with no pits and a value of RMS roughness

of as low as 0.12 nm. This result corresponds to the growth rates dependence on Ga flux in Fig. 4.10 that shows the Ga fluxes under 6.0×10^{-7} mBar is in the oxygen-rich regime, and at the approximate stoichiometric point shows the extremely smooth surface morphology.

The growth rate dependence on the oxygen flow rate is shown in Fig. 4.12. For this study, the Ga flux was fixed at 3.6×10^{-7} mBar and the substrate temperature were fixed at 700 °C. Also, the plasma power was fixed at 200 W. The growth rates of β-Ga_2O_3 epitaxial films increased as the oxygen glow rate increased. Since the maximum flow rate of the MFC was 3.0 sccm, the investigation was limited to oxygen flow rates under 3.0 sccm. However, if the oxygen flow rate can be further increased, the growth diagram can reach the maximum growth rate, which is the stoichiometric point at this fixed Ga flux of 3.6×10^{-7} mBar.
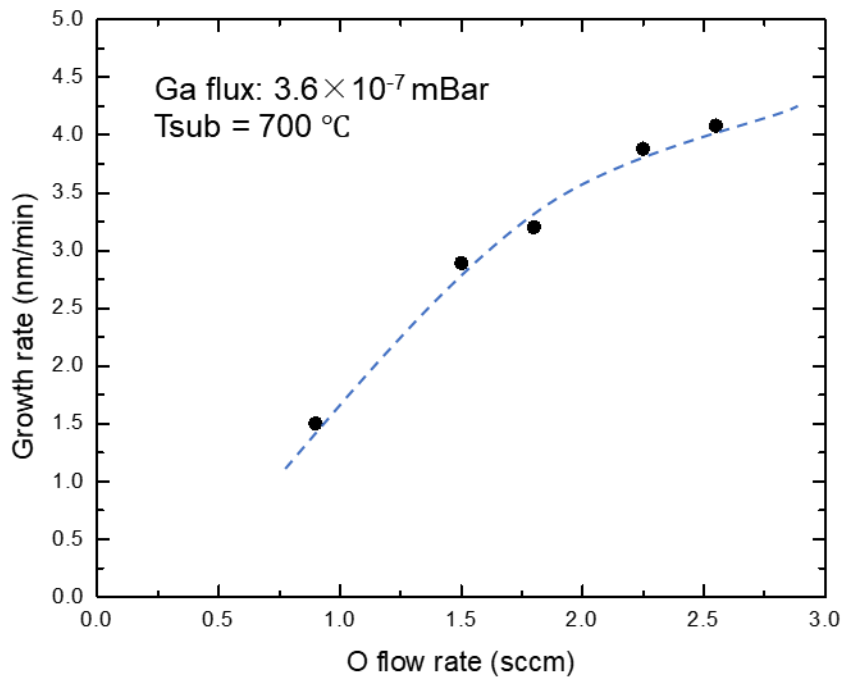

Figure 4.12. The growth rate dependence on oxygen flow rates at a fixed Ga flux of 3.6×10^{-7} mBar and a substrate temperature of 700 °C by PAMBE.

Despite the fixed Ga flux during the growth, the increasing growth rates of β-Ga$_2$O$_3$ epitaxial films at the oxygen-rich regime indicates that the higher oxygen background pressure and active oxygen atom can help suppress the desorption from the substrate. The increased high oxygen flow rate can improve the growth rate of β-Ga$_2$O$_3$ epitaxial films, and further growth studies can be conducted at the higher oxygen flow rates to obtain a comprehensive growth diagram.

The supply of oxygen source for the epitaxial growth of β-Ga$_2$O$_3$ is controlled by a Brooks 5800 series mass flow controller (MFC) which is modified for controlling O$_2$. The flow rate can be varied from 0.0 sccm to 3.0 sccm along with the fully open and fully closed mode. The oxygen gas pipe is further connected to the Vecco Unibulb RF plasma unit before entering the main growth chamber. Before the RF plasma unit, a manual gas valve was equipped to either completely shut the gas flow from the oxygen supply or allow the gas go into the plasma unit. The first step of the starting of the oxygen supply is to open the gas valves from the oxygen tank to the MFC when it is fully closed. After the gas flow stabilizes inside the whole gas piping, change the MFC to the normal mode: controlling the flow rate that goes through the MFC. Use a minimum flow rate of 0.10 sccm for the introduction of oxygen into the main growth chamber to avoid sudden pressure surge. When the reading of process value (PV) is stabilized at the value of the set point: 0.1 sccm, slowly open the gas valve before the RF plasma unit to introduce oxygen into the main growth chamber. Monitor the pressure in the main growth chamber to make sure there is no pressure surge during this introduction of sample process. To provide active oxygen gas species into the MBE chamber, the plasma unit was used to generate atomic oxygen to react with Ga flux on the

sample stage. The plasma was ignited and controlled by a MKS RF matching network controller, and its power was sullied from a power unit with an output of 200 W.
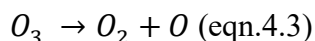
4.5. Pure ozone generator

The generation of pure ozone utilizes the difference of boiling points between oxygen and ozone. The boiling points for oxygen and ozone are 90.19 K and 161.2 K, respectively. While conventional ozone generator relies on the ozone discharger to produce ozone from oxygen gas, pure ozone generator further introduces a process that condensates the generated ozone/oxygen gas mixture to improve the ozone concentration. As a result, this condensation process significantly increases the concentration of ozone in the vessel.

In the atmosphere, the concentration of ozone is approximately 0.00006%[10]. Compared to the 21% concentration of oxygen in the atmosphere, the small amount of existing ozone is due to the rapid decomposition of ozone to oxygen in room temperature and atmosphere pressure. The generation of ozone includes two reactions: one is the break of the bonds between two oxygen atoms, the next one is the combination of atomic oxygen and oxygen molecule to form ozone.

$$O_2 \rightarrow 2O \text{ (eqn.4.1)}$$

$$O_2 + O \rightarrow O_3 \text{ (eqn.4.2)}$$
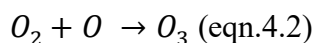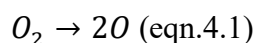
On the other hand, the decomposition of ozone is the reverse reaction,

$$O_3 \rightarrow O_2 + O \text{ (eqn.4.3)}$$

The schematic of ozone generation in the discharger is shown in Fig. 4.13. A pure oxygen gas source with a purity of 5N:99.999% is supplied to the ozone discharger. By applying high voltage up to 20 kV, corona discharge to generate atomic oxygen to react with

103

oxygen molecules, which results in ozone molecules. Due to the recombination of atomic oxygen, the yielding gas is the mixture of oxygen and ozone with ozone concentration to be around 5 wt% to 20 wt%.
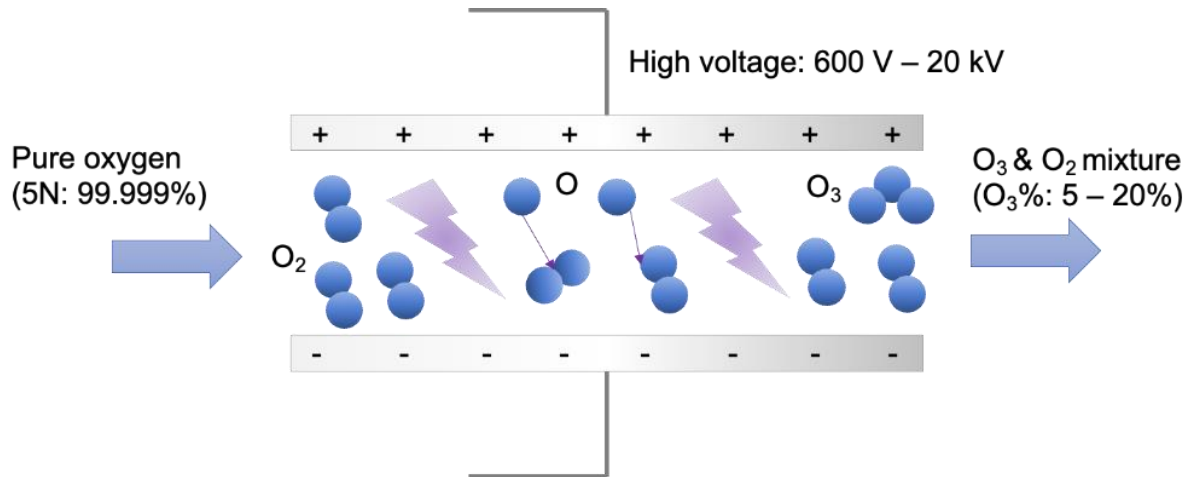

Figure 4.13. Ozone generated from pure oxygen gas by high-voltage corona discharge at a voltage of 600 V to 20 kV. The concentration by weight of generated ozone is usually 5 wt% to 20 wt%.

The source for generation of ozone can be either dry air or pure oxygen. Dry air contains too many contaminations such as nitrogen, CO_2 and other inert gases, and the generated ozone concentration is limited to less than 3 %. Therefore, using pure oxygen gas for generating oxygen is the most promising approach for its application to MBE growth. However, oxygen gas with ultra-high purity is not necessarily providing efficient ozone generation during the discharging process. This phenomenon is called the "ozone-zero" issue[11], which shows that the efficiency of ozone generation significantly declines right after the generation of ozone by high-purity oxygen gas[12]. Therefore, the source oxygen for the generation of pure ozone needs to be a mixture of gaseous oxygen and NO_x or Ar to

improve the efficiency of ozone generation. Since the primary objective of pure ozone for MBE growth is to remove nitrogen from the oxygen source to prevent nitrogen incorporation into β-Ga_2O_3 films. Therefore, the purity of the ozone source can be 99.5% with a mixture of 0.5% Ar for ozone generation to grow oxide semiconductor materials by MBE[13].

4.5. Purification of ozone/oxygen gas mixture

Pure ozone can be generated by either varying the temperature or the pressure of the vessel for accumulating liquid ozone. The temperature control of the vessel can be as accurate as 0.1 K and the temperature fluctuation can be less than 0.1 K during operation. The distilling of ozone is enabled by the difference of vapor pressures between oxygen and ozone. At 90 K, which is the boiling point of oxygen, the vapor pressure of oxygen is approximately four orders of magnitude larger than that of ozone in mbar. Figure 4.14 illustrates the boiling points of oxygen and ozone and their phases at different temperatures. When the temperature of the vessel is kept at 90.0 K, the majority of the mixture of ozone and oxygen are both in the liquid phase. Since the boiling point of oxygen is 90.19 K, most of the liquid oxygen vaporizes into gas phase while ozone stays in the liquid phase as the temperature of the vessel is raised to above 100 K. Pumping the vessel by a dry pump at this temperature range can purify the liquid oxygen due to the ventilation of gaseous oxygen. The effort of using pure ozone for MBE growth has begun in the early 1990's[13,14]. The fundamentals of generating pure ozone, however, have remained the same for years. On the other hand, the development and application of pure ozone has limited due to the dangers of store pure ozone since gaseous ozone is explosive at certain conditions[15]. The control of

temperature and pressure of the ozone container is the key towards the safety of operation. The vessel made of stainless steel provides stability of ozone storing since it is not reactive with gas or liquid ozone. Precise temperature management with an accuracy up to 0.1 K and PID is necessary for the stable pressure control inside the vessel.
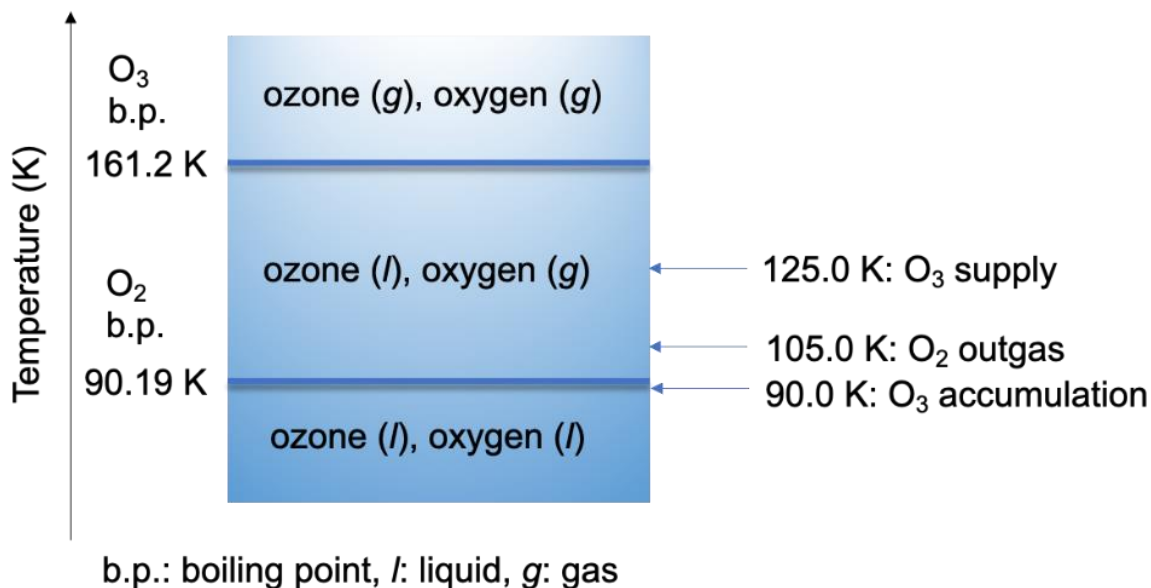

Figure 4.14. Phases of oxygen and ozone at different temperatures and the operation temperatures of the pure ozone generator.

The impurities in the oxygen gas cylinder can react with oxygen during the corona discharge in the ozone generator. In particular, the residual nitrogen in the oxygen cylinder can generate NO_x gas species by corona discharge, including N_2O, NO and NO_2. Figure 4.15 shows the vapor pressures of ozone, oxygen and other gas species that possibly co-exist in the ozone/oxygen gas mixture or liquid mixture. Moreover, the vapor pressures of nitrous oxide: N_2O and nitrogen dioxide: NO_2 in this temperature range are much lower than that of ozone, which indicates that NO_x can be removed from the pure ozone gas by purifying the

liquid ozone to achieve NO_x-free supply of gaseous ozone. Nitric oxide: NO, has higher vapor pressure than ozone in the whole range of the operation temperatures, which indicates that nitric oxide can be pumped out from the vessel during the ozone purification process at 105.0 K. Since nitrogen is a deep acceptor in the β-Ga_2O_3 materials system[5,16], NO_x-free pure ozone can achieve the growth of β-Ga_2O_3 epitaxial films with ultra-high purity. CO_2 is also a major residual gas species in the oxygen gas cylinder with a typical concentration of <0.5 ppm.
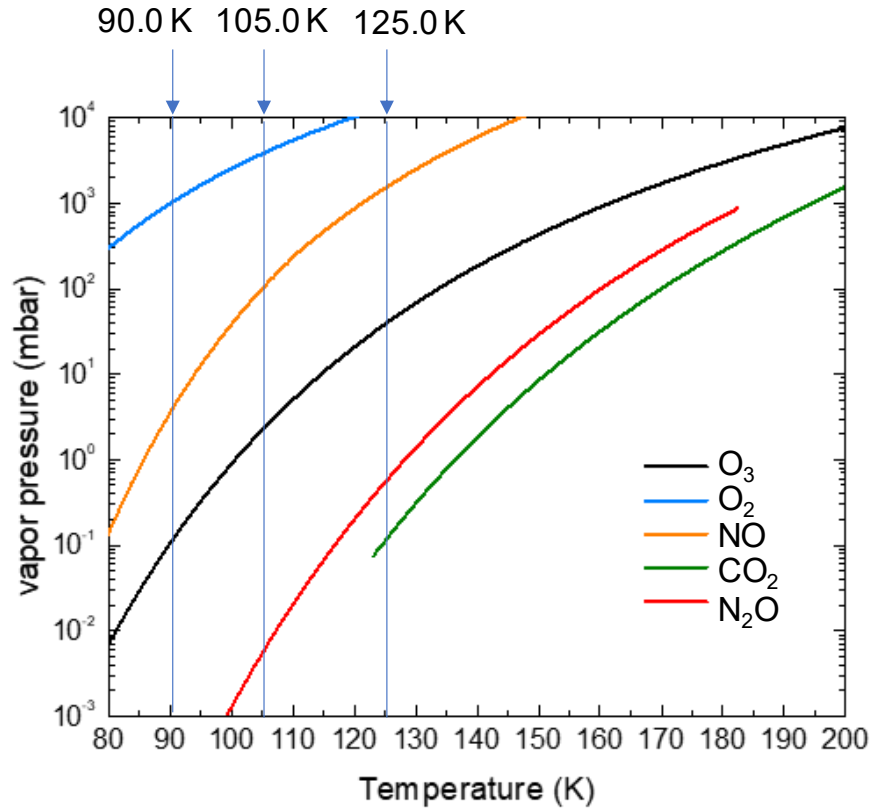

Figure 4.15. The vapor pressures of ozone, oxygen and other impurities that might co-exist in the vessel of pure ozone generator. The operation temperatures of the pure ozone generator are shown on the top of the graph for the comparison of vapor pressures of different gas species[17].

The safety concerns for a pure ozone generator can be solved by using a fully enclosed body metal frame and a dedicated exhaust system for ozone. Inside the body frame of the pure ozone generator, a negative differential pressure compared to the atmosphere is always kept by continuous venting by the exhaust line. Before the exhaust, an ozone decomposer is set before the exhaust line to prevent ozone from getting into the whole exhaust system[18]. Generating pure ozone from the ozone/oxygen gas mixture from corona discharger by a pure ozone generator from Meidensha can be conducted by the following process,

1. Cool the vessel down to 90.0 K by a cryocooler using helium in the compressor.

2. Generate ozone by corona discharge ozone generator and accumulate liquid ozone/oxygen mixture in the vessel at 90.0 K.

3. Raise the temperature of the vessel to 105.0 K to vaporize residual oxygen in liquid ozone.

4. Cool the vessel down to 90.0 K as a standby status to hold liquid ozone.

5. Raise the temperature of the vessel to a temperature that achieves the supplying pressure and start supplying ozone to the MBE system. The pressure of the vessel can be set to from 2000 Pa to 5000 Pa.

6. After the growth, stop supplying ozone and pump ozone out of the gas line.

7. Discharge the ozone from the vessel by raising the temperature to 120 K, pump the vessel through the dry pump and wait for 10 minutes. Then bring the vessel back to room temperature to standby status.

Modifications can be made to the above steps to get desirable outcome properties of gaseous ozone. In step 3, the temperature of vessel can be set to a higher temperature than

105.0 K such as 110.0 K to 115.0 K to increase the purity of ozone gas. However, higher temperature for purification consumes more accumulated liquid ozone, which results in less available liquid ozone for supplying it to the MBE system. For safety reasons, the pressure and the temperature of the vessel in step 5 have a limitation, respectively. Since gaseous ozone explodes at certain pressure, and the pressure in the vessel depends on the temperature, the highest temperature of the vessel can reach is set to 130.0 K. In addition, the limitation of pressure in the vessel is set to 9000 Pa for safety to prevent explosion of ozone inside the vessel. Since the pressure cannot be directly controlled by changing parameters in the pure ozone generator, the limitation for vessel pressure is conducted by an emergency purge by Ar gas when the pressure reaches 9000 Pa to prevent ozone pressure in the vessel from getting unexpectedly high. The purge gas was selected to Ar instead of nitrogen to realize a nitrogen-free environment inside the pure ozone generator. During the ozone supply, if the flow rate in the gas manifold is too low, the pressure in the vessel might keep increasing due to the decomposition of ozone into oxygen and oxygen has higher vapor pressure than ozone, which will be illustrated later in this chapter. Therefore, the flow rate during the supply stage should be high enough to maintain a stable pressure in the vessel and provide high-concentration ozone into the MBE system. The ozone concentration supplied from the pure ozone generator depends on the pressure in the vessel. While a higher vessel pressure can enhance the flow rate of the gaseous ozone, the ozone concentration decreases as the pressure increases due to higher decomposition rate at high vessel pressure. Therefore, a critical point for ozone concentration with optimized vessel pressure can be discovered and flow rates to achieve the highest ozone concentration. The ozone concentration is measured by a binary gas analyzer, which will be mentioned later in this chapter.
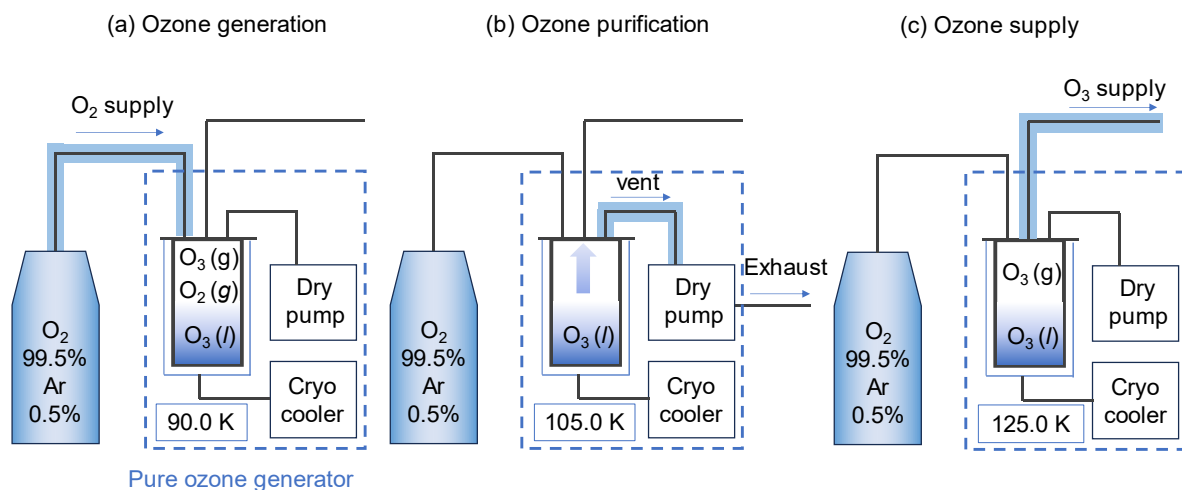
Figure 4.16. Schematics of the process for generating gaseous pure ozone in three steps (a) ozone generation at 90.0 K, (b) ozone purification at 105.0 K, and (c) ozone supply at 125.0 K (a typical operation temperature).

The schematic from generating ozone to ozone supply are shown in Fig. 4.16. In the stage of (a) ozone generation, the O_2 (99.5%) and Ar (0.5%) mixture was supplied to the ozone generator to produce ozone by corona discharge. Here, the resulting liquid that distilled from the ozone generator is a mixture of mainly oxygen, ozone and other gases since the efficiency of ozone generation by corona discharge is about 5% to 8%[12]. In this case, the volume concentration of ozone in the ozone/oxygen gas mixture is approximately 7.2 vol%. As a result, the step for ozone purification is necessary for producing high-purity ozone gas. In the stage of (b) ozone purification, the majority of oxygen is vaporized into gas phase and can be pumped out by the dry pump. Impurities that have lower vapor pressure than ozone such as CO_2, NO_2, and H_2O co-exist in the liquid ozone as separated phase from the test report. In particular, the NO_2 concentration in gaseous ozone is less than 0.01 ppm, which indicates the ozone gas provided by the pure ozone generator is NO_x free.

Lastly, in the stage of (c) ozone supply, the temperature of the vessel is raised to a temperature of around 125.0 K. The operation temperature is determined by the desired pressure in the vessel. While a higher pressure in the vessel gives a higher flow rate to the MBE system, the ozone concentration decreases due to a higher ozone decomposition rate at a higher vessel pressure. The pressure in the vessel needs to be always monitored since ozone gas is explosive above certain pressure.

The delivery of pure ozone gas to the β-Ga_2O_3 sample on the MBE sample stage is conducted by a custom designed gas injector mounted to the MBE system. The connection between the pure ozone generator and the MBE system consists of SUS316L stainless steel gas pipes and Swagelok VCR fittings. The SUS316L stainless steel gas pipes should be electrochemically polished to reduce the decomposition of ozone on the walls of the gas pipes. Figure 4.17 shows the schematic and the parameters of the gas injector when it is in operation mode, which shows the ozone gas supplied from the pure ozone generator is delivered from to the β-Ga_2O_3 substrates. The distance between the nozzle of the gas injector and the sample stage is less than 30 mm. This gas injector is designed to be retractable so that the gas injector can be protected by the shield from the elemental beams from other effusion cells. Additionally, the gas injector is equipped with water cooling to reduce the decomposition of ozone while flowing it in the gas injector. The temperature dependence of the half life time of zone changes significantly in the range of room temperature to a lower temperature such as a temperature near zero °C[19]. The gas valve can be closed when the gas injector is not in use to help the MBE system reach lower background pressure for better growth preparations and prevent undesirable gas leak to the MBE system. The position of the nozzle can be varied for different growth conditions and using of dopants.
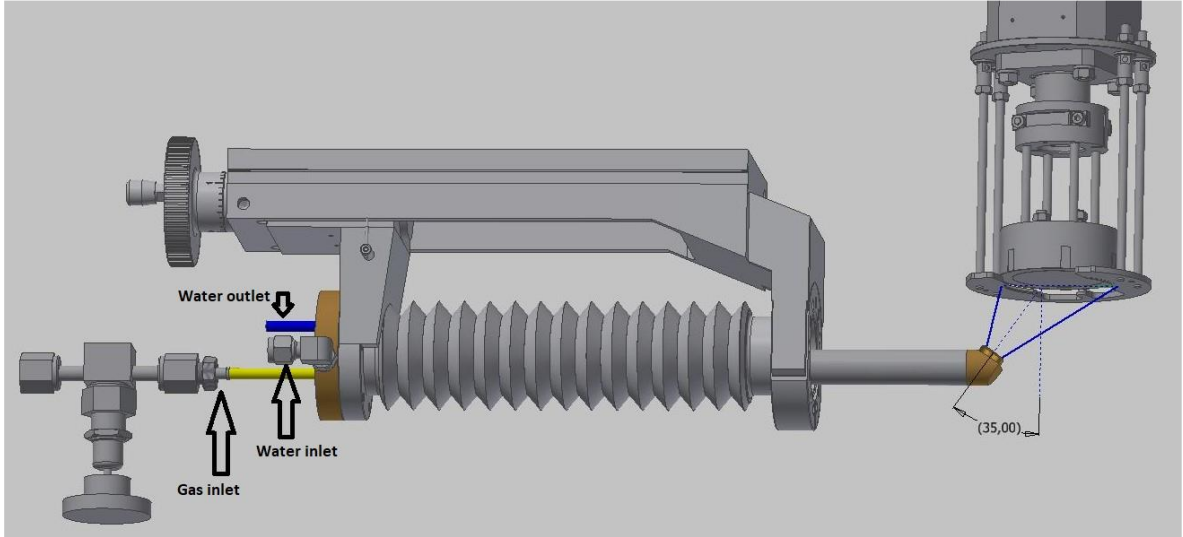
Figure 4.17. The schematic of the gas injector for the delivery of gaseous ozone to the sample stage in the MBE system.

The schematic of the connection of the pure ozone generator to the MBE system (simplified) is shown in Fig. 4.18. The ozone outlet is connected to the gas injector that is mounted on the MBE system. The pressure in the MBE chamber is positively corelated to the pressure in the vessel of the pure ozone generator. Before introducing ozone gas into the MBE chamber, the gas valve between the pure ozone generator and the MBE system should be open for a while to let the gas manifold be pumped to obtain a clean background for ozone delivery. By monitoring the pressure gauge in the MBE chamber, the complete venting of the gas manifold is reached when the pressure in the chamber stabilizes at the range of 1.0×10^{-7} mBar. The growth of β-Ga_2O_3 epitaxial film is conducted by supplying ozone gas and Ga flux to the sample at the same time as illustrated in Fig. 4.18. The nozzle of the gas injector should not be in the shadow of the Ga beam to prevent the deposition of Ga metal on the gas injector.
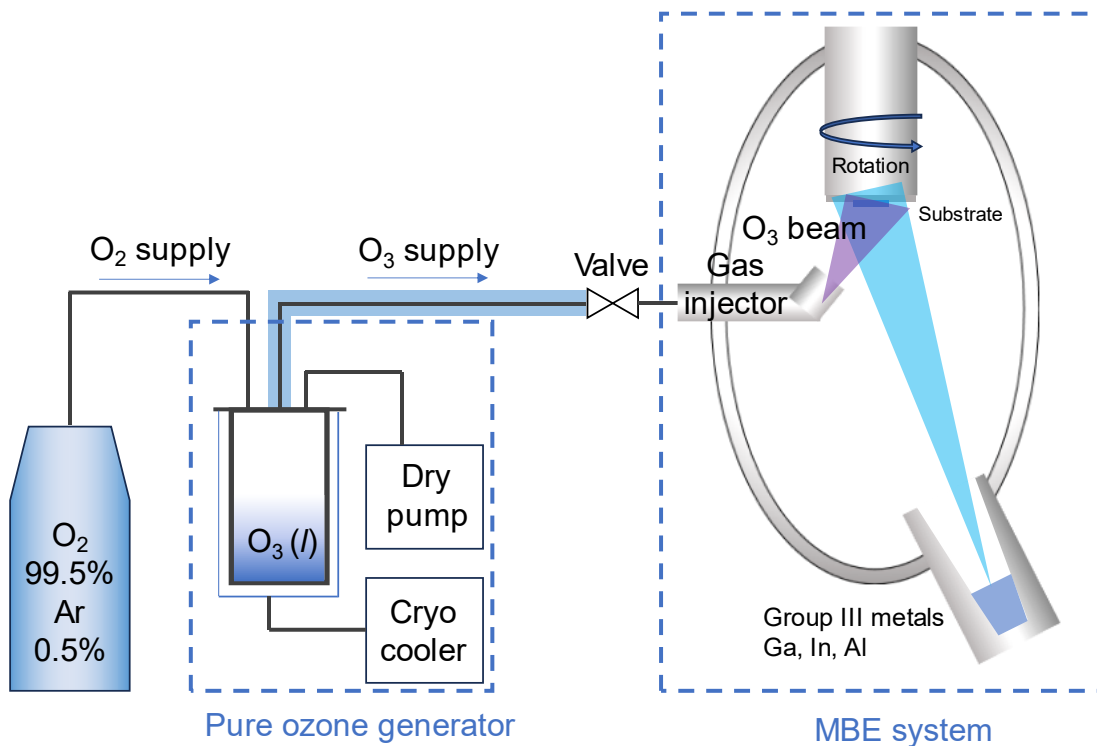
Figure 4.18. The schematic of the connection of pure ozone generator to the MBE system through a gas injector.

The ozone concentration in the ozone supply gas line measured by a Stanford Research Systems process gas analyzer (BGA244HP) in the gas manifold was less than 10.0% in this set up of pure ozone generator and MBE connections. In addition, the ozone concentration in the gas manifold remains the same level for more than 15 minutes after the ozone supply stopped due to the low flow rate of ozone from the pure ozone generator to the MBE system. Figure 4.19 shows the pressure in the vessel of pure ozone generator during ozone charge and ozone supply to the MBE system. The pressure during the ozone charge stage is kept at ~1500 Pa and is pumped down to ~ 0 Pa during the ozone purification stage. After starting the ozone supply by opening all the valves to the MBE system, the pressure in the vessel kept increasing during the ozone supply operation.
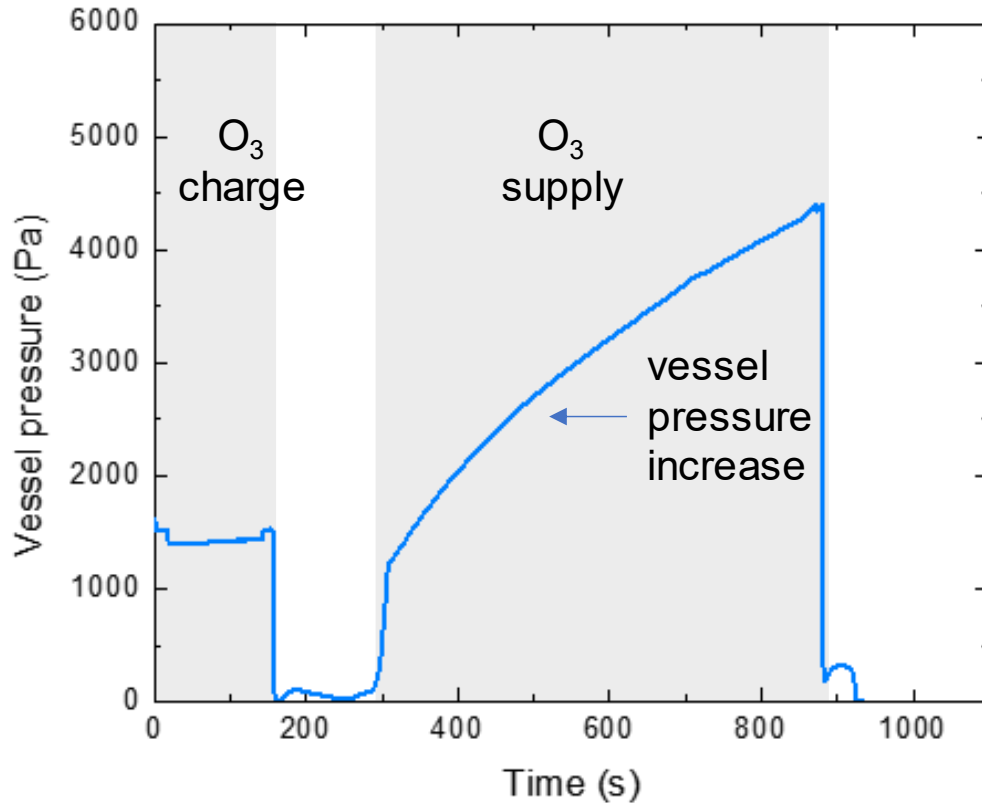
Figure 4.19. Pressure in the vessel of pure ozone generator during the operation of ozone charge and ozone supply. The pressure kept increasing during the ozone supply stage.

The increasing pressure in the vessel of pure ozone generator is attributed to ozone decomposition during the supply operation. As mentioned above, the decomposition rate of ozone depends on the flow rate of the gas in the gas pipes. Despite the pressure difference between the vessel (~ 3000 Pa) and the MBE system (1.0×10^{-9} Torr = 1.3×10^{-7} Pa), the low flow rate of ozone results in high decomposition rate before gaseous ozone reaches the sample stage. Moreover, a constantly increasing pressure in the vessel is not desirable for MBE growth since the changing oxygen supply during the epitaxial growth of β-Ga_2O_3 film, which results in shift of the growth condition in Ga-rich regime or in the oxygen-rich regime, significantly affect its crystal quality, transport properties and surface morphology.

To increase the flow rate of ozone in the gas pipe to achieve higher ozone concentration and stable operation of the pure ozone generator, an ozone loop line is built into the gas manifold and the pure ozone generator. Figure 4.20 illustrates the schematic of a pure ozone generator equipped with the ozone loop line and its connection to the MBE system. Compared to the previous design, the gas pipe that is connected to the gas valve on the gas injector is separated into two directions. One direction flows ozone into the MBE system through the gas injector, while the other flows ozone back to the dry pump with a binary gas analyzer to monitor the ozone concentration at the gas injector and a manual valve to control the flow rate inside the ozone loop line. Before starting the ozone supply, the valve to the ozone injector is closed since the gas flow in the loop line needs time to stabilize. The operation of the ozone supply in the loop line is controlled by a pneumatic gas valve that is integrated with the system software. As the supply of ozone begins, the inner wall of the gas pipeline is continuously passivated by ozone until all the surface area is filled. The pre-conditioning of ozone is not necessary once it is done. The flow rate of ozone in the gas manifold is considerably enhanced by the driving force from the dry pump. The ozone pumped by the dry pump is further guided into an ozone decomposer and vented to the exhaust line. This design of loop line, however, increases ozone consumption due to the pumping from the dry pump that consumes approximately 90% of the generated gaseous ozone. On the other hand, the residual ozone in the loop line can be quickly pumped out by the dry pump after finishing the ozone supply to increase productivity.
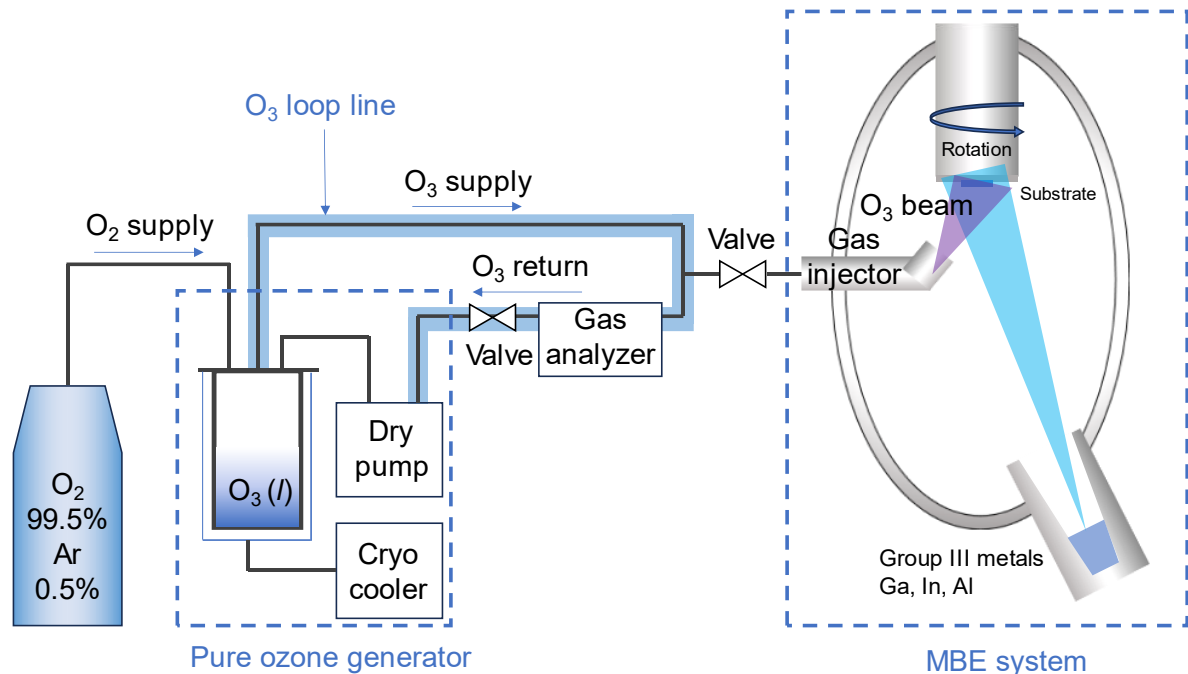
Figure 4.20. Schematics of the pure ozone generator and an MBE system. The loop line is shown by a thick blue line indicating the existence of ozone inside the gas manifold.

To evaluate the effect of the ozone loop line, the relationship between the pressure in the vessel and the flow rate in the gas manifold is shown in Figure 4.21. The manual gas valve that is mounted after the binary gas analyzer has an opening from 0% to 100%. By changing the opening of the manual gas valve, the flow rate in the gas manifold can be varied continuously. Additionally, the flow rate also depends on the pressure in the vessel. At the manual gas valve opening of 25%, 50%, and 100%, the vessel pressures dependence on the flow rates exhibited different trends. Moreover, the highest ozone concentration achieved in the gas manifold is as high as ~ 80% when the opening of gas valve is 100%, which was measured by the binary gas analyzer. When the opening of gas valve is 50%, the highest ozone concentration dropped to ~70%. This is still a considerably high value for the growth of β-Ga_2O_3 epitaxial films.
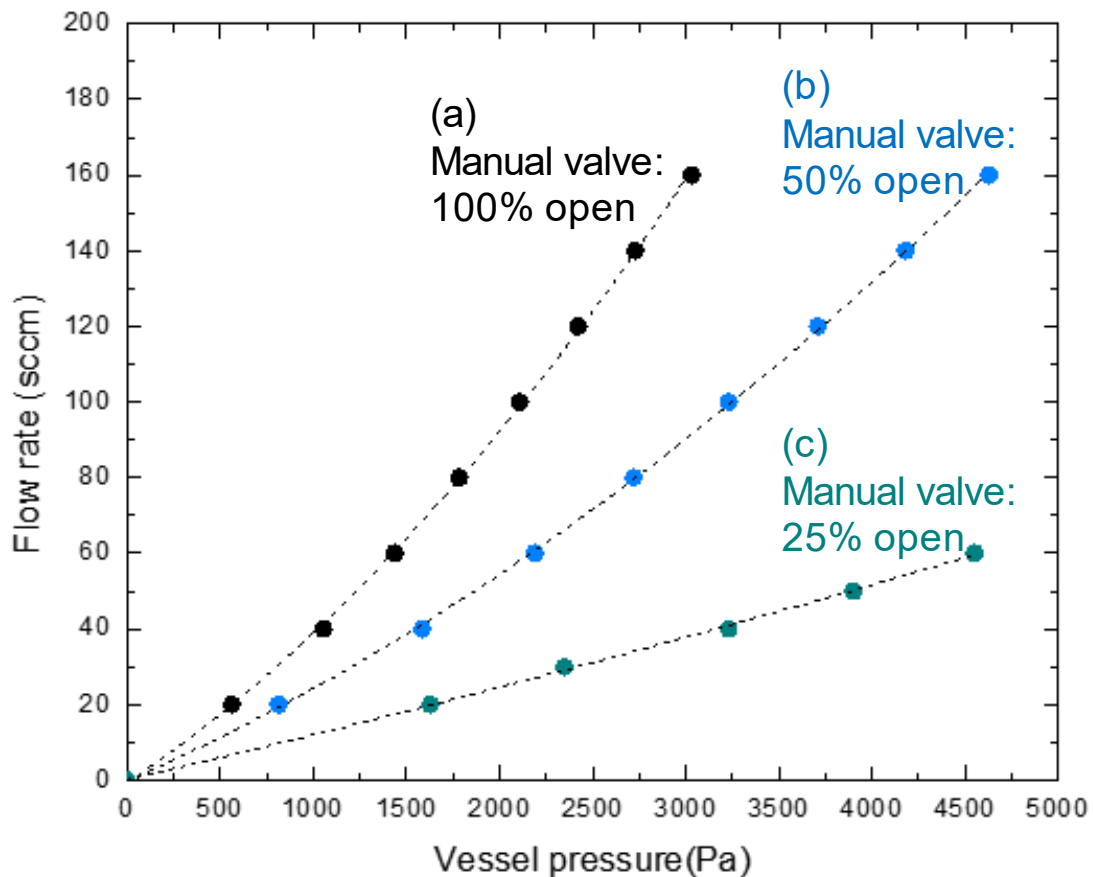
116

Figure 4.21. The relationship between the pressure in the vessel and the flow rate in the gas manifold. The binary gas analyzer shows a higher ozone concentration when the flow rate is higher. The opening is 25%, 50%, 100% at (a), (b) and (c).

From the result, the flow rate can be determined by the pressure in the vessel and the opening of the manual gas valve. The relationship between the flow rate (y) and the pressure in the vessel (x) is derived from the following second order polynomial curve fitting,

$$y = ax^2 + bx + c \text{ (eqn.4.4)}$$

The resulting coefficients of the fitting the three curves at different manual gas valve openings are shown in the following table,

Table 4.1. The coefficients for the second polynomial fitting at different valve openings

Opening	a (x^2)	b (x)	c
25%	6.0×10^{-7}	0.0095	3.1715
50%	3.0×10^{-6}	0.0216	-0.1529
100%	7.0×10^{-6}	0.0329	-0.6809

By acquiring the fitting curves for the ozone flow rate at these three manual gas valve openings, the flow rate of ozone can be estimated from the polynomial equations. For additional fitting curves of flow rates manual gas valve openings, the same experiment can be repeated at other valve openings. This approach is important for the operation of the pure ozone generator since a flow rate meter is not equipped in the gas manifold.

As a result, the ozone loop line significantly increases the ozone concentration in the gas manifold because of the enhanced flow rate. With an ozone concentration of approximately 80%, epitaxial growth by supplying ozone to the MBE system can improve the purity and growth rate of β-Ga$_2$O$_3$ epitaxial films. The issue that the ozone decomposes before it reaches the MBE system was also resolved by increasing the flow rate in the gas manifold by the driving force from the dry pump. With the high ozone concentration supplied to the MBE chamber, the growth of β-Ga$_2$O$_3$ epitaxial films can be improved from the aspects of film purity and growth rate. While the current MBE growth of β-Ga$_2$O$_3$ epitaxial films is limited by the amount of oxygen supply due to the Ga etching related suboxide desorption from the film, the pure ozone generator provides high volume of oxygen supply with high purity to enable the growth of β-Ga$_2$O$_3$ epitaxial films with extremely high purity at a fast growth rate. This will pave the way for the application of β-Ga$_2$O$_3$ to high-performance power electronics with low manufacturing cost.

References

1. G. Seryogin, F. Alema, N. Valente, H. Fu, E. Steinbrunner, A.T. Neal, S. Mou, A. Fine, and A. Osinsky, "MOCVD growth of high purity Ga2O3 epitaxial films using trimethylgallium precursor," Appl. Phys. Lett. **117**(26), 262101 (2020).

2. F. Alema, Y. Zhang, A. Osinsky, N. Valente, A. Mauze, T. Itoh, and J.S. Speck, "Low temperature electron mobility exceeding 10^4 cm^2/V s in MOCVD grown β-Ga2O3," APL Materials **7**(12), 121110 (2019).

3. Y. Zhang, F. Alema, A. Mauze, O.S. Koksaldi, R. Miller, A. Osinsky, and J.S. Speck, "MOCVD grown epitaxial β-Ga2O3 thin film with an electron mobility of 176 cm2/V s at room temperature," APL Mater. **7**(2), 022506 (2019).

4. T. Kamimura, Y. Nakata, M.H. Wong, and M. Higashiwaki, "Normally-Off Ga2O3 MOSFETs With Unintentionally Nitrogen-Doped Channel Layer Grown by Plasma-Assisted Molecular Beam Epitaxy," IEEE Electron Device Lett. **40**(7), 1064–1067 (2019).

5. J.L. Lyons, "A survey of acceptor dopants for β-Ga2O3," Semicond. Sci. Technol. **33**(5), 05LT02 (2018).

6. M.H. Wong, H. Murakami, Y. Kumagai, and M. Higashiwaki, "Enhancement-Mode B-Ga2O3 Current Aperture Vertical MOSFETs with N-Ion-Implanted Blocker," IEEE Electron Device Letters **41**(2), 296–299 (2020).

7. K. Sasaki, A. Kuramata, T. Masui, E.G. Víllora, K. Shimamura, and S. Yamakoshi, "Device-quality β-Ga 2o 3epitaxial films fabricated by ozone molecular beam epitaxy," Appl. Phys. Express **5**(3), 035502 (2012).

8. J. Falson, Y. Kozuka, M. Uchida, J.H. Smet, T.H. Arima, A. Tsukazaki, and M. Kawasaki, "MgZnO/ZnO heterostructures with electron mobility exceeding $1 \times 10\ 6$ cm 2 /Vs," Sci. Rep. **6**, 26598 (2016).

9. M.J. Manfra, K.W. Baldwin, A.M. Sergent, K.W. West, R.J. Molnar, and J. Caissie, "Electron mobility exceeding 160000 cm 2/V s in AlGaN/GaN heterostructures grown by molecular-beam epitaxy," Appl. Phys. Lett. **85**(22), 5394 (2004).

10. Environmental Protection Agency, "National Ambient Air Quality Standards for Ozone," Federal Register **80**, 65291–65468 (2015).

11. H. Itoh, M. Taguchi, and S. Suzuki, "Thermal decomposition of ozone at high temperature leading to ozone zero phenomena," J. Phys. D Appl. Phys. **53**(18), 185206 (2020).

12. B. Eliasson, M. Hirth, and U. Kogelschatz, "Ozone synthesis from oxygen in dielectric barrier discharges," J. Phys. D Appl. Phys. **20**(11), 1421 (1987).

13. S. Ichimura, S. Hosokawa, H. Nonaka, and K. Arai, "Evaluation of new ozone generator designed for oxide film formation by molecular beam epitaxy method," J. Vac. Sci. Technol. A **9**(4), 2369–2373 (1991).

14. S. Hosokawa, and S. Ichimura, "Ozone jet generator as an oxidizing reagent source for preparation of superconducting oxide thin film," Rev. Sci. Instrum. **62**(6), 1614–1619 (1991).

15. K. Koike, M. Nifuku, K. Izumi, S. Nakamura, S. Fujiwara, and S. Horiguchi, "Explosion properties of highly concentrated ozone gas," J. Loss Prev. Process Indust. **18**(4), 465–468 (2005).

16. H. Peelaers, J.L. Lyons, J.B. Varley, and C.G. de Walle, "Deep acceptors and their diffusion in Ga2O3," APL MATERIALS **7**(2), (2019).

17. D. Hanson, and K. Mauersberger, "Precision ozone vapor pressure measurements," J. Chem. Phys. **83**(1), 326–328 (1985).

18. T. Batakliev, V. Georgiev, M. Anachkov, S. Rakovsky, and G.E. Zaikov, "Ozone decomposition," Interdiscip. Toxicol. **7**(2), 47–59 (2014).

19. F.X. Mueller, L. Loeb, and W.H. Mapes, "Decomposition rates of ozone in living areas," Environ. Sci. Technol. **7**(4), 342–346 (1973).

V. Summary and Future Work

5.1. Epitaxial growth techniques for β-Ga₂O₃

PAMBE with proper modifications has shown its outstanding potential for the epitaxial growth of β-Ga₂O₃ films on (110), (010) and (001) bulk substrates. β-Ga₂O₃ epitaxial films grown on (110) substrates yielded smooth surface morphologies and superior crystal quality that is comparable to epitaxial films on (010) substrates and bulk substrates. The growth rates on (110) substrates are reasonable, but not as high as those on (010) substrates. This is presumably due to the different etching rate on (110) facets from the (010) planes. Even though the (110) plane is considered to be an energetic stable plane due to its presence during Ga etching and growth of β-Ga₂O₃ epitaxial films, the surface morphology still shows elongated features without step-flow structures. This might be attributed to the minimum offcut angle of the substrates, which was as small as 0.1°. To further improve the surface morphology of β-Ga₂O₃ epitaxial films grown on this crystal orientation, the investigation of optimal offcut angle of the substrate can be performed to achieve stop-flow mode growth.

The flexibility and availability of different types of elemental metal source is one of the major advantages for MBE as an epitaxial growth technique. Moreover, shallow donors such as Si, Ge and Sn enable β-Ga₂O₃-based high-performance electronic devices. Si is a promising candidate for n-type doping of β-Ga₂O₃ epitaxial films. The doping capability, however, was limited to δ-doping due to the rapid oxidation of the elemental Si source. By utilizing a valved effusion cell for Si elemental source, continuous Si doping of β-Ga₂O₃ epitaxial films on (010) and (001) substrates were achieved. The Si concentration was controlled by either changing the temperatures of the effusion cells or changing the opening of the needle valve. In particular, the Si concentration can be instantly and linearly

121

controlled by adjusting the needle valve of the effusion cell. The high ionization efficiency of Si in β-Ga$_2$O$_3$ epitaxial films compared to Sn makes it the most promising dopant, especially in the heavily doping regime.

While PAMBE shows promising features for the growth of β-Ga$_2$O$_3$ epitaxial films, the challenge for separating nitrogen from oxygen can be an obstacle to the growth of β-Ga$_2$O$_3$ epitaxial films. Despite the purity of the oxygen gas source is 5N:99.999%, β-Ga$_2$O$_3$ epitaxial films grown by PAMBE shows an ineligible amount of nitrogen This is due to the activation of residual nitrogen gas in the oxygen source by the plasma unit, which results in nitrogen incorporation during the growth of β-Ga$_2$O$_3$ films. Since nitrogen is a deep acceptor in the β-Ga$_2$O$_3$ materials system, the amount of nitrogen incorporated into β-Ga$_2$O$_3$ epitaxial film can significantly affect the transport properties. Instead of using oxygen gas tank as oxide source, a pure ozone generator provides high purity ozone gas for the growth of β-Ga$_2$O$_3$ epitaxial films. Since the active oxygen in the MBE growth environment will be provided by ozone molecules, plasma unit is not needed for generating atomic oxygen. Therefore, no more active nitrogen species will be generated and incorporated into β-Ga$_2$O$_3$ epitaxial films during the growth of a pure ozone MBE. Pure ozone MBE is a promising growth technique to grow β-Ga$_2$O$_3$ epitaxial films with high purity for multi-kV level vertical power electronics.

In the future. the key to the success of β-Ga$_2$O$_3$ as the channel of the application to power electronics is the crystal quality. The demand for switching electric power over megawatts (MW) that requires devices can endure voltages ~10 kV is growing rapidly due to the emerging market of electric vehicles and charging stations[1]. The current Si-based power electronics is facing its limitation as semiconductor materials with wide bandgap are

required for high-voltage switching[2,3]. While β-Ga$_2$O$_3$ has the benefit from the availability of high-quality single-crystal bulk substrates, the epitaxial growth techniques still have room for the improvement in the aspect of crystal quality, surface smoothness, doping control and growth rate.

The crystal quality of β-Ga$_2$O$_3$ is the primary factor for choosing epitaxial growth techniques. Currently, MOCVD is the growth technique that provides the highest crystal quality of β-Ga$_2$O$_3$ epitaxial films. Excellent low-temperature Hall mobilities were exhibited from β-Ga$_2$O$_3$ films grown by MOCVD since the high purity of epitaxial films leads to low background compensation level[4,5]. The drawback of MOCVD-grown films, however, is the limitation of maximum film thickness due to the formation of defects from the reaction of gas phase sources. The defects formed on the surface of β-Ga$_2$O$_3$ epitaxial films significantly affect the interface quality when metal or dielectrics is deposited on the surface, which results in early breakdown through the defects. So far, the reported MOCVD-grown films for vertical devices have been limited to less than 2 μm[6]. This limitation in film thickness results in low breakdown voltage compared to other thick films grown by other growth techniques. While vertical rectifiers based on MOCVD-grown β-Ga$_2$O$_3$ epitaxial films with a thickness of ~10 μm was demonstrated previously[7], the device performance was not ideal due to the low crystal quality of the drift layer.

HVPE can grow β-Ga$_2$O$_3$ epitaxial films with fast growth rate up to 250 μm/h and thick film thickness[8,9]. However, the epitaxial films grown by HVPE result in rough surface morphologies and many defects and pits that need post-growth CMP process to obtain a smooth surface. This post-growth process, which needs excessive film thickness to be removed during the CMP, is not required in other growth techniques such as MBE,

MOCVD. In addition, Cl incorporation from the source material GaCl has been the obstacle for the development of high-purity β-Ga$_2$O$_3$ epitaxial films since the drift layer of a vertical device requires sufficiently low doping concentration[10].

Similar to MOCVD, a growth method called mist-CVD, which was developed a Japanese group at Kyoto University, enables growing high quality α-Ga$_2$O$_3$ on (0001) sapphire substrates at low cost[11]. This method uses ultrasonic transducer to vibrate the source solution and then use carrier gas to introduce the mist into the reactor. The susceptor is sometime tiled at 45° to make the reaction more efficient. By using this method, a company called Flosfia collaborated with Kyoto university has been preparing for the mass production of Schottky barrier diodes based on α-Ga$_2$O$_3$ films. Ga$_2$O$_3$ epitaxial films grown by this growth technique has been thermodynamically metastable α-phase and κ-phase, mainly due to the substrates for this method have been foreign substrates such as (0001) sapphire and YSZ (yttria stabilized zirconia). Additionally, homoepitaxial growth of β-phase Ga$_2$O$_3$ has also been performed on β-Ga$_2$O$_3$ bulk substrates[12]. However, the crystal quality of β-Ga$_2$O$_3$ epitaxial films grown by this method needs further improvement to meet the requirements for fabrication of high-performance power electronics.

MBE-grown β-Ga$_2$O$_3$ epitaxial films have superior crystal quality and smooth surface morphology. The availability of n-type donors such as Si, Ge and Sn also makes it a promising growth technique. The growth rate, however, is slower than other growth techniques.

Suboxide MBE is a growth technique that can enhance the growth rate of conventional MBE[13]. Instead of using elemental sources such as Ga metal, suboxide MBE uses a mixture of Ga$_2$O$_3$ powder and Ga metal and heats them up to generate Ga$_2$O suboxide molecular

flux. Since the elemental Ga flux does not exist in the MBE growth chamber, the suboxide desorption reaction does not occur during the growth. In addition, the available suboxide molecular flux has a higher vapor pressure than the elemental metal flux, which results in a higher growth rate than the conventional MBE. The growth rate of suboxide MBE can reach ~1.5 μm/h. This fast growth rate is comparable to other growth techniques such as MOCVD[4,14–16]. The doping capability by utilizing SiO_2 source has also been achieved in suboxide MBE. However, the obstacle for his growth technique is the low purity of powder oxide source materials. The elemental metal source materials for conventional MBE have high purity up to 7N (99.99999%) or even 8N (99.999999%) materials that are available. On the other hand, the purities of oxide powder materials are limited to 5N (99.999%). This purity is two orders of magnitude lower than those of the elemental metal materials, which would result in high concentration of purity incorporation during the process of epitaxial growth. So far, the transport properties in the UID β-Ga_2O_3 epitaxial films grown by suboxide MBE have not been investigated. The Si-doped β-Ga_2O_3 epitaxial films grown by suboxide MBE in a growth rate of ~ 1μm/h showed lower carrier mobilities compared to MOCVD-grown epitaxial films at the same Hall carrier concentration level[17]. In the Si-doped films grown by suboxide MBE, significant Fe incorporation into the film was confirmed due to the low purity of the oxide powder source materials.

$$4Ga\ (\ell) + Ga_2O_3\ (s) \rightarrow 3Ga_2O\ (s,g)\ (eqn.\ 5.1)$$
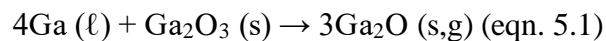
Growing β-Ga_2O_3 epitaxial films by improving the oxygen source could be a promising approach toward high-quality growth with fast growth rate. While MBE can grow β-Ga_2O_3 epitaxial films with superior crystal quality, the oxygen source has been the primary issue of

this growth technique. Firstly, the gas cylinder can only provide the purity of oxygen up to 5N (99.999%). Since it is hard to separate nitrogen from oxygen due to the higher boiling point of oxygen (90 K) than nitrogen (77 K), the residual nitrogen in oxygen source eventually will be incorporated into the β-Ga_2O_3 epitaxial films during the MBE growth process. Nitrogen is a deep acceptor in the β-Ga_2O_3 materials system. While trying to fabricate a lightly doped n-type drift layer for a vertical power device, the incorporated nitrogen in β-Ga_2O_3 epitaxial films would compensates the donor, which significantly affect the donor doping range. Moreover, the supply of active oxygen species is limited in conventional plasma-assisted MBE or ozone MBE. The studies on MBE-grown β-Ga_2O_3 epitaxial films have shown the growth diagram with oxygen-rich regime and Ga-rich regime. The growth rates of β-Ga_2O_3 epitaxial films saturates near the stoichiometric point and decreases due to suboxide desorption. Since the stoichiometric points are usually in the range that the Ga cell temperature is around 1000 ℃, there is still room to generate more Ga flux by using higher cell temperature up to 1300 ℃ or adding additional Ga cells to the MBE system.

To solve these two major problems in a conventional MBE growth of β-Ga_2O_3 epitaxial films, pure ozone with an ozone concentration close to 100% can be used. The process of generating pure ozone by a pure ozone generator was mentioned in Chapter 4. The lightly n-type doped layer requires (1) a n-type carrier concentration that is as low as possible, and (2) the thickness of the drift layer is as thick as possible. Therefore, pure ozone MBE can be the most promising growth technique due to its potential to growth β-Ga_2O_3 epitaxial films with fast growth rate and high purity compared to other epitaxial growth methods such as MOCVD, HVPE and PLD.

126

5.2. Fabrication of β-Ga$_2$O$_3$-based device

The major deposition techniques of dielectric layers for devices applications are atomic layer deposition, plasma-enhanced CVD (PECVD) and sputtering. ALD provides precise thickness control and high-quality dielectric films through the layer-by-layer depositing process. Compared to the other two deposition methods, the low damage to the surface of the semiconductor material due to the absence of plasma or ion damage is one of the biggest advantages of ALD process. Dielectric layers grown by ALD can serve as a protection layer that is deposited on the surface of the semiconductor materials to prevent damage of deposition from other deposition methods[6,18]. On the other hand, the low growth rate and relatively higher process temperature (usually > 200 ℃) restricts its applicable process since most kinds of photoresists cannot be heated up above 150 ℃. PECVD and sputtering are both well-established deposition techniques for dielectric materials. For conventional dielectric materials such as SiO$_2$ and Si$_3$N$_4$, PECVD has relatively fast deposition rate and uniform film quality. Sputtering can be used from materials that are not available for PECVD or ALD such as high-k dielectric materials: BaTiO$_3$ (dielectric constant: 300)[19].

To overcome the ion damage or plasma damage problem caused by the sputtering process or PECVD, and the low deposition rate of ALD, pure ozone MBE could be utilized to grow high-quality oxide dielectrics at a fast growth rate. The deposition of dielectric films on the β-Ga$_2$O$_3$ epitaxial films can be performed seamless in the vacuum chamber without taking the sample out to expose it to the atmosphere, that is, the surface of the semiconductor materials remains clean to form an ultra-pure dielectric/semiconductor interface. This in-situ dielectric deposition process can significantly reduce the interface defects[20], which enhances the device performance. For example, the MBE system for the

127

growth of β-Ga_2O_3 that is usually equipped with Al and Si effusion cells that can directly grow Al_2O_3 or SiO_2 right after the epitaxial growth of β-Ga_2O_3 films. In addition, the sample temperature can be varied to a wider range than ALD and PECVD since MBE has its own equipped sample heater. This leads to higher deposition temperature of the dielectric materials, which might bring high crystal material to achieve superior breakdown performance.

Among the device fabrication process, heavily n-type doped layer is important to form ohmic contact with the contact metal such as Ti. The conductivity for the heavily n-type doped layer depends on the crystal quality and doping capability of the β-Ga_2O_3 epitaxial films. Growth techniques such as MOCVD and PLD has been used to form heavily doped β-Ga_2O_3 epitaxial films with high conductivity[21,22]. To further improve the quality of ohmic contact layers, pure ozone MBE has the potential to grow materials with low background compensation level and high crystal quality.

MBE can also be utilized to deposit metal on the surface of semiconductor materials without taking the sample out of the vacuum chamber[23]. The metals can be either deposited by using an effusion cell or an electron beam evaporator. Metal with low vapor pressure can be deposited by electron beam evaporator instead of the effusion cells to achieve in-situ metal deposition on the surface of semiconductor materials. Additionally, using in-situ Schottky metal deposition could reduce the contamination on the surface, which could result in lower interface states at the metal-semiconductor junctions to enhance the device performance.

Consequently, pure ozone MBE can be a promising candidate for the growth of drift layer, ohmic contact layer and semi-insulating layers in a vertical structure for power

128

electronics applications as shown in figure 5.1. The possibility of high growth rate also improves the productivity of the fabrication of vertical power electronic devices. It should be noted that the process might be able to be conducted in the MBE environment without taking the sample out of the chamber. In addition to the growth of β-Ga$_2$O$_3$ layers with different doping conditions, the etching process can also be conducted inside the MBE system via the suboxide desorption mechanism[24,25]. Therefore, the contamination on the regrowth interface can be minimized by using *in-situ* techniques, such as direct deposition of dielectrics on β-Ga$_2$O$_3$ epitaxial layers and the following metal layers on the dielectrics for the fabrication of MOSFETs.
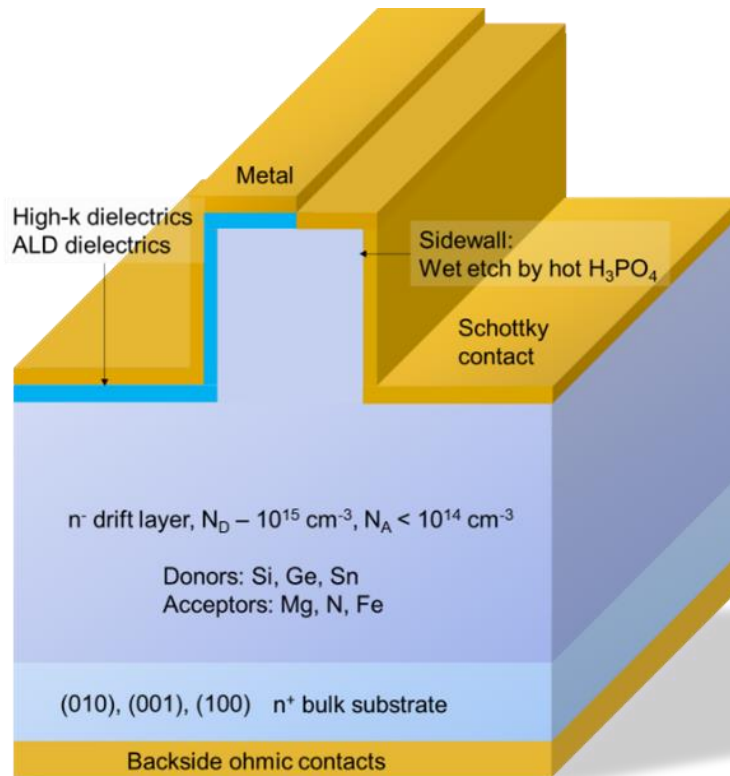
Figure 5.1. A schematic of the ideal structure for the application of vertical power electronic devices.

References

1. Y. Qin, M. Xiao, M. Porter, Y. Ma, J. Spencer, Z. Du, A.G. Jacobs, K. Sasaki, H. Wang, M. Tadjer, and Y. Zhang, "10-kV Ga2O3 Charge-Balance Schottky Rectifier Operational at 200 °C," IEEE Electron Device Lett. **44**(8), 1268–1271 (2023).

2. J.Y. Tsao, S. Chowdhury, M.A. Hollis, D. Jena, N.M. Johnson, K.A. Jones, R.J. Kaplar, S. Rajan, C.G. Van de Walle, E. Bellotti, C.L. Chua, R. Collazo, M.E. Coltrin, J.A. Cooper, K.R. Evans, S. Graham, T.A. Grotjohn, E.R. Heller, M. Higashiwaki, M.S. Islam, P.W. Juodawlkis, M.A. Khan, A.D. Koehler, J.H. Leach, U.K. Mishra, R.J. Nemanich, R.C.N. Pilawa-Podgurski, J.B. Shealy, Z. Sitar, M.J. Tadjer, A.F. Witulski, M. Wraback, and J.A. Simmons, "Ultrawide-bandgap semiconductors: Research opportunities and challenges," Adv. Electron. Mater. **4**(1), 1600501 (2018).

3. M. Higashiwaki, R. Kaplar, J. Pernot, and H. Zhao, "Ultrawide bandgap semiconductors," Appl. Phys. Lett. **118**(20), 200401 (2021).

4. G. Seryogin, F. Alema, N. Valente, H. Fu, E. Steinbrunner, A.T. Neal, S. Mou, A. Fine, and A. Osinsky, "MOCVD growth of high purity Ga2O3 epitaxial films using trimethylgallium precursor," Appl. Phys. Lett. **117**(26), 262101 (2020).

5. F. Alema, Y. Zhang, A. Osinsky, N. Valente, and A. Mauze, "Low temperature electron mobility exceeding 104 cm2/V s in MOCVD grown β-Ga2O3," APL Quote Quad, (2019).

6. E. Farzana, F. Alema, W.Y. Ho, A. Mauze, T. Itoh, A. Osinsky, and J.S. Speck, "Vertical β-Ga2O3 field plate Schottky barrier diode from metal-organic chemical vapor deposition," Appl. Phys. Lett. **118**(16), (2021).

7. J. Yang, S. Ahn, F. Ren, and S.J. Pearton, "High Breakdown Voltage (−201) -Ga2O3 Schottky Rectifiers," IEEE Electron Device Lett., (2017).

8 H. Murakami, K. Nomura, K. Goto, K. Sasaki, K. Kawara, Q.T. Thieu, R. Togashi, Y. Kumagai, M. Higashiwaki, A. Kuramata, S. Yamakoshi, B. Monemar, and A. Koukitu, "Homoepitaxial growth of β-Ga2O3 layers by halide vapor phase epitaxy," Appl. Phys. Express **8**(1), 015503 (2014).

9. Z. Hu, K. Nomoto, W. Li, N. Tanen, K. Sasaki, A. Kuramata, T. Nakamura, D. Jena, and H.G. Xing, "Enhancement-Mode Ga2O3 Vertical Transistors With Breakdown Voltage >1 kV," IEEE Electron Device Lett. **39**(6), 869–872 (2018).

10. R. Lingaparthi, Q.T. Thieu, K. Koshi, D. Wakimoto, K. Sasaki, and A. Kuramata, "Surface states on (001) oriented β-Ga2O3 epilayers, their origin, and their effect on the electrical properties of Schottky barrier diodes," Appl. Phys. Lett. **116**(9), 092101 (2020).

11. D. Shinohara, and S. Fujita, "Heteroepitaxy of corundum-structured α-Ga$_2$O3Thin films on α-Al2O3Substrates by ultrasonic mist chemical vapor deposition," Jpn. J. Appl. Phys. **47**(9), 7311–7313 (2008).

12. H. Nishinaka, T. Nagaoka, Y. Kajita, and M. Yoshimoto, "Rapid homoepitaxial growth of (010) β-Ga2O3 thin films via mist chemical vapor deposition," Mater. Sci. Semicond. Process. **128**, 105732 (2021).

13. P. Vogt, F.V.E. Hensling, K. Azizie, C.S. Chang, D. Turner, J. Park, J.P. McCandless, H. Paik, B.J. Bocklund, G. Hoffman, O. Bierwagen, D. Jena, H.G. Xing, S. Mou, D.A. Muller, S.-L. Shang, Z.-K. Liu, and D.G. Schlom, "Adsorption-controlled growth of Ga2O3 by suboxide molecular-beam epitaxy," APL Mater. **9**(3), (2021).

14. T.-S. Chou, P. Seyidov, S. Bin Anooz, R. Grüneberg, T.T.V. Tran, K. Irmscher, M. Albrecht, Z. Galazka, J. Schwarzkopf, and A. Popp, "Fast homoepitaxial growth of (100) β-Ga2O3 thin films via MOVPE," AIP Adv. **11**(11), 115323 (2021).

15. F. Alema, B. Hertog, A. Osinsky, P. Mukhopadhyay, M. Toporkov, and W.V. Schoenfeld, "Fast growth rate of epitaxial β–Ga2O3 by close coupled showerhead MOCVD," J. Cryst. Growth **475**, 77–82 (2017).

16. F. Alema, Y. Zhang, A. Mauze, T. Itoh, and J.S. Speck, "H2O vapor assisted growth of β-Ga2O3 by MOCVD," AIP, (2020).

17. K. Azizie, F.V.E. Hensling, C.A. Gorsak, Y. Kim, N.A. Pieczulewski, D.M. Dryden, M.K.I. Senevirathna, S. Coye, S.-L. Shang, J. Steele, P. Vogt, N.A. Parker, Y.A. Birkhölzer, J.P. McCandless, D. Jena, H.G. Xing, Z.-K. Liu, M.D. Williams, A.J. Green, K. Chabak, D.A. Muller, A.T. Neal, S. Mou, M.O. Thompson, H.P. Nair, and D.G. Schlom, "Silicon-doped β-Ga2O3 films grown at 1 μm/h by suboxide molecular-beam epitaxy," APL Materials **11**(4), 041102 (2023).

18. N.K. Kalarickal, Z. Xia, H.-L. Huang, W. Moore, Y. Liu, M. Brenner, J. Hwang, and S. Rajan, "beta-(Al0.18Ga0.82)(2)O-3/Ga2O3 Double Heterojunction Transistor With Average Field of 5.5 MV/cm," IEEE Electron Device Lett. **42**(6), 899–902 (2021).

19. Z. Xia, H. Chandrasekar, W. Moore, C. Wang, A.J. Lee, J. McGlone, N.K. Kalarickal, A. Arehart, S. Ringel, F. Yang, and S. Rajan, "Metal/BaTiO3/beta-Ga2O3 dielectric heterojunction diode with 5.7 MV/cm breakdown field," Appl. Phys. Lett. **115**(25), (2019).

20. S. Roy, and A.E. Chmielewski, "In Situ Dielectric Al2O3/β-Ga2O3 Interfaces Grown Using Metal–Organic Chemical Vapor Deposition," Advanced Electronic, (2021).

21. F. Alema, T. Itoh, S. Vogt, J.S. Speck, and A. Osinsky, "Highly conductive epitaxial β-Ga2O3 and β-(Al x Ga1−x)2O3 films by MOCVD," Jpn. J. Appl. Phys. **61**(10), 100903 (2022).

22. K.D. Leedy, K.D. Chabak, V. Vasilyev, D.C. Look, J.J. Boeckl, J.L. Brown, S.E. Tetlak, A.J. Green, N.A. Moser, A. Crespo, D.B. Thomson, R.C. Fitch, J.P. McCandless, and G.H. Jessen, "Highly conductive homoepitaxial Si-doped Ga2O3 films on (010) β-Ga$_2$O$_3$ by pulsed laser deposition," Appl. Phys. Lett. **111**(1), 012103 (2017).

23. K. Huynh, M.E. Liao, A. Mauze, T. Itoh, and X. Yan, "Surface reaction dependence of molecular beam epitaxy grown aluminum on various orientations of β-Ga$_2$O$_3$," APL Quote Quad, (2022).

24. N.K. Kalarickal, A. Fiedler, S. Dhara, H.-L. Huang, A.F.M.A.U. Bhuiyan, M.W. Rahman, T. Kim, Z. Xia, Z.J. Eddine, A. Dheenan, M. Brenner, H. Zhao, J. Hwang, and S. Rajan, "Planar and three-dimensional damage-free etching of beta-Ga2O3 using atomic gallium flux," Appl. Phys. Lett. **119**(12), (2021).

25. S. Dhara, N.K. Kalarickal, A. Dheenan, S.I. Rahman, C. Joishi, and S. Rajan, "β-Ga$_2$O$_3$ trench Schottky diodes by low-damage Ga-atomic beam etching," Appl. Phys. Lett. **123**(2), (2023).

Appendix A. Reciprocal Space Mapping of β-(Al$_x$Ga$_{1-x}$)$_2$O$_3$ films

To understand the coherency between the β-(Al$_x$Ga$_{1-x}$)$_2$O$_3$ films and the β-Ga$_2$O$_3$ bulk substrates, reciprocal space mapping (RSM) measurements can be used on different crystal orientations such as (100), (010) and (001). A proper off-axis crystal plane should be used in this measurement, including (1) detectable crystal plane with a positive value of offset angle and (2) relatively high structure factor to obtain large intensity from the X-ray facility's detector. For the RSM measurement of β-(Al$_x$Ga$_{1-x}$)$_2$O$_3$ films grown on (010) substrates, (420) plane can be used as shown in figure A.1.
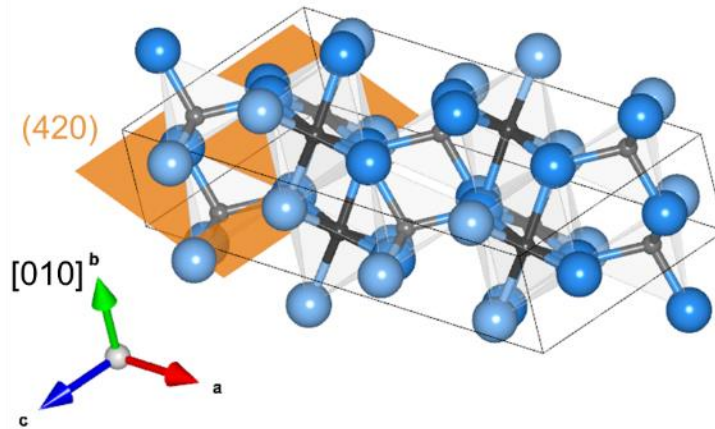
Figure A.1. The unit cell of β-Ga$_2$O$_3$ and the (420) plane for RSM measurements.

An example of β-(Al$_x$Ga$_{1-x}$)$_2$O$_3$ films grown on (010) β-Ga$_2$O$_3$ substrate is shown in figure A.2. On the left is a β-(Al$_x$Ga$_{1-x}$)$_2$O$_3$ film with an Al composition of 26.8%, which was determined from the HRXRD result. On the right is a β-(Al$_x$Ga$_{1-x}$)$_2$O$_3$ film with an Al composition of 30.3%. While the β-(Al$_x$Ga$_{1-x}$)$_2$O$_3$ peak with an Al composition of 26.8% is aligned to the β-Ga$_2$O$_3$ peak in the reciprocal space indicative of coherently strained, the β-

$(Al_xGa_{1-x})_2O_3$ peak with an Al composition of 30.3% is not aligned to the β-Ga_2O_3 peak. These differences of the peak positions of the β-$(Al_xGa_{1-x})_2O_3$ epitaxial films can be used to investigate the coherency of the films to the substrate.
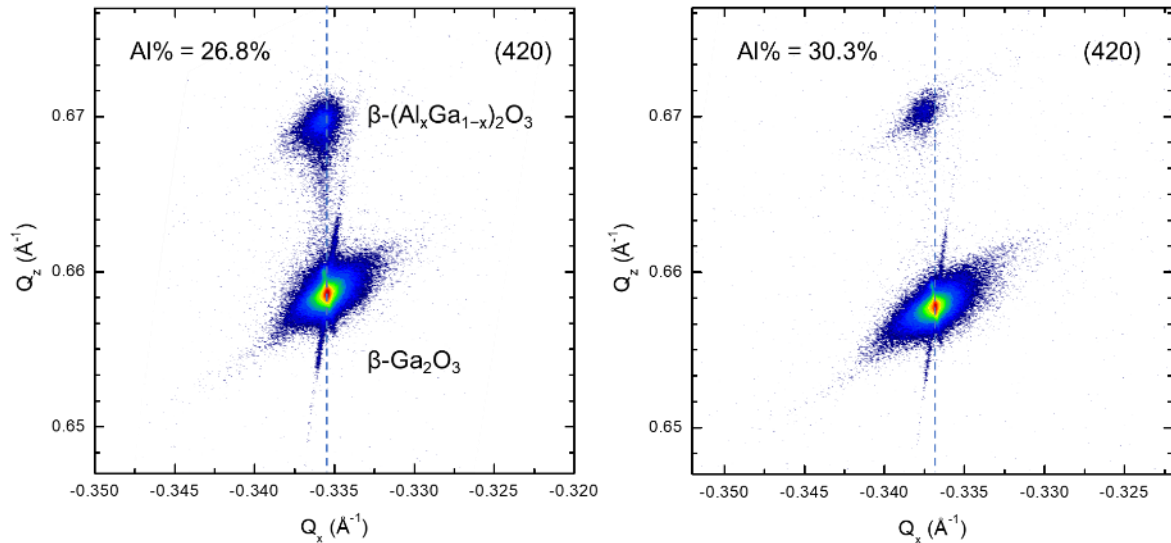

Figure A.2. RSM results of two β-$(Al_xGa_{1-x})_2O_3$ films grown on (010) substrate with Al composition of 26.8% and 30.3%, respectively.

The measurement parameters can be modified to use slits with bigger openings to obtain more signals while losing resolutions to some extent. In particular, the Panalytical Pixel3D XRD facility provides two dimensional detectors for fast measurements of RSM by quickly acquiring two theta/omega results.

In the case of β-$(Al_xGa_{1-x})_2O_3$ films grown on (001) substrates, either the off-axis (404) plane or the (024) plane can be used for the RSM measurement, which is shown in figure A.3. These two planes are detectable orientation that have the positive value of offset angle of two theta and omega with large structure factors.
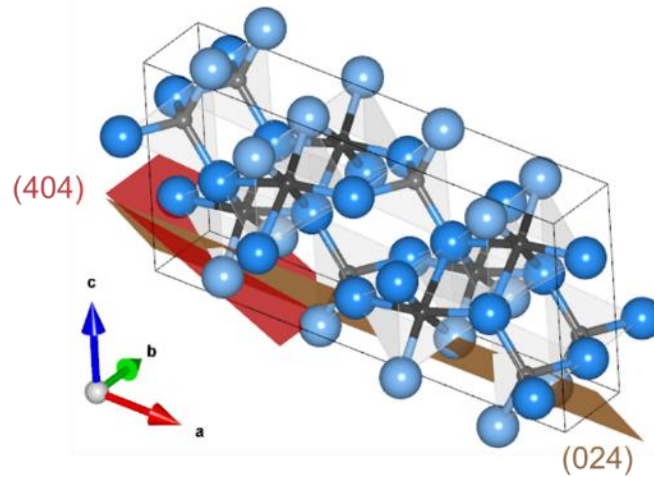
Figure A.3. Off-axis planes (404) and (024) that can be used for RSM measurement for the β-(Al$_x$Ga$_{1-x}$)$_2$O$_3$ films grown on (001) β-Ga$_2$O$_3$ substrates.

The RSM results of β-(Al$_x$Ga$_{1-x}$)$_2$O$_3$ film with an Al composition of 11% are shown in figure A.4. The β-(Al$_x$Ga$_{1-x}$)$_2$O$_3$ film was coherently strained to the β-Ga$_2$O$_3$ substrate.
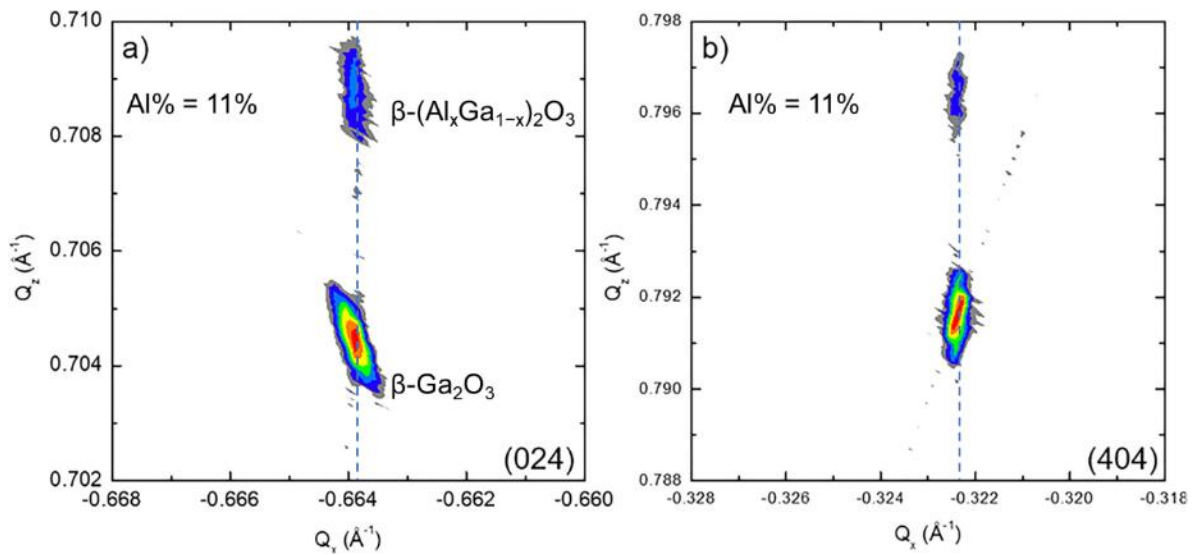

Figure A.4. RSM results on (024) and (404) planes of a β-(Al$_x$Ga$_{1-x}$)$_2$O$_3$ film grown on (001) substrate with an Al composition of 11%.

For RSM measurement of β-(Al_xGa_{1-x})$_2O_3$ films grown (100) β-Ga_2O_3 substrates, the off-axis ($80\bar{1}$) plane can be used. It should be noted that the ($80\bar{1}$) diffraction has a large value of two theta angle. Additionally, the structure factor of this plane is not as high as the cases of β-(Al_xGa_{1-x})$_2O_3$ growth on (010) and (001) substrates. Therefore, the scan should be done with extra step time to accumulate more signals.
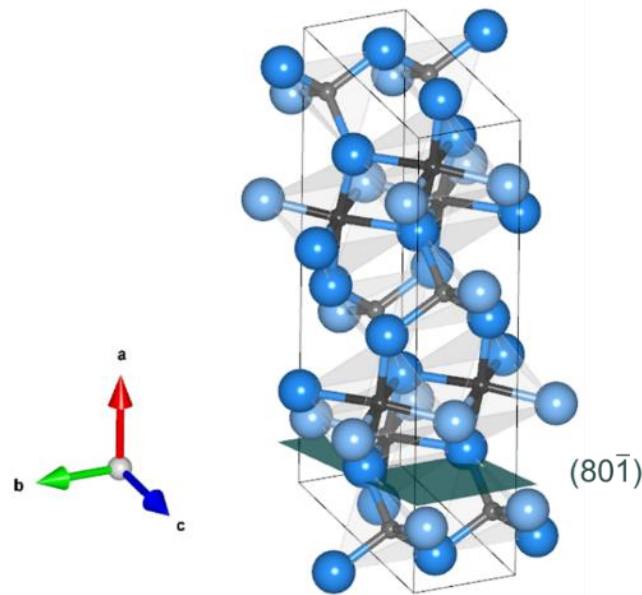

Figure A.5. Off-axis planes ($80\bar{1}$) that can be used for RSM measurement for the β-(Al_xGa_{1-x})$_2O_3$ films grown on (100) β-Ga_2O_3 substrates.

The RSM results of β-(Al_xGa_{1-x})$_2O_3$ film with an Al composition of 34.3% and 39.5% are shown in figure A.6. The β-(Al_xGa_{1-x})$_2O_3$ peaks were aligned to the β-Ga_2O_3 substrate peaks, which indicates that the films were coherently strained.
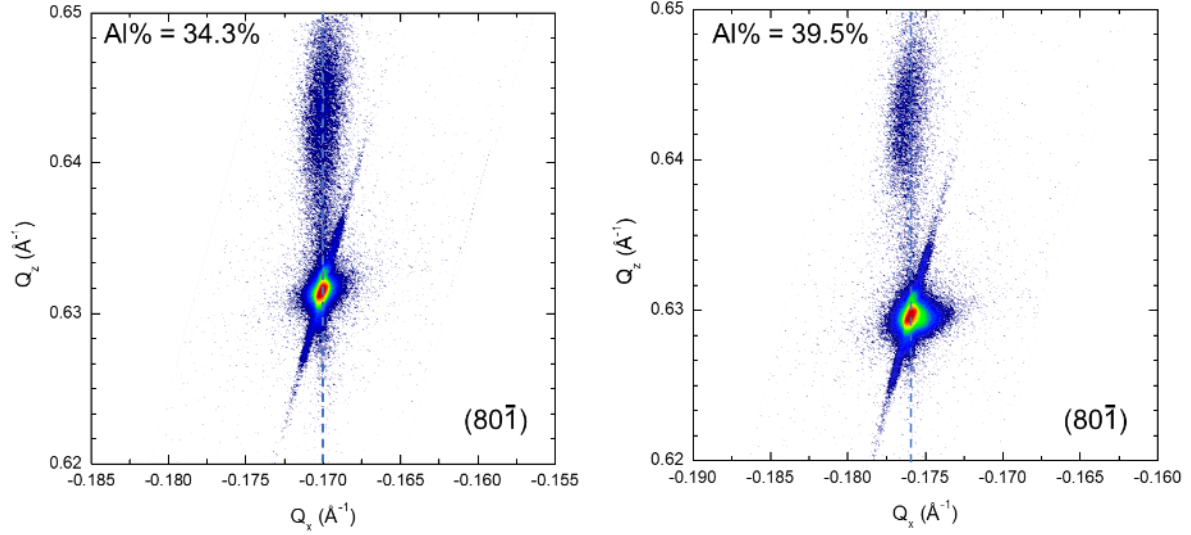
136

Figure A.6. RSM results on $(80\bar{1})$ plane of a β-$(Al_xGa_{1-x})_2O_3$ film grown on (100) substrate with an Al composition of 34.3% and 39.5%, respectively.

The RSM measurements of β-$(Al_xGa_{1-x})_2O_3$ films grown on (100), (010) and (001) β-Ga_2O_3 substrates are shown above. The selection of off-axis planes needs to be a plane with a positive value of offset angle of two theta and omega, and the structure factor should be strong enough for the detector to easily gather signals for accurate measurement.

Furthermore, the RSM measurement can also be applied to superlattice structures that are grown with β-$(Al_xGa_{1-x})_2O_3$ and β-Ga_2O_3 layers. Figure A.7 shows the structure of the β-$(Al_xGa_{1-x})_2O_3/\beta$-$Ga_2O_3$ superlattice sample, its HRXRD results, and the corresponding RSM measurements. The satellite peaks from 0th to 2nd along with the thickness fringes were clearly observed. The RSM results also exhibit the peaks from the superlattice structure. Additionally, by investigating the alignment of the β-$(Al_xGa_{1-x})_2O_3$ satellite peaks and β-Ga_2O_3 substrate peak, the layers are found to be fully strained to the substrate. This

137

measurement requires a wide range of two theta and omega angles to include the satellite
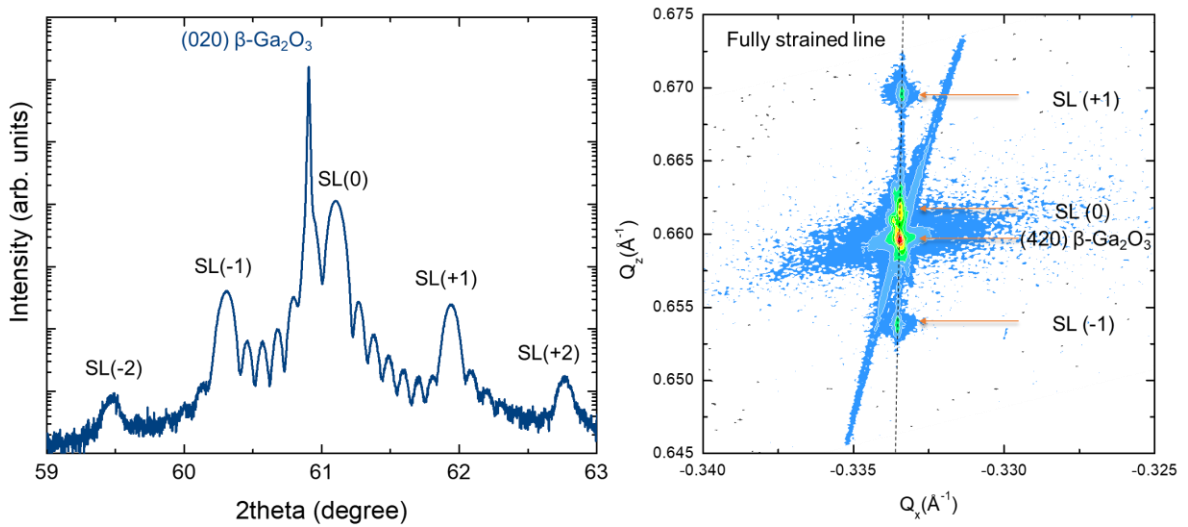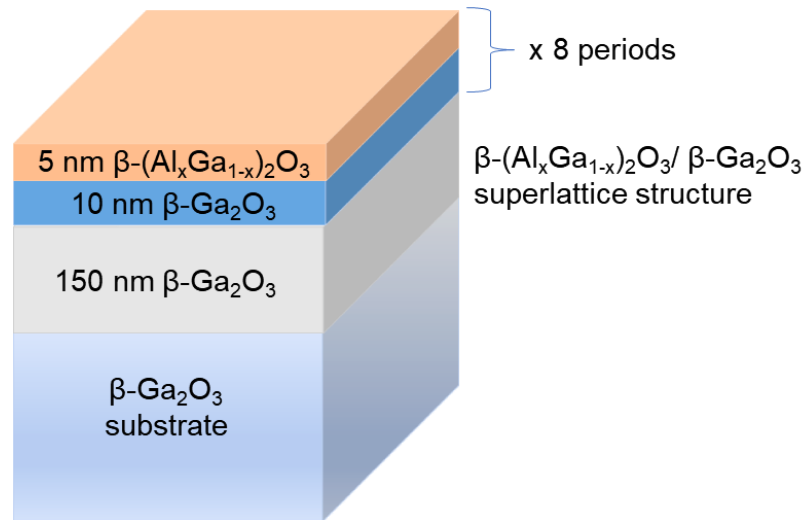
peaks up to the second order.

Figure A.7. The growth structure, HRXRD diffraction patterns and the corresponding

RSM results based on a $\beta\text{-}(Al_xGa_{1-x})_2O_3/\beta\text{-}Ga_2O_3$ structures grown on (010) substrate.

Appendix B. AFM measurement of β-Ga$_2$O$_3$ films and structures

AFM measurement of β-Ga$_2$O$_3$ films is essential for the characterization of the surface morphologies of the MBE-grown films with extreme smooth surfaces. However, the measurement might be challenging due to the low conductivity of as-grown β-Ga$_2$O$_3$ films because of the wide energy bandgap that results in low background carrier concentrations. The resistive sample of β-Ga$_2$O$_3$ means that the surface might accumulate static charge from the environment during handling. In the case of surface charging, the surface profile obtained by AFM measurement can be inaccurate due to the additional repulsive force from the static charge. The bad match between the forward and backward retracement of the surface profile at the edge of the scan area shows up when the surface of the sample is charged up with static charges.
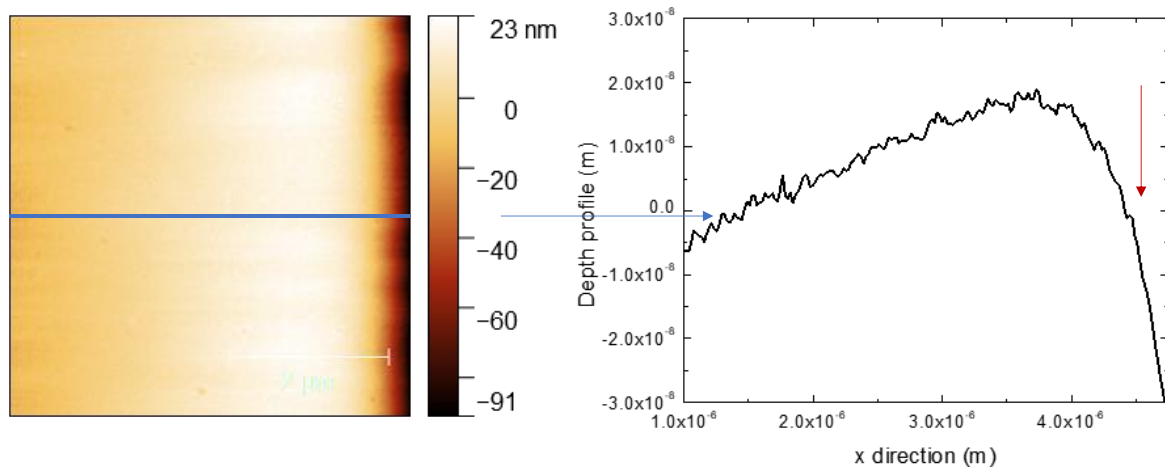

Figure B.1. An AFM image obtained while the sample is charged up. A sharp decline of the cross-section profile can be observed on the edge of the scan area.

To solve the problem of surface charge, the first step is to use a conductive stage such as a 2-inch or 4-inch Si wafer instead of slide glass or other non-conductive materials as the

stage. The conductive stage helps the static charge on the surface of the sample to be released to ground so that the sample is no longer charged up. An anti-static brush can also be used to remove the static charge on the surface of the sample. Additionally, for better resolution of AFM images, the drive amplitude can be increased along with the set point (the value of set point should be approximately twice as the that of the drive amplitude). After tuning the atomic probe, a value of drive amplitude is assigned to the controller for measurement. Since the drive amplitude is obtained when the probe is far away from the sample surface, the value might not be well optimized. This can be fixed by adjusting the value of drive amplitude after the probe is close enough to the sample surface to get more accurate surface profiles.

For the troubleshooting of AFM images with large noises, the replacement of the probe is the first choice to try. Since the AFM probe is made of Si from a Si wafer, the probe itself is fragile and easily damaged. A damaged probe might cause a failed tuning of the tip or an inaccurate response from the surface due to unstable operation. It is important to monitor the phase retracement to make sure the phase is under 90°. When the phase is lower than 90°, the probe is in repulsive mode with the surface of the sample. Compared to attractive mode, which has a phase larger than 90°, repulsive can protect the probe from breaking during the measurement since the probe is not directly touching the surface.
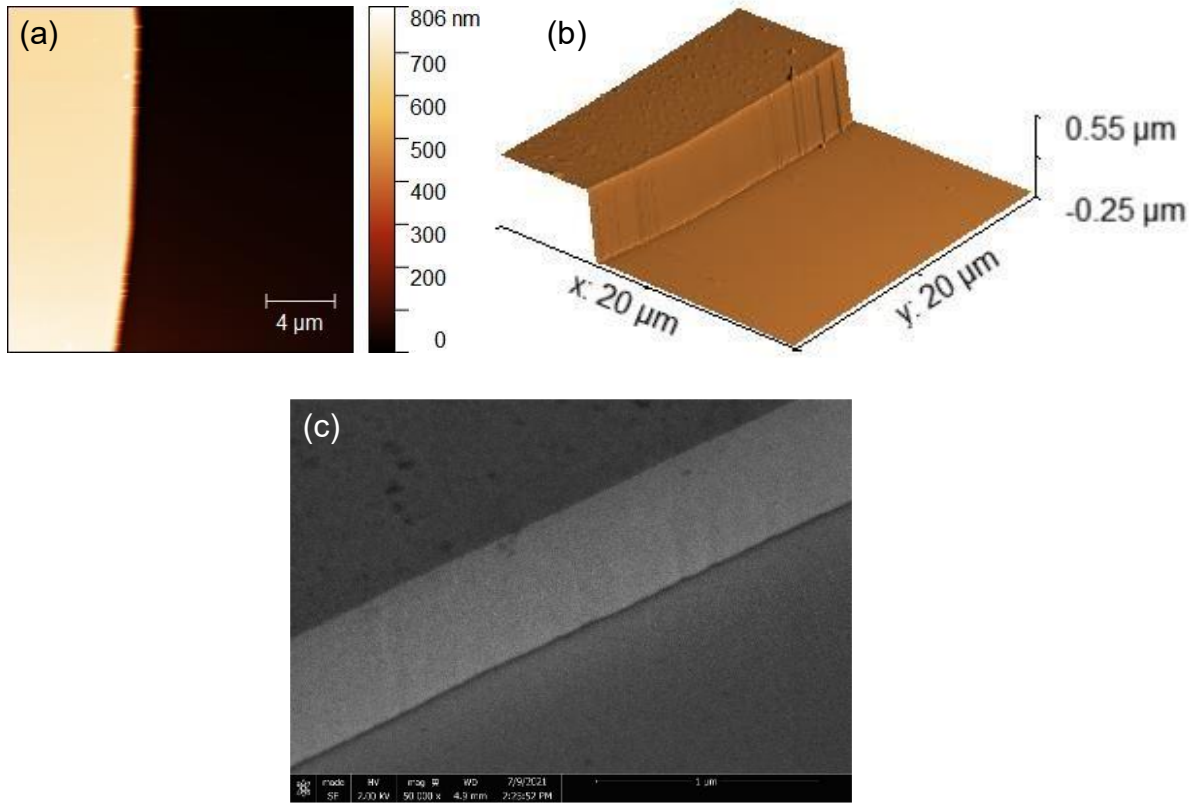
Figure B.2. (a) An AFM image of β-Ga_2O_3 film with a step structure, (b) its 3D mapping of topography and (c) the corresponding SEM image of this structure.

For the measurement of β-Ga_2O_3 film's surface profile with large height differences, the set point and scan rate of AFM measurement can be optimized to obtain high-resolution images. Vertical devices fabricated by dry etching or wet etching can yield step height in the μm range. Since the difference of height in the step structure can be several hundred nm to ~ μm, the set point needs to be a larger value, such as 700 – 800 mV, than that of the scan of a smooth surface. Additionally, the scan rate can be lowered to less than 0.5 Hz to achieve greater accuracy of the details of the slope. The data point is set to 256 per line as default. This value can be increased to improve the resolution on the slope of the step structure. By

using AFM to measure the step structure, the accurate bevel angle between the surface and the slope can be obtained.
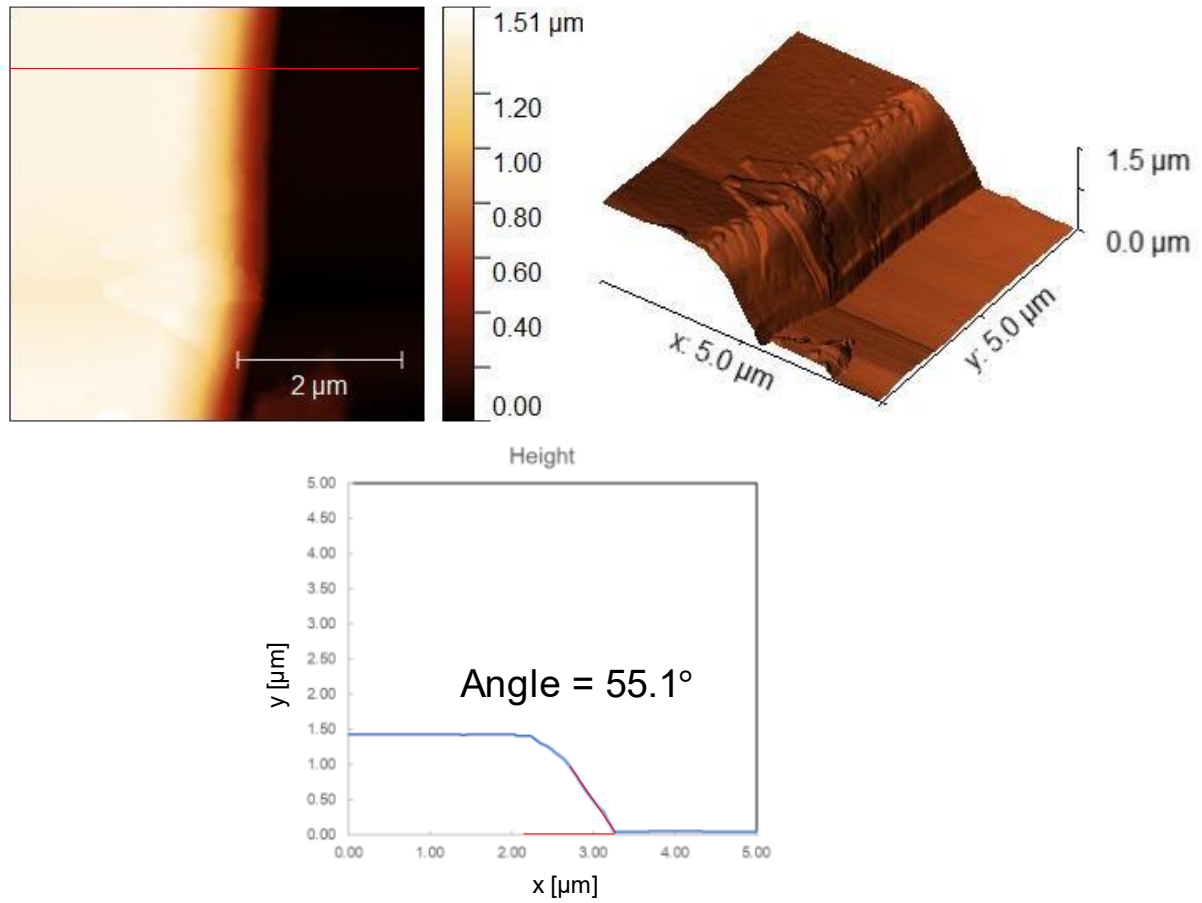

Figure B.3. AFM image of a step structure and its 3D mapping. The angle is measured by the cross-section profile

Appendix C. Operation and safety procedures of pure ozone generator

1. Open Ar (purge gas) and O_2 line to pure ozone generator (POG). Make sure the water line and air compressor are open. Start power by rotating the switch. Wait for warming up. When the ozone sensor is ready, we can use the touch panel. The ozone sensor shows 0000 when the system is ready. The cartridge of the ozone sensor needs to be changed every two years.

Figure C.1. The ozone sensor for monitoring leaking inside POG

2. Push the system state button to reach the command page. Push the command button, then push start POG. Normally, the differential pressure is 3pa. Alarm will buzz to warn the low differential pressure. Can push Buzz off to stop the alarm. Solve the issue and push reset (long push the blue physical button). Push Command and push start POG again.

3. If you want to stop ozone generating, push command again and push stop POG. (The touch panel of pipe view is locked during automatic operation).

4. Ozone chamber starts to cool down toward 90K (need 80 min). When the ozone chamber reaches 90K, reactivate charge enable by long pushing at pipe view. Or, long push the x sign at system state page.

5. Push Setting at system state page. Can change ozone charge volume (>200 cc) at operation setting page. Don't change the ozone charge rate (48 cc/min fixed). The charge volume can be changed after starting charging by changing the charge volume at operation settings page.

6. Ozone Charge: Push Command on the system status page. Push start charging to start accumulating ozone. Make sure Argon is supplied before starting charging. If the pressure in ozone chamber is unstable, check the water flow in the compressor. Can start discharge during the charging process. Can select halt charge during the charge process, but we cannot restart charging.

7. When charging is finished, the status of system is Standby. Unlock the interlock toward feeding. Then press command and start feeding. Can change supplying pressure at operation settings page. Change feeding pressure after reaching 113K. Before reaching 113K, use feeding pressure like 1000 Pa. When reach set point pressure (feed button is blinking), go to system state and push command and feeding start. Open the two valves on the ozone line connected to MBE and change the set point of MFC.

8. Feeding: at around 118 K, 3000 Pa in POG, about 1E-5 Torr in MBE MC. 120K 3600 Pa in POG. 121.5K 4300 Pa in POG, 2.0E-5 Torr in MBE MC, 0.2 sccm in MFC. The highest temperature for feeding is 125 K.

9. To stop feeding (after finishing growth), go to system state page, press command, stop feeding. Now, the MBE chamber is pumping out the whole Ozone line. Can set the MFC to fully open.

10. Starting discharge: on the system state page, press Command, press start discharge.

11. When discharge is over, POG will start to cool the ozone chamber. We can press Command and select Stop POG. Can select start cooling again at the command tab. We can select forced stop after pressing command when the system is heated up to around 200 K. When the Stop POG process is finished, turn off the power by rotating the switch. Turn off Argon and O_2.

The ozone line needs to be pumped out for a while (30 min to 1 hr). We can close the valves to do the transfer or RHEED and open the valves again afterward.